UNIVERSITÉ DU LUXEMBOURG

PhD-FSTM-2022-056
The Faculty of Science, Technology and Medicine

DISSERTATION

Presented on 06/05/2022 in Luxembourg

to obtain the degree of

DOCTEUR DE L'UNIVERSITÉ DU LUXEMBOURG

EN Sciences de l'Ingénieur

by

Mats Bremer
Born on 27 January 1989 in Lindlar (Germany)

OPTICAL MEASUREMENT UNDER SPACE CONDITIONS

Dissertation defence committee

Prof. Dr Slawomir Kedziora, dissertation supervisor
Professor, Université du Luxembourg

Prof. Dr Michael Wahl, Vice Chairman
Professor, Hochschule Trier, Umwelt-Campus Birkenfeld

Prof. Dr Stefan Maas, Chairman
Professor, Université du Luxembourg

Prof. Dr Michael Vielhaber
Professor, Universität des Saarlandes

Prof. Dr Lilia Sidhom,
Professor, National Engineering School of Bizerte, University of Carthage

Table of Contents

1 Introduction

1.1 Motivation

The PhD - project "Optical metrology under space conditions" tries to measure objects which are located in a space simulation chamber with the help of a 3D scanner. The work addresses the question of whether optical measuring instruments can be used for demanding quality assurance in the space industry.

The space industry has become increasingly important since this work began in 2018. Private companies like SpaceX and Blue Origin are in a race with governmental agencies like NASA or ESA. Especially through private companies like SpaceX, it is much easier for research institutes and companies to send satellites into orbit [Spa-21]. With the increased interest in spaceflight, the amount of potential space debris is also increasing [Rau-20], which must be prevented. In addition to the emerging private space companies, the "Cubesat" class of small satellites [NAS-17], established since 1991, plays another important role in the increased interest in space. In addition to these small satellites, a total of 140 satellites weighing less than 30 kg were launched into Low Earth Orbit (LEO) in 2014 [Fun-16].

Cubesat's are a standardized small satellite system that can be used for many applications due to its uniform and compact size [NAS-17, ESA-21]. The smallest variant of these satellites weighs no more than 1.3 kg [NAS-17]. The technical requirements a Cubesat has to fulfill are described e.g. in "Mission Succes Handbook for Cubesat Missions" of NASA. No fixed values are given here, but the quality criteria depend on the defined mission objective of the satellite. An example of European Cubesat requirements can be found in [QB5-15]. For larger satellites, the requirements are specified in, for example, [NAS-21] of NASA.

A test that satellites or their components [NAS-17, Fun-16] undergo is the so-called "Thermal vacuum test" [NAS-19]. For this test, objects are placed in a vacuum chamber. Hot temperatures and cold temperatures alternate inside the chamber [ESA-17], with an "atmosphere" that simulates outer space. After the satellite completes a specified number of alternating cycles, it is removed from the chamber and inspected for damage and deformation. This procedure can take up to 200 hours [NAS-19, p. 23], making it lengthy, costly, and logistically challenging [ESA-17]. These experiments simulate the contrast between the cold of space and the heat of the sun, which can lead to strong deformations or stresses across the components, which may result in damage to the components.

This is where the PhD project "Optical Metrology under Space Conditions" comes in, by determining if a 3D scanner can be used to evaluate the linear thermal expansion of satellite components under space conditions. This allows engineers and developers to gain new insights into the actual deformation of the components, which is particularly interesting for components made of composite materials. With large-scale space

missions such as Starlink [Sta-21], over 40,000 satellites [Tag-21, Cap-21] are sent into low Earth orbit by a single company. It is to be expected that in the point of quality assurance no 100% control of all satellites will take place, as it is currently required in the standards [QB5-15, p 33], because this is too time and cost intensive. With the help of the optical evaluation procedure, a compromise between a 100% control and a sample-like quality assurance could be created. In addition, optical evaluation is a low-cost alternative to the current test standard, which would allow space companies to test components against the extreme conditions in space during development.

3D scanners are used in many areas of our society. In addition to their application in the quality control of technical products such as cars, airplanes or ships, 3D scanners are used in human medicine [Pal-12], dentistry, archaeology and areas of architecture. Through the process of scanning, objects are digitized and the user receives a three-dimensional point cloud of the object. Based on this point cloud, the user can perform a variety of different work processes. The most important ones include evaluation for dimensional accuracy, or a reverse engineering process [Kef-15], where a reconstruction of the surface of the scanned object is performed. Another option is to produce a copy of the object using 3D printers, for this the point cloud of the component must be completely closed.

In this project, the fringe light scanner [Gen-16; Kef-15] Comet L3D 5M from the Zeiss company is used. In the course of this work, the device is used to check the dimensional accuracy of various objects. Subsequently, the components will be thermally loaded and the Comet will be used to record and check the linear thermal expansion. The manufacturer Zeiss does not give any direct information about the accuracy of its devices, since this depends on a multitude of factors [Kef-15]. In the following, requirements for the measurement method to be developed are described.

1.2 Requirements

The following requirements apply to the procedure, which can be divided into two different categories. The first category concerns the environmental conditions in which the components are measured. The second category relates to the measurement procedure.

- **Ambient conditions**
  - Inside the vacuum chamber, there must be a vacuum similar to outer space.
  - It must be possible to heat the components. Temperatures of at least 120°C must be achievable.
  - It must be possible to cool the components. Cooling with liquid nitrogen is desirable, but not mandatory. It should be possible to achieve a component temperature of at least -25°C.

From the requirements for the environmental conditions, it became clear at the beginning of the project that the 3D scanner would not be inside the utilized vacuum chamber. This is due to the combination of the high temperatures and low pressures inside the chamber, which would require a costly and time-consuming modification to make the scanner work, if the space inside the chamber is sufficient. For this reason, the 3D scanner detects the components from the outside through a sight glass. This results in the following requirements for the measurement process.

- **Measurement procedure**
  - It must be possible to evaluate the data quickly
  - The evaluation must be able to detect linear thermal expansions of components
  - The evaluation should have the largest possible measuring volume
  - The evaluation should have high accuracy and repeatability
  - The evaluation must work for as many surfaces as possible.
  - The evaluation must function through an additional glass pane.

A balance must be found for the requirement of the applied measurement volume and the achieved accuracy of the measurement method, since these two factors cannot be maximized at the same time. [Wio-01]. The initial goal is to achieve deviations smaller than 50 µm, as this is an achieved value in the literature [Geo-10, Ber-13]. The effect of the additional glass pane on the 3D scanner is an important core issue and has to be determined in detail within the project. Due to the use of a 3D scanner, the method is subject to the already existing restrictions of the 3D scanning process. This means that the components must not consist of any transparent or partially transparent material. The size of the components is limited by the size of the vacuum chamber.

1.3 Course and structure of this work

The project "Optical metrology under space conditions" started in winter 2018 and was funded by the German state of Rhineland-Palatinate and the European Union.

The work primarily deals with the subject area of optical evaluation by means of a 3D scanner in the application field of quality control for the space industry. Thereby the quality control of the space industry plays only a very small role in the context of the work, and serves much more as a reference point for later characteristic values in different test series. As can be seen from the requirements, a measurement method was developed and tested in the thesis that evaluates objects within a space simulation chamber.

State of the art (chapter 2) shows how 3D scanners were used in similar research work. Special attention is given to the use of an additional medium such as glass or water. Since 3D scanners have a wide range of applications, as already briefly described, non-technical applications such as use in medicine are also listed here.

The third chapter deals with the underlying theory, which is relevant for the later results. Chapter 3 explains the operation of a 3D scanner and basic knowledge of vacuum technology. In Methods and Material (Chapter 4), the general procedure and the experimental setups used are described and explained.

This is followed by the results of the work. Due to the large number of results presented and the general approach, there will be no separation between results and discussion, otherwise the flow of reading and the associated understanding will be too impaired. The presentation of the results follows the principle: from simple issues to complex issues. First, the general accuracy of the scanner is determined and "best practice" parameters are established. Then the effect of the additional glass pane on the scanning process is determined. Then, step by step, the environmental parameters are adapted to space conditions, and linear thermal expansions on different objects are determined. Finally, different satellite components are evaluated. The work is concluded with a conclusion and an outlook on potential improvements.

2 State of the Art

The present work deals with a practical application of optical metrology using 3D scanners. In the course of the work, no custom 3D scanner was developed or special software or an additional algorithm for the data acquisition of the employed device was generated.

In this chapter, scientific work and practice-oriented results from the literature in the field of 3D scanning are presented. The focus is on strip light scanners, such as the Comet L3D 5M. In addition to findings on the general accuracy of 3D scanners, research for scans through an additional medium such as glass is demonstrated.

From the user's perspective, little information can be found in the literature on specifics for determining the accuracy of 3D scanners. VDI Guideline 2634 [VDI-08a-c] and DIN EN ISO 10360-13:2020-07 [DIN-20] provide guidance for various systems on how to determine the accuracy of scanners. The guidelines relevant to this work are [VDI-08b] for systems with areal scanning, [VDI-08c] for systems with areal scanning in multiple single views, and DIN EN ISO 10360-13:2020-07, which combines the two VDI guidelines. The underlying theory and the associated definitions of terms are discussed in Chapter 3. It is important for the following scientific literature that the guideline mentions different test specimens with which the accuracy can be checked. Among others, the guideline lists gauge blocks and test spheres as possible test specimens.

Gauge blocks of this type are investigated in the work of Bernal et al. [Ber-13] using a Comet L3D 5M. In this work, the authors use four gauge blocks of different sizes to investigate the accuracy of the scanner. For each gauge block, five 3D measurements were taken and subsequently evaluated in Inspect+. A matte adhesive tape was applied to the gauge blocks to reduce optical noise due to the polished surfaces of the gauge blocks. The deviations determined between the digital point clouds and the real object are on average around 50 µm. However, the measurement values obtained vary greatly in the individual measurement series, so that standard deviations of up to 0.174 mm are achieved here. The authors attribute this to the number of individual views and to the experience and skill of the user. Georgopoulos et al. [Geo-10] also investigated, among other things, the accuracy of a stripe light scanner using two different gauge blocks processed with matting spray. The scanner is a model manufactured by XYZRGB Inc. This device uses two cameras and a light source for data acquisition. The results for the measurement of gauge blocks are consistent with the results of Bernal et al. [Ber-13] in that the accuracy of the scanner is 50 µm on average. However, the authors also note that some individual measurements are above this value.

The work of Radomir Mendricky [Men-16] also deals with the accuracy of a strip light scanner. Mendricky uses an ATOS device of the company GOM (now Zeiss Optotechnik) with different measuring fields. He investigates the influence of the time of the last calibration of the scanner on the accuracy, as well as the effect of matting spray. For this purpose, he uses a special calibration scale on which three pairs of spheres are mounted. The pairs have different diameters, and there is a fixed distance

between the spheres of each pair. Such a body is also used in VDI Guideline 2634 [VDI-08a-c]. The body was measured tactilely on a coordinate measuring machine. Since the body is very reflective, a matting spray is used in the work for all results of the 3D scanner. For the evaluation, Mendricky followed instructions from the GOM company. For the evaluation, the sphere diameters were measured as well as their distance from each other. First, the device was properly calibrated, and a week later, 10 measurements were made for the sphere diameter and 5 measurements for the sphere distance. Subsequently, the device was calibrated again and immediately after that the measurements were repeated. The results for the influence of the calibration time show that a one-week-old calibration results in a deterioration of the measurement result of up to 30 µm for the distance measurement. For the evaluation of the sphere diameter, the deviation is about 20 µm. These results were generated with the 250-measuring volume of the scanner. Mendricky is investigating the influence of the matting spray to see to what extent multiple layers of the spray affect the results. For the sphere diameters, a second layer of the spray results in the logical result that the measured sphere diameter increases by about 3 µm. For the distance measurement between the spheres, no effect of the second layer can be found. The work of D. Palousek et al. [Pal-15] also investigated the behavior of different matting sprays. The average layer thickness was determined, which is produced when the aerosol based coatings are applied to the component. The comparison showed that the chalk matting spray used, with an average particle size of 9 µm, leaves an average coating thickness of 44 µm on the component. The titanium oxide matting spray used by Palousek et al. left an average coating thickness of about 5 µm.

In 2020, M.G. Guerra et al. [Gue-20] investigated the accuracy of different scanner systems using a step gauge block. Among the considered systems was the fringe light scanner ATOS III of the company GOM (now Zeissoptotechnik). The investigated measuring volume has a scanning area of 60 x 45 x 30 mm³ and is thus significantly smaller than the measuring volume of Mendricky [Men-16]. Different length measurements were evaluated with the help of the step gauge block. The gauge block was previously measured tactilely on a coordinate measuring machine in order to obtain accurate nominal values. The results for the strip light scanner show that the measurement error of the scanner increases slightly with increasing length. The deviation from the nominal value does not exceed 5 µm on average, but the results vary with a standard deviation of ± 10 µm.

In 2004, A. Yamashita et al. [Yam-04] published an algorithm that allowed a 3D scanner to scan into a glass water tank from the outside. In their work, Yamashita et al. use a camera and a laser to determine the 3D point cloud of the object to be measured. Here, the object is located in a glass water tank whose walls are flat and not curved. To calculate the points, Yamashita et al. use a ray tracing method that simplifies the laser line and camera to many individual points, so that the calculation of the three-dimensional point coordinates resembles the intersection of two straight lines. This forms the basis for the algorithm, which is used to measure a rectangular object inside the tank. The results show that the algorithm can be used to calculate the

optical displacements of the individual media, and accurate 3D measurement is possible.

Building on the results of [Yam-04], M. Pallone et al. [Pal-12] investigates the possibility of using a 3D laser scanner to improve the results of microwave tomography for breast examinations. In this work, two laser lines and a camera are used to capture the surfaces of breast-shaped phantoms [Bli-20]. The phantoms are placed in cylindrical containers surrounded by a glycerol solution, which is necessary for microwave tomography. The laser-diodes as well as the camera, are placed on a circular structure around the cylindrical container. The laser-diodes are oriented so that the laser line is perpendicular to the tank. Pallone et al. must adapt the algorithm of [Yam-04] due to the experimental setup. In addition to the algorithm, Pallone et al. test different registration algorithms that compose the individual images from the 3D scanner. Pallone et al. wanted a 3D registration that had an accuracy of 0.5 mm. Using a calibration field, Pallone et al. discovered that Yamashita's ray tracing method had the largest error compared to the other registration algorithms. The average deviation of 1.863 mm of the ray tracing method can be explained by the numerous error sources of the real experimental setup, which cannot be considered in the simplified assumptions of the point calculation. An example is e.g. the wall thickness of the cylinder, which according to the manufacturer, varies by about ± 1 mm. These dynamic variations cannot be compensated for by the static calculation model. For further experiments, Pallone et al. use a different registration method for the 3D data and obtain three-dimensional point clouds, which have a deviation of less than 0.5 mm.

For 3D scans under space conditions, reference can be made to the work of T. Hadjimichael et al. [Had-10]. Hadjimichael's team investigated the behavior of a laser radar under space conditions for the James Webb Space Telescope. For the experimental setup, the authors used a vacuum chamber at the Goddard Space Flight Center. The chamber can image temperatures from -120°C to 110°C, but no direct information is given about the vacuum achieved. However, since the chamber is evacuated with 3 cryopumps, the chamber can reach very low vacuums. The aim of the work of Hadjimichael et al. was to measure a series of test bodies or test points through a glass pane. The test bodies were mounted inside the chamber on an aluminum frame. A ray tracing approach was to be used to calculate the displacements through the different media, in this case, air, glass, and vacuum. Initial experiments showed that the glass leads to displacements of up to 5 mm. Only the displacement in the direction of the optical axis of the laser remained relatively small with 0.07 mm. The ray tracing method was able to reduce this measurement error. The results showed that the deviation at room temperature was about 11 µm. The second set of results, with a temperature of 130 K inside the chamber, showed larger deviations of about 21 µm. The higher deviations are attributed to the vibrations of the three cryopumps.

In 2011, the approach of Hadjimichael et al. [Had-10] was taken up and improved by J. Hayden et al. [Hay-11]. In this work, the ray tracing approach was improved, and instead of using external software, the calculation was performed in Matlab. The experimental setup and requirements remained the same as Hadjimichael [Had-10]. In

their work, Hayden et al. mainly investigated that refractive behavior of the installed glass pane in relation to the material used as well as the additional deformation due to the vacuum present inside the chamber. Direct numerical values for the deviation are not provided in the paper. The authors report that the Matlab code works and a deviation of less than 20 µm is obtained, which is sufficient for measurements with a laser radar. In 2015, a patent was filed based on this calculation [Hay-15], which shows that the Matlab application continues to be used for experiments.

The influence of environmental factors such as the acquisition angle between the object and the scanner, as well as the light exposure, were investigated in the work of F. Li et al. [Li-17] and S. Gerbino et al. [Ger-16]. Gerbino and his team used a design of experiment (DoE for short) to investigate the effect of three different environmental factors on the accuracy of a laser line scanner. The factors studied are the exposure angle, the ambient lighting, and a camera filter. The component to be measured was a part of a car body with numerous free-form surfaces. The laser line scanner is a system that can be controlled by a gripper arm using a measurement coordinate machine. The DoE showed that only the acquisition angle had a statistically significant effect on the results. The work of F. Li et al. [Li-17] investigated the effect of ambient lighting on the scanning results of an ATOS III from GOM. For this purpose, Li et al. investigated exposures with different lumen intensities. The three exposure levels studied were 660 lux, 280 lux, and 0 lux. The test specimen under investigation is a body with different shape elements and free-form surfaces. For each of the three ambient exposure settings, 10 measurements were taken. The results showed that the strip light scanner achieved consistent results on average for all ambient exposures. However, the individual measurements vary greatly, which the authors of the paper also note and state as a disadvantage of optical triangulation. The results obtained by Li et al. [Li-17] are consistent with the results of Gerbino et al. [Ger-16] that the ambient exposure does not exert a significant influence on the performance of a 3D scanner.

The work presented so far addresses the issue of 3D scanner accuracy, the influence of environmental or setting parameters, and scanning through an additional medium. However, these works do not show the wide-ranging and versatile applications of 3D scanners. To this end, some recent scientific work is presented below. One of the main applications of 3D scanners is the process of reverse engineering (RE). The point cloud acquired with the 3D scanner is used as a basis to create non-existing CAD data for still existing, mostly old, objects. The problems and challenges of reverse engineering are addressed in the work of R.H. Helle et al. [Hel-21]. The work makes a comparison between literature results and an own experiment and concludes that RE processes should use scanned data, especially for freeform surfaces. A practical example for reverse engineering based on a 3D-Scan can be seen in the work of te Heesen et al. [Hee-20]. In this work an antique belt buckle was reconstructed with the help of a complete 3D-Scan. From the field of quality control, the work of W. Kwangwoo et al. [Kwa-19] and D. Lazarevic [Laz-19] can be mentioned. Kwangwoo et al. [Kwa-19] investigate the quality of additively manufactured clay components using a 3D scanner. Based on the scanned data sets, deviations and deformities of the printed components

can be determined so that the additive manufacturing process parameters can be adjusted. Lazarevic et al. [Laz-19] compare several 3D scanners using a milled aluminum component. Different scanners from the company GOM and a coordinate measuring machine are used. The results show that although the 3D scanners are less accurate than the measuring machine, the inaccuracies in the distance measurements are in the range of about 50 µm. For measurements of parallelism, flatness, and perpendicularity, the scanners deviate only minimally from the measuring machine.

In summary, it was shown that determining the accuracy of 3D scanners is still a current research topic [Men-16, Gue-20]. Thereby, the achieved accuracy for fringe light 3D scanners for matted objects is 30 - 50 µm. For non-matted or reflective objects, no value was found in the reference literature other than [Bre-19], which is part of this work and establishes a 20 µm accuracy for reflective surfaces. Ray tracing methods [Yam-04, Pal-16, Hay-15] can be used to calculate the optical displacements of the additional media, allowing accurate measurements of up to 20 µm precision [Hay-15]. However, this value was obtained for a laser radar and not for a stripe light 3D scanner. The work presented also shows that the ray tracing method must be adapted to the experimental setup. From the studies for the environmental conditions, it was shown that only the acquisition angle has a significant effect on the accuracy of the 3D scanners [Ger-16]. However, this result by Gerbino et al. was obtained using a laser line scanner. Related to the problem at hand in this dissertation, this raises the following questions that need to be answered before the actual task:

- How accurately can a stripe light scanner scan a reflective object?
- Which environmental parameters or setting options influence the result of the 3D scan the most?
- Will a ray tracing method be necessary to perform three-dimensional measurements behind a glass pane?

The importance of the first question arises from the fact that matting sprays cannot be used inside vacuum chambers. The use of the spray prevents the vacuum from being as low as possible because the particles of the coating are attracted to the vacuum pump. For this reason, matting spray is not used for experiments under space conditions, so the accuracy of the 3D scanner for reflective objects must be determined. The experiments carried out in this work are all based on VDI 2634, so the general accuracy and the influence of the glass pane were determined using a gauge block.

As part of this investigation, the effect of the various setting parameters for the 3D scan is also determined. It is particularly important to validate or refute the results of F. Li et al. [Li-17], since good illumination of the components inside the vacuum chamber cannot be guaranteed.

The third question using an additional ray tracing program to compute the 3D data costs time and, depending on the applied software, money. The aim of the work is to measure the thermal expansions of the components under space conditions as simple

as possible as a "normal" user of a 3D scanner. For this reason, a possible ray tracing approach should be omitted if possible. The results of Pallone et al. [Pal-16] and Hayden et al. [Hay-11] also showed that ray tracing approaches still have strong deviations, so that an application does not immediately provide accurate results.

3 Theory

In this chapter, the underlying theory for the later results is explained. The basic principle of the applied 3D scanner will be explained, as well as the general procedure of a 3D scan. In addition, definitions of terms are established, which will be used repeatedly throughout the thesis. Besides the 3D scan, there is a brief overview of the subject of vacuum - technology. In the course of this work, no new results or findings are made in the field of vacuum technology, so only a small insight is provided in order to understand the later experimental setup.

3.1 3D-Scan

In this chapter, the fundamentals of 3D scanning are presented. As already described, the Comet L3D 5M fringe light or stripe light scanner (Comet for short) from Zeiss was used for this work. The described contents of this subchapter, therefore, refer to fringe light scanners. In order to have an overview of the different technologies, a small overview of the different measurement methods is provided at the beginning. Subsequently, the function of the stripe light scanner will be explained.

3.1.1 Triangulation

The basis for the optical evaluation with the help of the Comet is the triangulation method. The basic principle of this method is shown in Figure 1 and will be explained in the following.

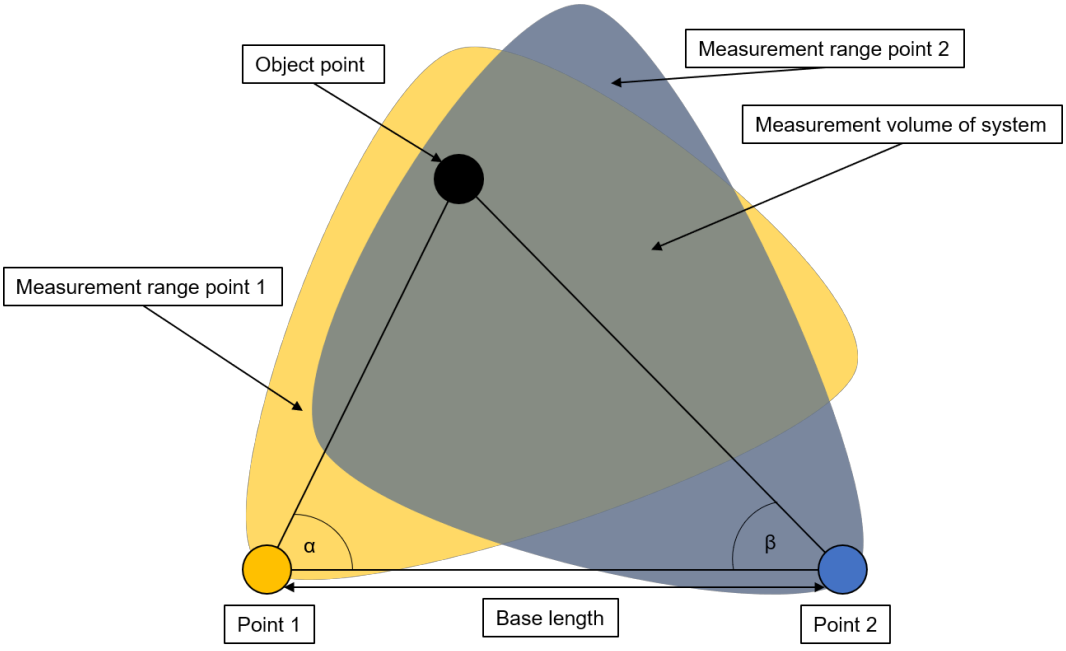

Figure 1 Sketched representation of the triangulation principle in the two-dimensional case. Adapted from [Wio-01].

An object point is to be aimed at from two different measuring points, point 1 (yellow) and point 2 (blue). Both measuring points have a range of view, which is represented

by the colored zones in Figure 1. The distance between the two points is known, as are the angles α and β. Thus, the unknowns of the triangle and thus the position of the object point can be calculated. This is only valid for the intersection of the viewing areas of the two measuring points. This basic principle is also used for the Comet. The measuring points are replaced here only by a camera and a light source. Figure 2 shows the scanner used for this work

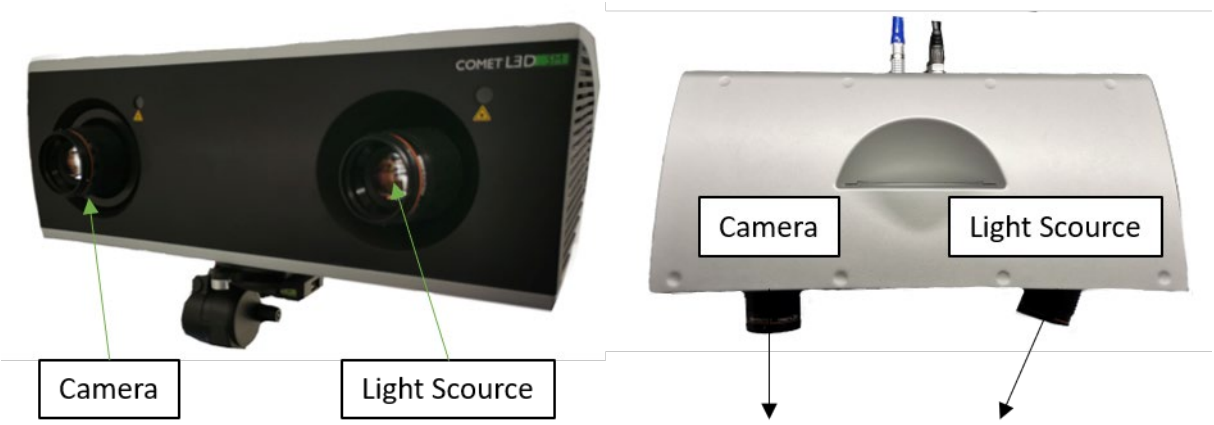

Figure 2 Comet L3D 5M stripe light scanner.

For the analogy to Figure 1, the camera of the Comet system shall be measuring point 1 and the light source corresponds to measuring point 2. Figure 2 shows that α is a right angle, because the camera is mounted perpendicular to the base length. According to the manufacturer, the angle β of the strip light projector has a value of 20°. A major difference from the Comet to the sketched representation from Figure 1 is its measuring volume. This begins only at the working distance of 73 cm. The size of the measuring volume of the Comet depends on the installed camera/light source combination, but more about this in chapter 3.1.4. In the next subchapter, a brief overview of the possible triangulation methods will be given.

3.1.2 Triangulation method

The overview of the possible triangulation methods is shown in Figure 3.

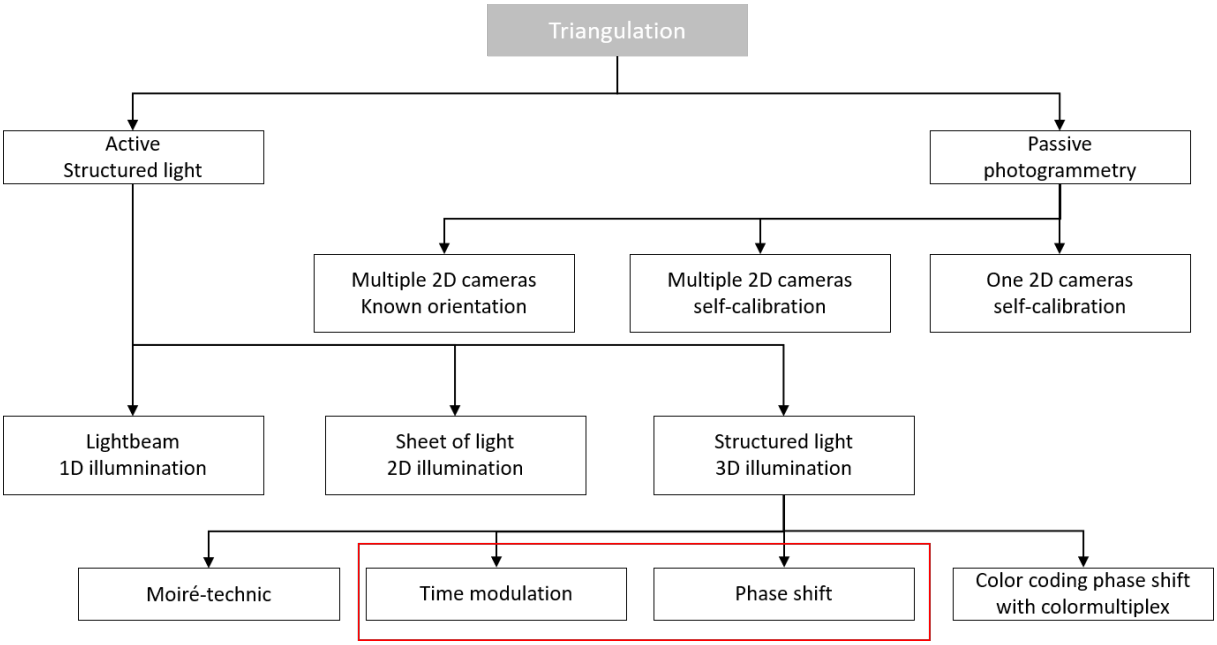

Figure 3 Overview of possible methods for optical evaluation of objects based on triangulation. Adapted from [Sch-99]

The Comet L3D uses a combination of the phase shift method and time modulation to calculate the three-dimensional point cloud. In this case, the time modulation takes place first during the scanning process, followed by the phase shift. Regarding the general measurement uncertainty, C.P. Keferstein and M. Marxer [Kef-15] provide an overview of different measurement sensors and measurement methods. This overview can be seen in Figure 4.

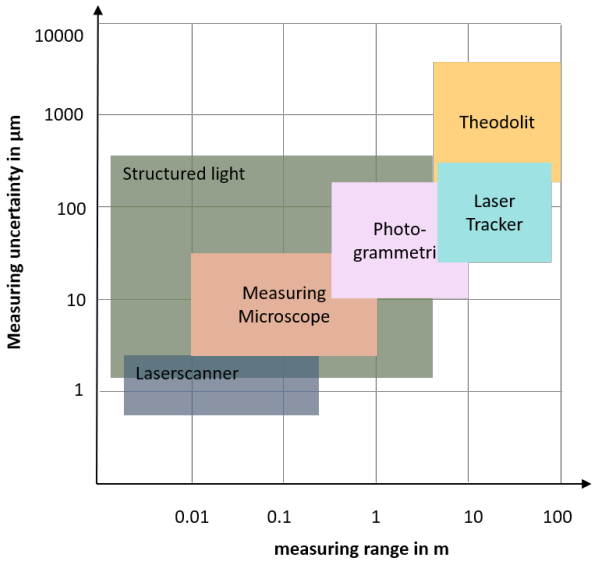

Figure 4 Overview of possible optical measuring methods for the optical measurement of objects. [Kef-15, S.199]

The comparison of the individual methods shows that the fringe projection covers a wide spectrum in terms of measurement range and measurement uncertainty. For optical systems, the measurement error also increases as the measurement volume increases. A good example of this is another system from the Zeiss company, the T-Scan. This device is a combination of laser scanner and laser tracker. This device can be used to quickly measure large objects such as a car. According to the manufacturer, the measurement uncertainty of the device is 0.033 mm + 0.033mm per additional meter. [Zei-21]. From Figure 4 it applies that not the physical limits of the respective procedures are represented, rather the representation of restrictions for the solutions available on the market takes place. [Kef-15, p 200].

3.1.3 Stripe light projection of the Comet L3D 5M

The principle of stripe light projection or fringe light projection uses at least one camera and one light source that projects a light pattern onto the object. The Comet L3D 5M works based on one camera and one light source. Newer systems, such as the ATOS III from Zeiss, use two cameras and one light source. The principle of operation remains basically the same. Figure 3 shows that the Comet uses a combination of a time modulation, the so-called Gray-code, and a sinusoidal phase shift. These two methods will be briefly explained in this chapter. The specific explanation of the calculation of the surface points of the scanned object shall be omitted, because during this project, no results or work took place in this area.

Basically, the Gray-code-method and the phase shift serve for the solution of the so-called correspondence problem. If an object point of an object surface is captured from two different viewing directions, these datasets must be matched to each other. This means that those pixels, which image the object point, must be identified in both cameras [Wio-01]. For this purpose, the two methods already mentioned are used in the Comet L3D 5M.

For the Gray-code-method, time modulated stripe light patterns (light-dark patterns), blue-black in the case of the Comet, are projected, onto the object one after the other. For each fringe pattern an image is created by the camera. Figure 5 shows an example of the Gray-code-method.

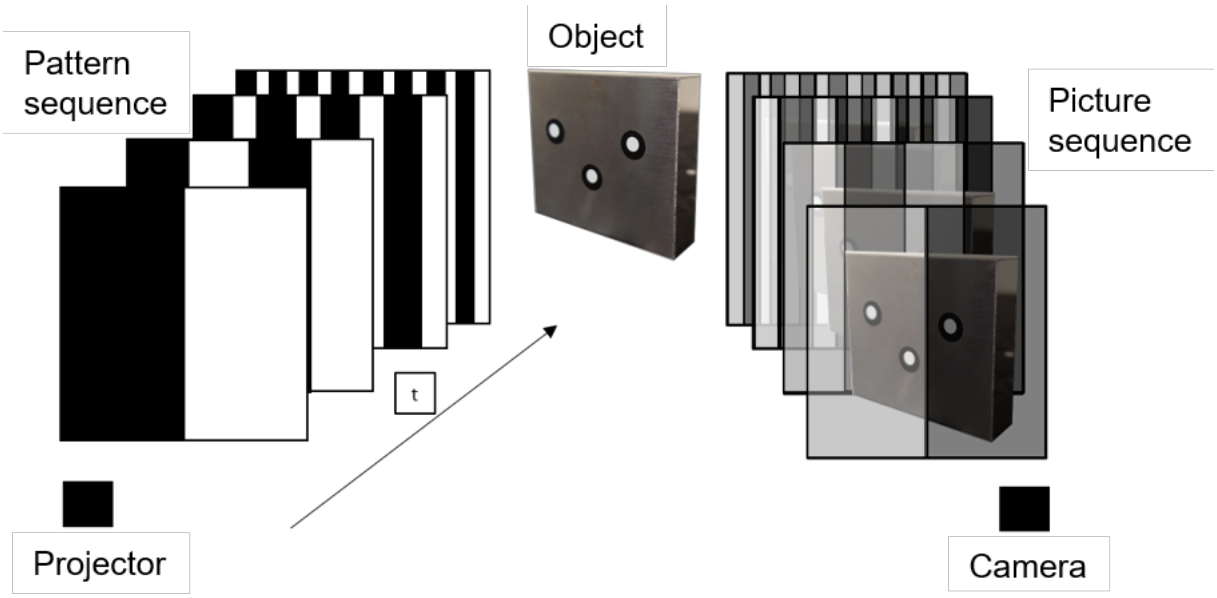

Figure 5 Schematic representation of the Gray-code-method. The transparent representation of the light-dark transitions of the image sequence was created only for this illustration.

For the calculation of the object point coordinates, the light-dark transitions of the light pattern are considered as planes. For the created images of the camera, each pixel of the image is assigned coordinates in a two-dimensional coordinate system. Based on these coordinates, a vector is created for each pixel. For the transformation of the 2D-coordians of the image into a three-dimensional space, the previously mentioned planes of the light-dark transitions are used. The intersection of the vectors with the planes creates a three-dimensional object point for each pixel. [Wio-01] Following the Gray code procedure, the phase shift procedure is performed for the Comet. This makes the assignment of the image points to the corresponding light planes more robust. In general, the phase shift method projects several sinusoidal patterns, shifted by a defined fraction of a period, onto the component [Wio-01]. In this process, the intensity is measured at each pixel [Gen-11], resulting in the same number of gray values being measured for each pixel, which are used to calculate the phase of each pixel. [Wio-01, Güh-02]. By combining the two methods, the weaknesses of each individual method can be negated, allowing accurate, fast, and robust surface measurements. [Wio-01, Güh-02, Gen-11]. The disadvantage of these methods is that the measurements are static, which means that neither the scanner nor the object may be moved during the scan.

3.1.4 Measuring-fields

During the scanning process itself, these procedures are only performed in a specific area of the camera's image. For these areas, the user receives a three-dimensional point cloud after the scan is completed. This area is not a two-dimensional surface but a volume that is called a measurement field. This volume corresponds to the overlap of the viewing area of the camera and the projector. The center of this volume is approximately 73 cm from the front edge of the scanner. The size of the measuring

field or the measuring volume can be changed on the Comet. For this purpose, different camera-projector combinations can be installed and exchanged if necessary. At the Umwelt-Campus-Birkenfeld three different measuring fields are available, whose dimensions are listed in Table 1

Table 1 Dimensions of the measuring fields available at the Environmental Campus Birkenfeld for the Comet L3D 5M

	X	Y	Z
45 measurement volume	45	38	30
100 measurement volume	120	100	60
500 measurement volume	480	400	250

Table 1 shows that the greatest limitation of the measuring fields is the Z direction. This direction corresponds to the optical axis of the scanner. For the measuring fields it is valid that the respective camera works only with the corresponding projector. Thus, for example, the camera of the 100-measuring field cannot be operated with the projector of the 45-measuring field. Within the scope of this work, the 100-measuring field was mainly used, since it represents the compromise between measuring volume and resolution. With the help of the 500-measuring field, the transfer and validation of some research results took place. The 45-measuring field was not used for this project. The difference between the 100 and 500 measurement fields is shown in Figure 6

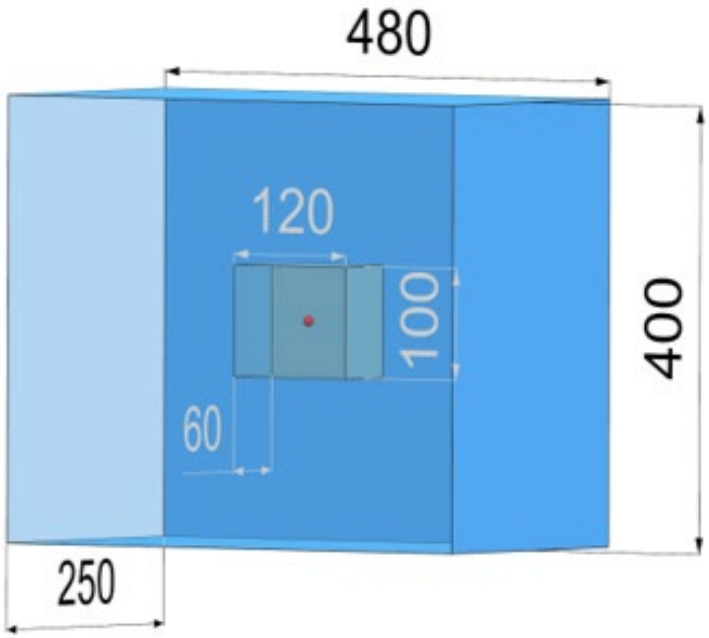

Figure 6 Schematic comparison of the measuring fields used for the Comet L3D 5M

Figure 6 demonstrates very clearly that the 500-measuring field can capture significantly more volume of a part, but it is important to note that the volumes described do not represent fixed limits for a possible part size, but only limit the areas that can be captured with a single scan. Typically, 3D measurements consist of multiple individual scans.

Due to the larger volume of the 500-measuring field, the assumption is obvious to use the 500-measuring volume as often as possible. In addition, the following facts must be explained. The cameras of the Comet, independent of the size of the measuring field, have a pixel number of 5 megapixels, hence the abbreviation 5M. Therefore, the images have a resolution of 2592 x 1944 pixels. These pixels are now evenly distributed over the length and height of the measuring volume. For example, the pixels are distributed over the length of 120 mm, resulting in a pixel spacing or point spacing of approximately 45 µm. This distance is not to be equated with the accuracy of the scanner, but is an indication of the resolution of the scanned areas. The point spacing for the 500-measuring field is thus significantly larger, whereby the scanned object surfaces appear significantly coarser compared to the same areas from a scan with the 100-measuring field.

For this work, the 100-measuring field was used because it has the best combination of measurement volume and point spacing. In addition, the objects, that will be scanned, are limited in volume or size by the size of the vacuum chamber so that they can be evaluated time-efficiently with the 100-measuring field. In the context of this work, however, it is examined to what extent the accuracy of the 500-measuring field differs from that of the 100-measuring field. In general, the choice of the measuring field is a decision between efficiency, object size and accuracy. Due to the possibility of changing the measuring field, a combination of 3D scans with the help of different measuring fields is also possible, so that, for example, large objects can be fully digitized with the 500-measuring field, and by changing to the 100-measuring field or even 45 measuring field, the measurement of areas that are subject to special tolerances, for example, is then carried out.

3.1.5 3D-Scan process

This chapter describes the most important processes during 3D scanning and defines terms that are important for the rest of this thesis. The procedures and conditions described up to this point are the theoretical background for the three-dimensional optical measurement of an object-surface. This chapter explains the practical procedure of a 3D scan.

Mendricky et al. [Men-16] showed the significant influence of the time of the last calibration on the results of a 3D scanner. For this reason, the calibration of the Comet is described. For the calibration, a calibration field is needed, which can be seen in Figure 7.

Figure 7 Calibration field for the 100 and 45 measuring field

This field was manufactured and measured by the manufacturer Zeiss, so that the distances between the points are known exactly. This data is available to the scanning software as references and is used for comparison during calibration. The three somewhat larger points in the center of the field, which have an L arrangement, serve as an aid to the user during the calibration process. For calibration, the user must take a total of eight measurements, which must be done using the positioning guide shown in Figure 8. It is important that the eight measurements are performed one after the other and that the calibration field is also rotated according to the illustrated instructions. In addition, the scanner must not be moved between the eight measurements.

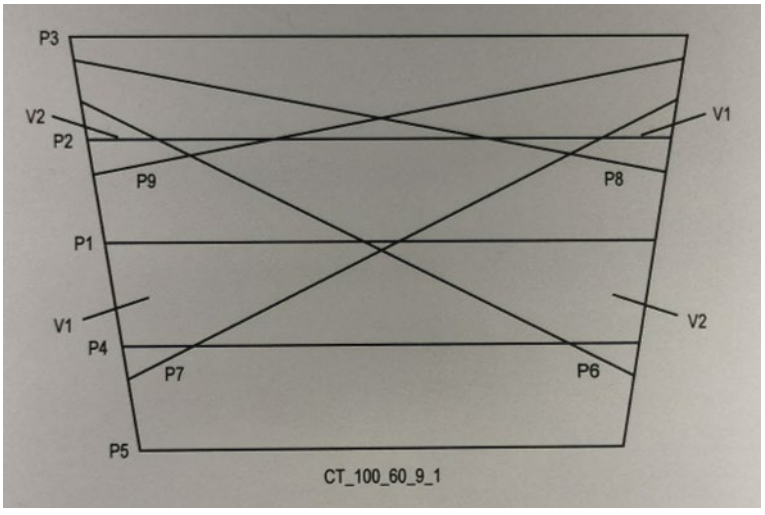

Figure 8 Calibration instructions for the 100-calibration field

The positions of the calibration field shown in Figure 8 correspond to the limits of the respective measuring field. This ensures that the scanner will function properly in all

areas of the scan volume. The user has only two adjustment options during calibration. Firstly, he can set the exposure time, and secondly, the contrast. The last option is only available to the user during calibration. The exposure time must be selected so that a result, as in Figure 9, is obtained.

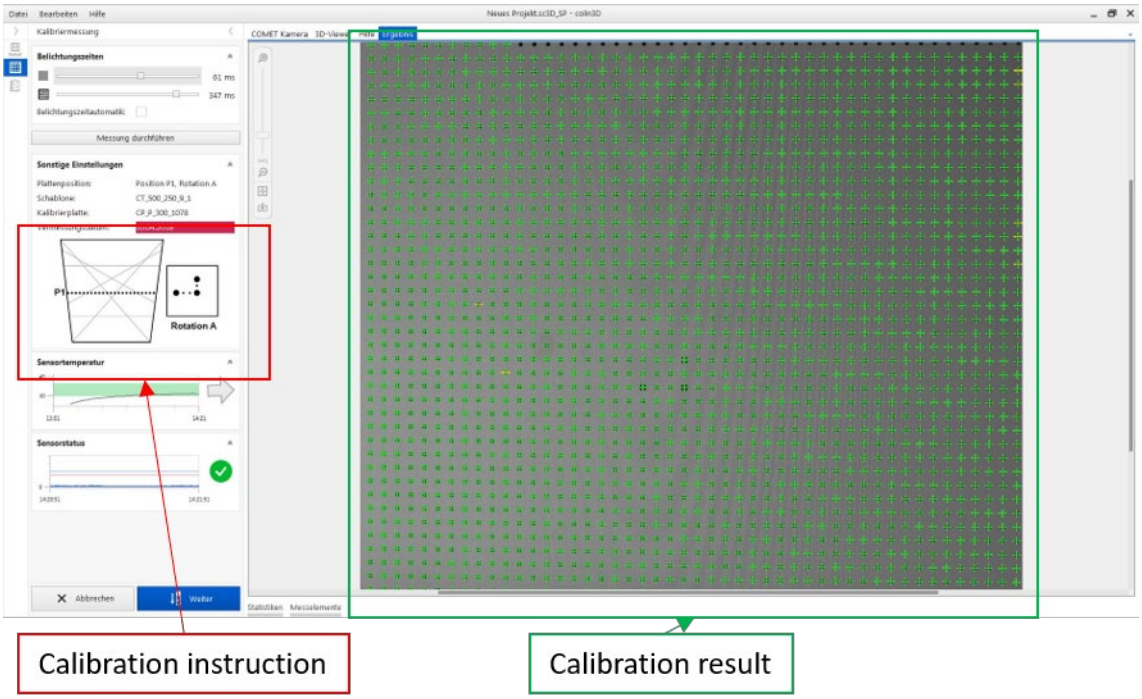

Figure 9 Result from one of eight scans during calibration of the scanner.

The aim of the eight measurements is to obtain a result, as shown in Figure 9. After the eight scans have been completed, the calibration can be finished. After a successful completion of the calibration, the measurement of an object can be started. For the results of this work, care was taken to calibrate the scanner before each large series of experiments. If a test series lasted longer than three days, a new calibration was performed. This can be used to counteract the findings of [Men-16].

The full-scale measurement of a component using a 3D scanner basically involves the constant repetition of two process steps. For a better understanding, the process will be explained by means of an example. Figure 10 demonstrates the example.

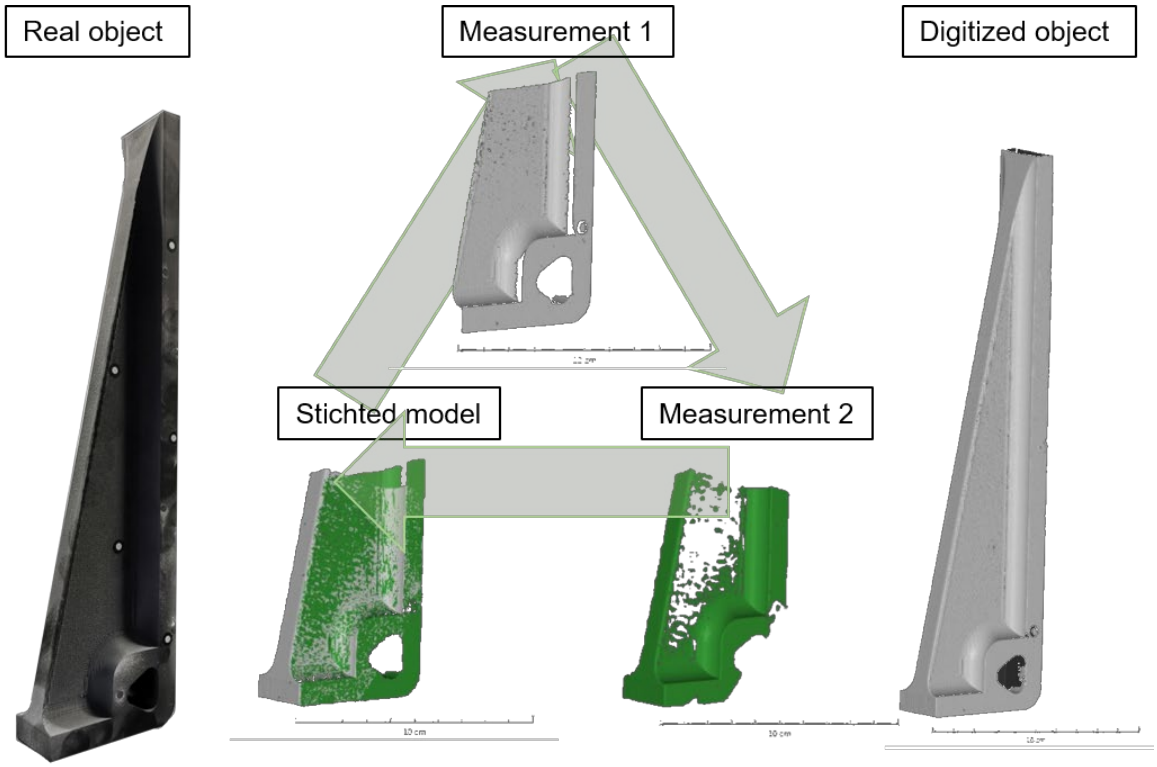

Figure 10 Schematic representation of the process steps for the complete measurement of an object using a 3D scanner

The first important process step is the scanning itself. For this purpose, a three-dimensional point cloud of the object visible in the measurement field is generated with the aid of the methods described. This corresponds to measurement 1 in Figure 10 and is a single measurement. Figure 11 shows a Gray-code pattern and the phase shift during the scanning process.

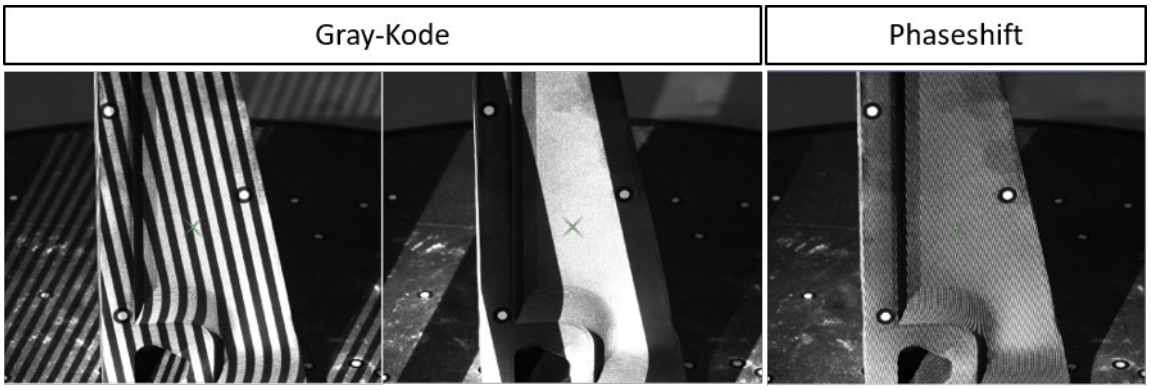

Figure 11 Gray code pattern and phase shift pattern on a component during the scanning process.

Subsequently, either the scanner or the object is moved so that additional surfaces become visible in the measuring field of the scanner. Another single measurement is then taken, corresponding to image 2 in Figure 10. Now comes the second important process step of the 3D scan, the so-called "stitching" process. The two individual measurements are connected by the scanning software searching for areas that were captured in both measurements. By mathematically superimposing the respective object points, the two individual measurements are aligned with each other. This is

shown in Figure 10 by the stichted model. This process must be manually controlled by the user depending on the object. For objects with distinctive surfaces and easily identifiable geometries, the software manages this process automatically. For objects that have a simple topology, such as cylinders, the software needs instructions from the user. This manual instruction can also be automated with the help of measurement marks. The measurement marks used for this work are small circular black and white stickers that are automatically detected by the software under the correct exposure times and used for the stitching process.

Subsequently, another single measurement is created and added to the existing point cloud via the stitching process. The user repeats this until the object is scanned as completely as possible, which is demonstrated by the digitized model in Figure 10. The point cloud can be converted into a polygon body within the scanning software, e.g., to close holes or reduce the number of points. The user also has the option to export the scanned data directly as an STL file without converting it into a polygon body. For this work, the scanned data was written directly to STL format to avoid possible data loss due to polygon body creation. When exporting data to STL format, the user has no setting options.

Subsequently, it can be stated that a 3D measurement can either consist of a single measurement (single view) or of several measurements (multiple views). In the course of this work, it will be investigated whether this makes a difference to the accuracy of the 3D scanner. The background is the consideration that components can only be rotated in a vacuum with a high effort. A movement of the scanner should be avoided for measurements under space conditions due to the refraction laws of the optics, which are explained in chapter 3.3.

3.1.6 Definition accuracy

DIN ISO 5725-1:1997-11 [DIN-97] defines the term accuracy for measurement procedures and measurement results. According to the standard, the accuracy of a measurement or measurement procedure is composed of the trueness of the measurement and the precision of the measurement. The precision describes the fluctuation of independent measurement results, during the same unchanged measurement procedure, to each other [DIN-97]. The accuracy reflects the difference between a previously defined reference value and, for example, the determined arithmetic mean of a large series of measurement results [DIN-97]. A good example is a shooter who wants to hit a certain target with five attempts. Figure 12 describes how precision and accuracy can be applied to this example.

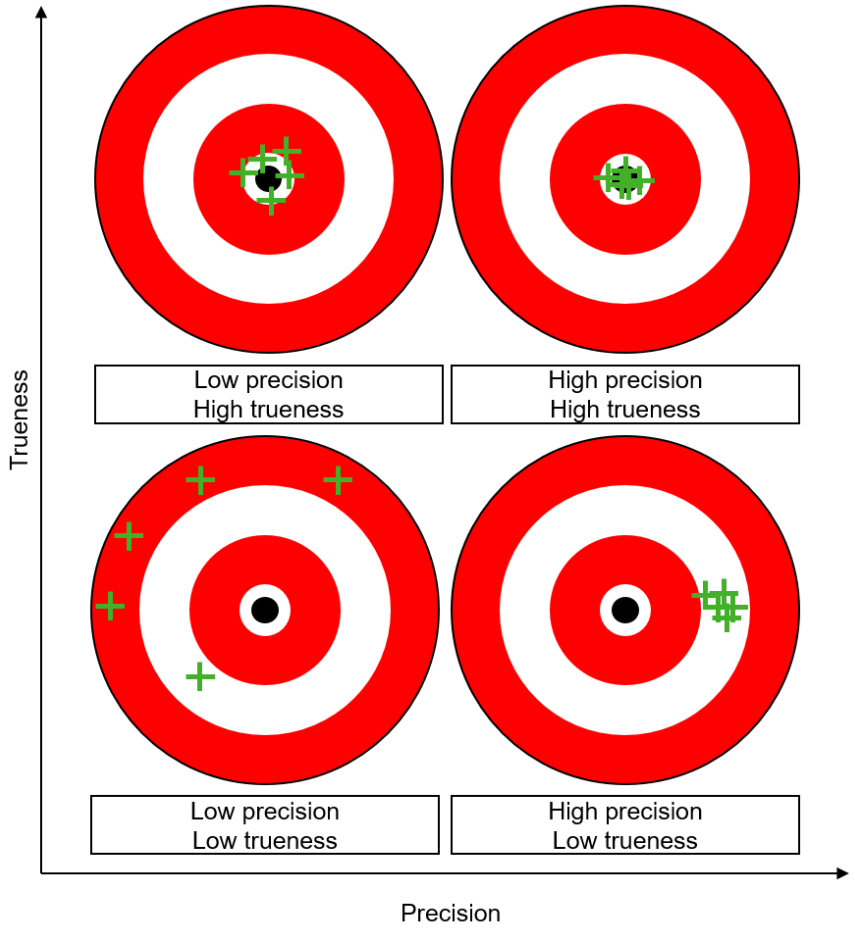

Figure 12 Example for the better representation of the term's trueness and precision. Adapted from the [DIN-97]

The wish of every user is that the measurement methods used or the measurement results obtained have a high precision and accuracy. Both terms provide only qualitative information [DIN-97]. For a quantitative statement, the measurement uncertainty is used [DIN-97]. The trueness of a measurement or a measurement procedure is represented as a systematic deviation component and the precision as a standard deviation [DIN-97]. The evaluation of the measurement uncertainty is based on a statistical evaluation and can therefore be carried out according to "GUM determination Method A" [Gum-93]. The variance is calculated by the following formula. Here n is the sample size, q_j the characteristic expression, and $\bar{q}$ the mean value of the sample.

Equation 1 Calculation formula for the variance according to [Gum-93].

$$s^2(q_k) = \frac{1}{n-1}\sum_{j=1}^{n}(q_j - \bar{q})^2$$

The standard deviation s or σ can be calculated from the variance with Equation 2.

Equation 2 Calculation formula for the standard deviation according to [Gum-93]

$$\sigma(q_k) = \sqrt{s^2}$$

Since the determination of the measurement uncertainty in this work is a statistical evaluation, it is assumed that the measured experimental values can be described by a normal distribution. Furthermore, a confidence interval of $k = \pm 2\sigma$ shall apply to the measurement procedure. Where σ is equal to the standard deviation. This means that the accuracy limits determined within the scope of this work apply to 95% of all measurement results carried out

3.1.7 Analysis of the scan data

For the determination of the accuracy of optical measuring systems, several procedures are described in VDI Guideline 2634 [VDI-08a-c] and DIN EN ISO 10360-13:2020-07 [DIN-20]. The measurement procedures are the same in both guidelines, which is why only the abbreviated form of the DIN standard will be referred to for the literature references. For the Comet, VDI Guideline 2634-3 [VDI-08c] and [DIN-20] must be referred to. The three methods described are:

- Probing deviation
- Sphere distance deviation
- Length measurement deviation

For this work only the length measurement deviation is of importance, thus only this method will be explained. The aim of the parameters of VDI 2634-3 and [DIN-20] is to check the errors of the individual measurements and to show the errors of the "stitching" process. For this reason, the test specimens are always measured from several views and positions. The length measurement deviation is calculated with the aid of the spherical dumbbell bar or a gauge block. The sphere dumbbell bar consists of two spheres of the same size, which are held together by a connecting piece. The diameter of the spheres as well as the distance of their center-point were measured exactly with a coordinate measuring machine. This also applies to the length of the gauge block.

For this work, a gauge block is used at the beginning to record the general accuracy of the scanner and the influence of various parameters on the measurement result. The measurements are to be carried out according to the VDI guideline 2634-3 and [DIN-20]. For this purpose, the gauge block must be measured from several positions. Figure 13 demonstrates the individual measuring positions.

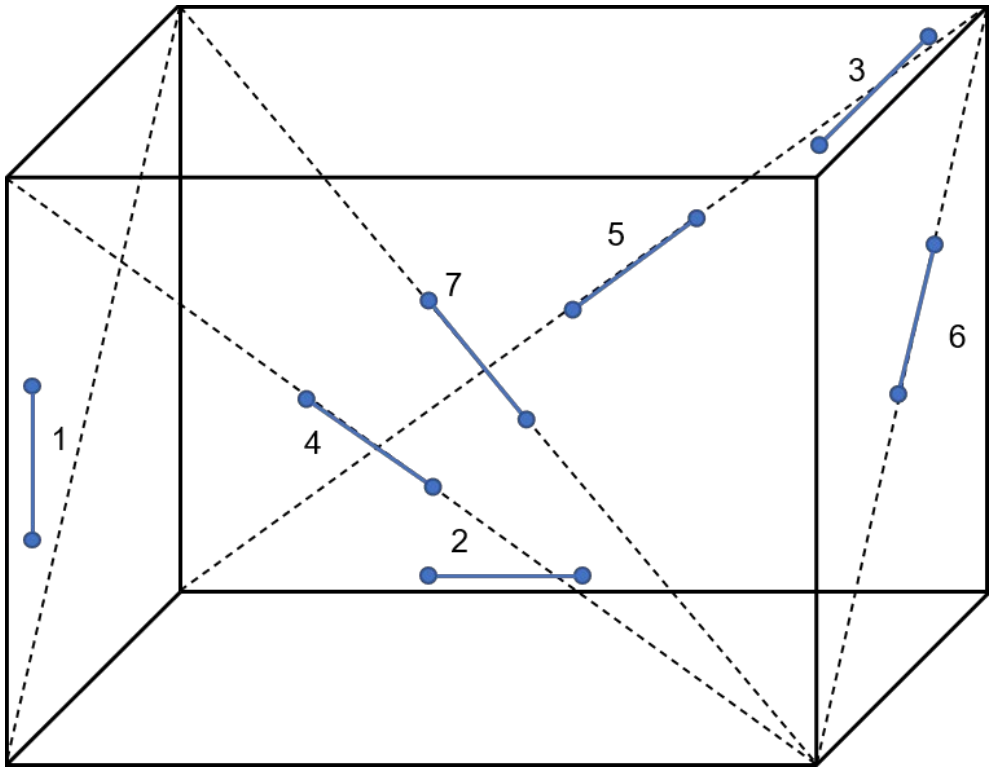

Figure 13 Recommendation for the arrangement of the test specimen for the determination of the length measurement deviation [VDI-08c].

The rectangular space shown in Figure 13 does not correspond to the measuring field of the scanner, but to a combination of individual scans, which create a measuring volume that is at least twice as large as the measuring field of an individual scan. The gauge block should have a length of 2/3 of the spatial diagonal of the combined measuring volume, which equals a length of 190 mm for the 100-measuring field of the Comet. For the evaluation of the length of the gauge block, two opposite points are used, which are located as centrally as possible on the relevant surfaces of the gauge block. Explicitly, only one single point per surface may be selected [VDI-08c].

Several practical problems arose for this work from the requirements of VDI-2634-3 [VDI-08c] and [DIN-20]. The first practical problem arose from the fact that the gauge block could only be measured from a single position from multiple views due to the high reflectivity of the polished surfaces. Therefore, no six other setups could be performed. Another problem is posed by the subsequent experimental setup for investigations under space conditions. With a length of 190 mm, the theoretical component is too large for experiments in the vacuum chamber. It follows from this that the investigations carried out in this work are only an adaptation of VDI-2634-3 and [DIN-20].

For the evaluation, compensation planes were created in the evaluation software for the relevant surfaces in each case, with the help of which the point distance measurements for the length of the gauge block were carried out. An outlier tolerance can be specified as part of the plane creation process. The center points of the created planes form the respective points for the length measurement.

3.2 Vacuum technology

This chapter is intended to provide a brief overview of the relevant areas of vacuum technology. Vacuum is generally understood to mean a space in which the pressure is lower than atmospheric pressure. According to DIN 28400-1:1990-05 [DIN-90], vacuum is defined when the pressure of a room gas and its number of particles is lower than the number of particles outside the room. Or when the pressure of the room gas is lower than 300 mbar, as this is the lowest atmospheric pressure on the earth's surface. [DIN-90]. Figure 14 gives a good overview of the different vacuum ranges and relates them to space astrophysics and atmospheric physics.

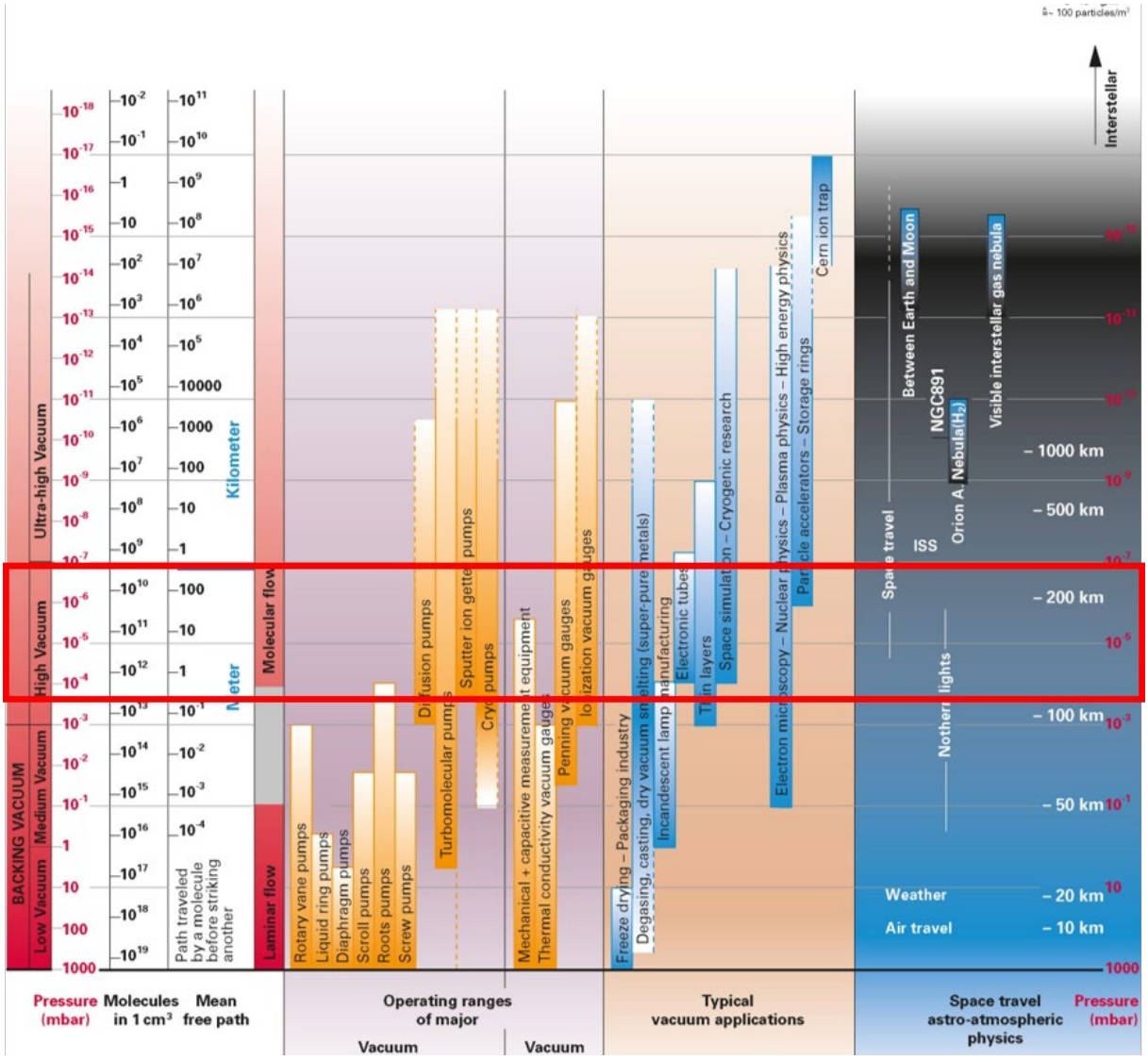

Figure 14 Presentation of vacuum classification with reference to pumps used, areas of application and comparison to space travel and atmospheric physics [Pfe-13]

The area marked in red in Figure 14 represents the vacuum range that can be achieved in the vacuum facility at the environmental campus. Thus, the vacuum achieved is just at the lower limit of space technology and in the range of molecular flow.

For the explanation of the concept of molecular flow, the subject of the mean free path length and the so-called Knudsen number must first be introduced. The mean free path

length $\bar{l}$ is the distance of an atom between two successive collisions. This distance is of different length, due to statistical particle motion [Wut-06, p. 39]. The distance traveled depends on the particle diameter d_t of the atom, the temperature T, and the pressure p. Equation 3 can be used to determine the mean free path $\bar{l}$.

Equation 3 Calculation formula for the mean free path [Wut-06, p. 40].

$$\bar{l} * p = \frac{k * T}{\sqrt{2} * \pi * {d_t}^2}$$

k is the Boltzmann constant[1]. To illustrate the mean path. $\bar{l}$ the following simple example shall serve [Wut-06]:

A fictitious air particle[2] has a diameter of 0.37 nm. At a temperature of 20°C, from Equation 3:

$$\bar{l} * p = \frac{1{,}380 * 10^{-23} J * K^{-1} * 293\ K}{\sqrt{2} * \pi * (0{,}37 * 10^{-9} m)^2}$$

$$\bar{l} * p = 0{,}0066\ m * Pa$$

For atmospheric pressure of $10^5 Pa$, $\bar{l}$ is 66 nm long. In high vacuum at $10^{-4} Pa$ the distance is 66 m. Since most vacuum chambers don't have such a large wall distance, the atoms inside the chamber only collide from wall to wall. It follows that there is no contact between the individual atoms in the volume of the chamber, and thus, there is no mass transfer for thermal energy and frictional forces [Wut-06]. This describes a molecular flow. The Knudsen number Kn is the ratio between the mean free path length $\bar{l}$ and the diameter d of the conductor cross section. This is shown in Equation 4.

Equation 4 Calculation formula for the Knudsen number Kn [Wut-06, p 67].

$$Kn = \frac{\bar{l}}{d}$$

The Knudsen number can be used to classify the flow types [Wut-06, p. 68]. It is:

$$Kn > 0{,}5 \rightarrow molecular\ flow$$

$$0{,}5 > Kn > 0{,}01 \rightarrow Knudsen\ flow$$

$$Kn < 0{,}01 \rightarrow viscose\ flow$$

This means that at low pressures, such as those in a vacuum, there is a large Knudsen number.

Under normal atmospheric conditions, heat is transported by three mechanisms: thermal radiation, convection, and conduction, which are intermixed. Thermal radiation

[1] $k = 1{,}380 * 10^{-23} J * K^{-1}$ [Wut-06]

[2] In [Wut-06], a fictitious air particle is calculated via the partial fraction of air, with which simplified calculations can be made. These simplifications are adopted for this example.

is based on the fact that any physical body with a temperature above zero Kelvin emits thermal energy in the form of electromagnetic waves. This means that thermal radiation transfers thermal energy between two bodies without material. Thermal radiation can be transmitted, reflected, or absorbed. The following equation describes the physical relationship of these quantities, where ε describes the absorbed, τ the transmitted, and r the reflected component:

Equation 5 Law of conservation of energy of thermal radiation [Tip-19]

$$\varepsilon + \tau + r = 1$$

According to the law of conservation of energy, the addition of all quantities must yield the result 1. It should be noted that a body emits thermal radiation in all spatial directions. If thermal radiation hits a body, the absorbed radiation increases the internal energy of the body and causes a temperature increase.

The term convection describes the transfer of thermal energy via a transfer medium, e.g., air or water. This involves physical contact between the transfer medium and the heat-emitting body. Through this contact, the internal energy of the body is transferred to the transfer medium. Heat transfer by contact is called thermal conduction. The heated transfer medium then transfers the heat to other bodies with which it comes into contact.

In a perfect vacuum, heat energy can only be transferred by thermal radiation and thermal conduction since there is no transfer medium in the vacuum or, at low vacuums, the transfer medium has only molecular material flows, which means that contact among the individual atoms is statistically absent. Thus, there is no convection in the vacuum.

3.3 Scientific fundamentals

For the later raytracing approach, some basics of vector algebra and optics are needed, which will be briefly described in this subchapter. For the vectorial consideration of the point displacement, the following formulas are needed. Here $\vec{a}$ and $\vec{b}$ are two vectors, and i describes the included angle between the two vectors. This angle can be calculated with Equation 6

Equation 6 Calculation of the included angle between two vectors [Pap-14].[3]

$$\cos(i) = \frac{\vec{a} * \vec{b}}{|a| * |b|}$$

The relationship between sine, cosine, and tangent is described in Equation 7 and is relevant for the later calculations.

[3] The * indicates a simple multiplication.

Equation 7 Relationship between tangent, sine, and cosine of an angle [Pap-14].

$$\tan(i) = \frac{\sin(i)}{\cos(i)}$$

The refraction of a light beam at a transparent boundary surface is determined with the help of Snellius' law of refraction. Figure 15 shows a schematic example of a plane-parallel plate.

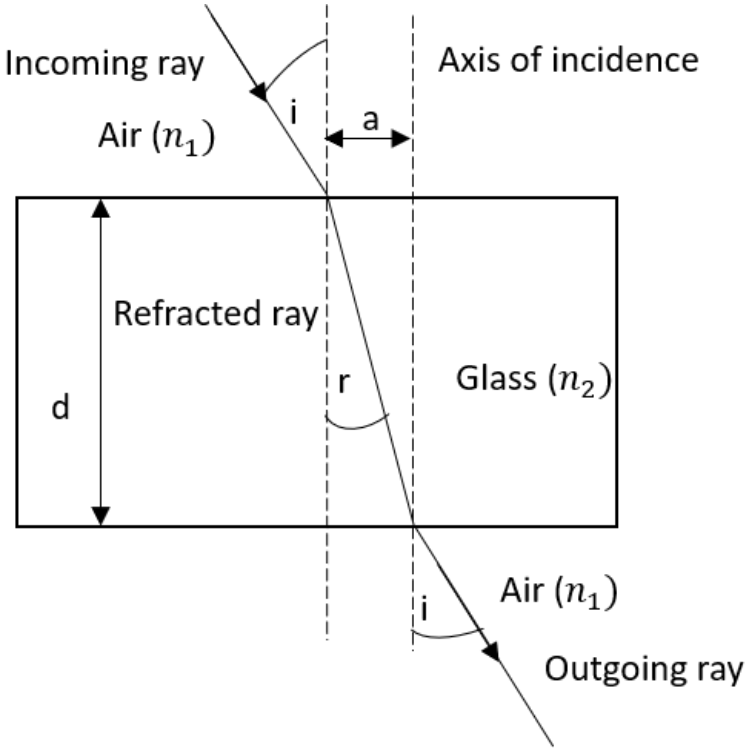

Figure 15 Sketch for Snellius' law of refraction on a plane-parallel plate. Adapted from [Tip-19]

n_1 and n_2 are refractive indices which can usually be read from material tables for the respective materials. The refraction law of Snellius is based on the input angle i of the light beam and the output angle r of the refracted beam. With the help of the refractive indices, the equation from Equation 8 can be set up.

Equation 8 Snell's law of refraction. [Tip-19]

$$\sin(i) * n_1 = \sin(r) * n_2$$

The offset a of the incoming and outgoing beam shown in Figure 15 can be determined with the help of the calculated refraction angles i and r as well as the thickness d of the plane-parallel plate based on the following formula.

Equation 9 Optical displacement of the incoming and outgoing beam through a plane-parallel plate. [Tip-19]

$$a = d\,\frac{\sin(i) - \sin(r)}{\cos(r)}$$

Furthermore, continuity considerations and optical application of Maxwell's equation are important for the calculation of the displacement. The light from the scanner is assumed to be a transverse plane monochromatic wave for the calculations. This

allows the light beam to be split into a tangential and perpendicular part at the boundary surface, in this case, the glass pane. The following applies:

Equation 10 Division of a beam into tangential and perpendicular components [Kon-11, p.48]

$$\vec{s} = \overrightarrow{s^{\parallel}} + \overrightarrow{s^{\perp}}$$

This formula is also valid for the refracted beam after the interface. Furthermore, the incident of refracted and reflected parts of the wave vector tangential to the interface must be equal everywhere on the interface. [Con-11]

Another important formula for this work is the calculation formula for the linear thermal expansions ΔL v of components. For the calculation, the coefficient of linear expansion α of the material under investigation is required. This material characteristic value can be obtained from material tables. With the aid of the temperature differential, ΔT and the initial length, L_0 the linear expansion can be calculated via Equation 11.

Equation 11 Calculation of linear thermal expansion [Tip-19]

$$\Delta L = \alpha * L_0 * \Delta T$$

3.4 Design of Experiments (DoE)

The statistical design of experiments describes a methodology for the construction of experimental designs. In contrast to the conventional methodology in which the parameters are changed only one after the other and the rest is kept constant, in the statistical design of experiments several parameters are varied simultaneously. In order to use DoE, it is necessary to define several terms.

The term system describes the entity on which the DoE is applied. A system has input variables, which can be changed by the system itself, as well as input variables, which cannot be changed because they belong to another system [Sie-17, p.3]. The output of each system is results.

The results of a system are called quality characteristics in the DoE and must be continuous sizes so that the later computations of the DoE can take place [Sie-17, p.4]. Systems are analyzed in terms of the quality attributes. For example, in the case of 3D scanning, the quality attribute to be analyzed would be accuracy. The input variables are defined as parameters [Sie-17, p.5] and those parameters that are investigated in the DoE are called factors [Sie-17, p.5] Factors must be reproducible and must not be mutually exclusive, since the DoE requires that each trial of the experimental design be worked through. [Sie-17, p.5]. The settings of the factors in the course of the DoE experiments are called levels. Each factor must have at least two levels. [Sie-17, p.6] When choosing the settings or the levels of each factor, the different combinations of all factors must still produce results. As an example of a possible factor, the exposure time of the scanner shall serve. This can be set specifically in the scanning software and two possible levels would be, for example, an exposure time of 300 ms and 600

ms. Further factors would be e.g. the ambient exposure, the time of the last calibration, or the exposure angle of the object.

In the context of this work, a DoE was performed based on a so-called full factor plan. This means that every possible combination of the tested factors was tested and evaluated. The presentation of the test plans of the DoE is done with the help of a normalization. The levels are represented, for example, by a "+/-" or "-1/1". The factors are abbreviated with letters (ABC). The examined quality characteristics are also represented with letters (xyz). An example of a full factor test plan can be seen in Table 2

Table 2 Example of a full factor test plan with 3 factors each having 2 levels. Derived from [Sie-17, p.19].

	factor			quality characteristic
trial number	A	B	C	x
1	-	-	-	x_1
2	+	-	-	x_2
3	-	+	-	x_3
4	+	+	-	x_4
5	-	-	+	x_5
6	+	-	+	x_6
7	-	+	+	x_7
8	+	+	+	x_8

Full factorial experimental designs usually require a large amount of time but also provide the clearest results [Sie-17, p.31]. The results of a DoE evaluation are the effect and the interactions. The effect describes the influence of a factor on the quality characteristic [Sie-17, p. 12]. The interaction demonstrates how strongly the effect of a factor depends on the settings of another factor. [Sie-17, p.15]. The significance of the evaluation of a DoE depends on the size of the experimental design; with a large experimental design, such as the full factor plan, the most accurate statements about effect and interactions can be reproduced [Sie-17, p.31]. The DoE has a variety of experimental design models, which can be found in the literature and will not be discussed in this thesis.

The calculation of the effect of a factor is done by the mean values of the quality characteristic of the stages of the respective factor. The order and normalizations from Table 2 apply to Equation 12.

Equation 12 Calculation formula for the effect of a factor [Sie-17, p.12]

$$E_A = \frac{x_2 + x_4 + x_6 + x_8}{4} - \frac{x_1 + x_3 + x_5 + x_7}{4}$$

The interpretation of the effect of a factor can be made by effect diagrams. An example is shown in Figure 16. The values calculated with Equation 12 correspond to the gradients of the respective graphs. [Sie-17, p.14]

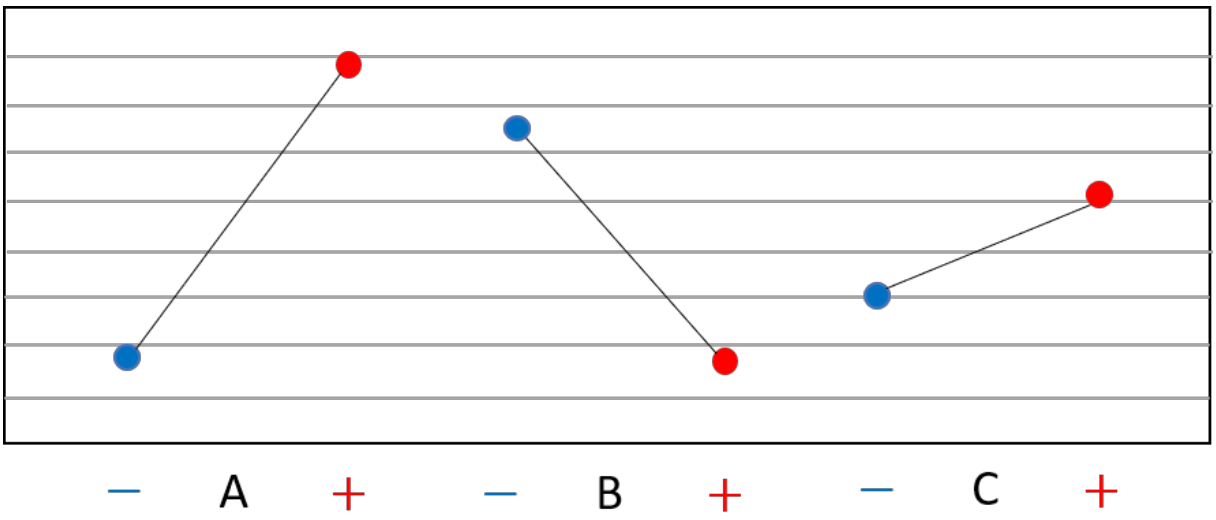

Figure 16 Example of an effect diagram from [Sie-17, p. 14].

The calculation of the interactions is carried out according to the principle of the effect calculation however, the possible interactions between the factors must be recognized beforehand. For this purpose, interaction columns are inserted in the experimental design. These describe whether the respective factors are on the same (+) or unequal (-) level [Sie-17, p. 17]. For plans with more than two factors also multiple interactions can occur [Sie-17, p.19]. For these columns, a different "construction rule" must be applied. For this purpose, the levels of the respective factors and twofold interactions must be multiplied with each other line by line. This leads to the fact that from the multiplication of "+" and "-" a "-" follows.

The interaction columns will be demonstrated in Table 3 for the example of Table 2. The presentation of the experiment numbers is omitted in this table.

Table 3 Full factor plan from Table 2 incl. the interaction columns.

factor			interaction effect				quality characteristic
A	B	C	AB	AC	BC	ABC	x
-	-	-	+	+	+	-	x_1
+	-	-	-	-	+	+	x_2
-	+	-	-	+	-	+	x_3
+	+	-	+	-	-	-	x_4
-	-	+	+	-	-	+	x_5
+	-	+	-	+	-	-	x_6
-	+	+	-	-	+	-	x_7
+	+	+	+	+	+	+	x_8

For the calculation of the interactions, the following formula can be used now. Here E_A is the effect of the factor A and E_{AB} is the effect of the interaction column AB. Both values are calculated with Equation 12. The interactions can be calculated with Equation 13

Equation 13 Calculation formula for the interaction effect of a factor. [Sie-17, p.18]

$$E_{A(B-)} = E_A - E_{AB}$$

$$E_{A(B+)} = E_A + E_{AB}$$

The values calculated with Equation 13 correspond to the gradients of the interaction diagrams [Sie-17, p.18]. An example of such a diagram can be seen in Figure 17.

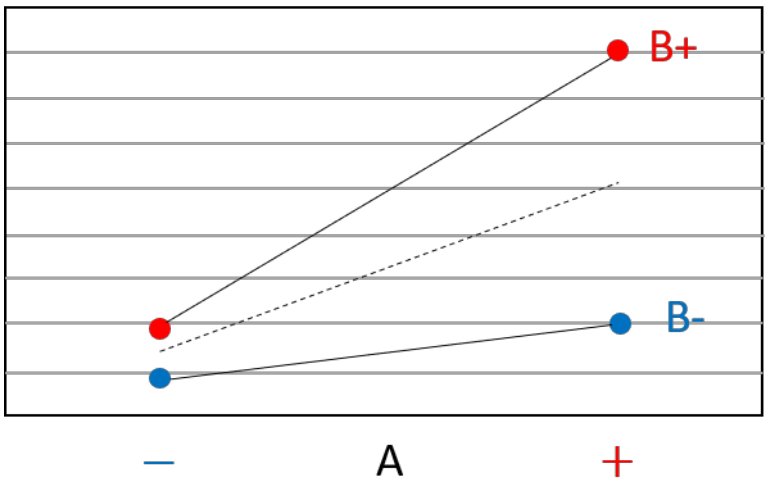

Figure 17 Example of an interaction diagram. The dashed line describes the main effect of factor A. Adapted from [Sie-17, p.18].

The interpretation of the interactions is clearly more complex than that of the effects, therefore, no direct explanation can be supplied in this part. However, in principle,

parallel lines indicate a weak interaction effect. Crossed lines demonstrate an opposite interaction effect. [Sie-17, p.18]

4 Methods and materials

In this chapter, the general procedure and the used experimental setups are described and explained. First, the general procedure is described, and then the investigated objects are presented. During subchapter 4.5, the construction and modification of the vacuum chamber are described, which is required for the initial environmental requirements of the measurement procedure. This is followed by a description of the respective experimental setups. Finally, the applied evaluation methods are described and explained.

4.1 General procedure

As described briefly at the beginning, this project follows the approach of starting with simple facts and then making them more complex step by step. An overview of the general procedure for this work and its experiments can be seen in Figure 18.

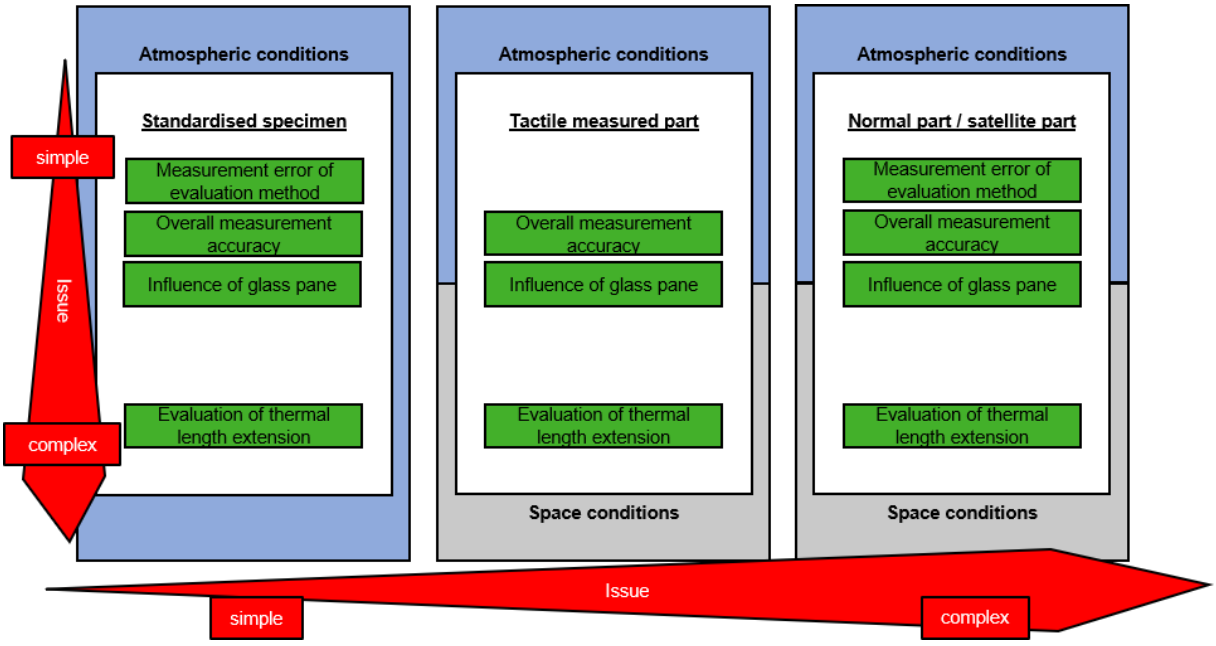

Figure 18 Presentation of the general procedure during the project.

By this approach, the obtained results form foundations for the further results. Without the derivation and presentation of the simpler results, a clear and meaningful evaluation of the more complex experiments is not possible. Furthermore, by deriving the results based on very simple facts and standardized components, the effect of the increasingly complex circumstances can be better determined and more clearly distinguished from each other.

The cornerstone of the project is the assurance and verification of the evaluation procedure, after which the general measurement accuracy of the scanner is

determined on the basis of a standardized component. Best practice parameters will be worked out. This elaboration is done first by a conservative test procedure and is subsequently verified by means of a DoE. Afterward, the influence of the glass pane is analyzed using the same test body. The last step for the normalized bodies is the evaluation of the linear thermal expansions or the verification weather linear thermal expansions can be detected with a 3D scanner. All these steps are performed under atmospheric conditions.

The next step is to switch to a tactile measured component. This is used to measure an object that is subject to general manufacturing tolerances. The tactile measurement can be used to define nominal values for selected form elements, which are then used to determine the systematic bias. For this component, the results obtained using the standardized test specimen are checked, validated, and extended. Following this, the first tests are carried out in the vacuum chamber to determine the influence of the glass pane used. Finally, the linear thermal expansions of the component through a glass pane are measured and evaluated under space conditions.

In a final step, the results and findings obtained so far are applied to general components or satellite components. These components have unknown actual dimensions and manufacturing tolerances. For these components, partly new evaluation methods are applied so that they must be evaluated first. Subsequently, the general measurement accuracy and the influence of the glass pane are checked under atmospheric conditions. Finally, the linear thermal expansion is evaluated under space conditions. Based on the results of the satellite components, a direct statement can be made about a possible application of the developed evaluation method.

4.2 Components

This section presents the used objects. The standardized test specimens are a test sphere and a 40 mm gauge block. Examples of gauge blocks and the test sphere used for this project are presented in Figure 19.

Figure 19 Standardized test specimens. L. Parallel gauge block R. Test sphere.

When purchasing a parallel gauge block, the buyer receives a certificate stating the exact width of the gauge block. The exact actual dimension of the gauge block used in this work is 40.0004 mm. The test sphere is used to calibrate another 3D scanner (T-

Scan) from the company Zeiss. Again, the exact size is known by a tactile measurement, which was done by the company Zeiss. The exact diameter of the sphere is 49.992 mm. Figure 20 shows the relevant dimensions of the two bodies schematically.

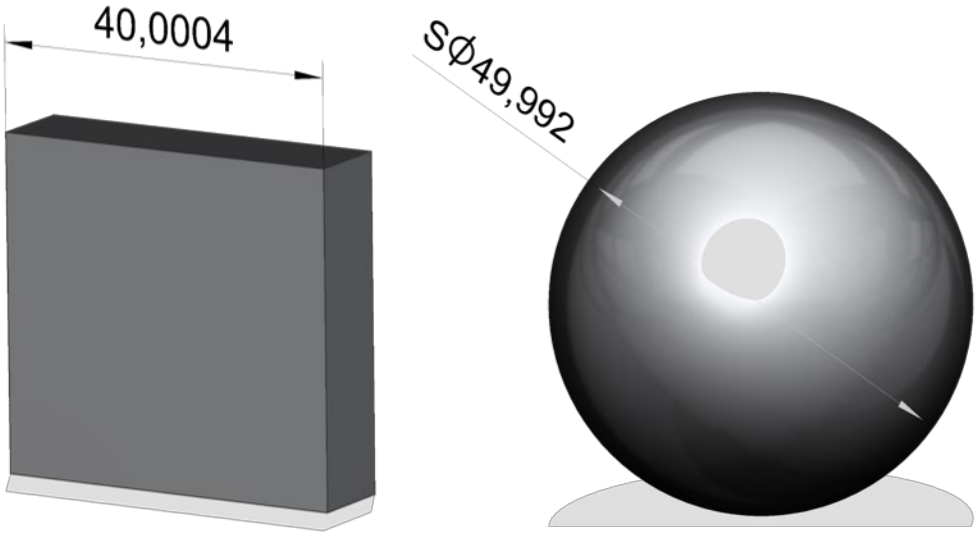

Figure 20 Representation of the actual dimensions of the standardized measuring bodies

Both bodies can be used for accuracy verification for 3D scanners according to [VDI-08c] and [DIN-20]. For this work, a steel gauge block was used, which with its reflective lateral surfaces is considered a "worst case" scenario for 3D scanning. For this reason, the surveying strategy requirement of [VDI-08c] and [DIN20], as already described in Chapter 3, could not be met either, which is why the tests performed are all based on the VDI guideline and DIN standard, respectively. Based on the gauge block and the test sphere, the evaluation procedure, the general accuracy, and the influence of the glass pane were checked. The recording of the linear thermal expansions was determined only for the gauge block. The gauge block was also used to check the results for the 500-measuring field.

The test specimen, which was measured tactilely on a coordinate measuring machine, can be seen in Figure 20. The part is made of aluminum and has a large number of form elements to check the accuracy of the 3D scanner on various geometries. The tactile measured form elements are illustrated in Figure 20.

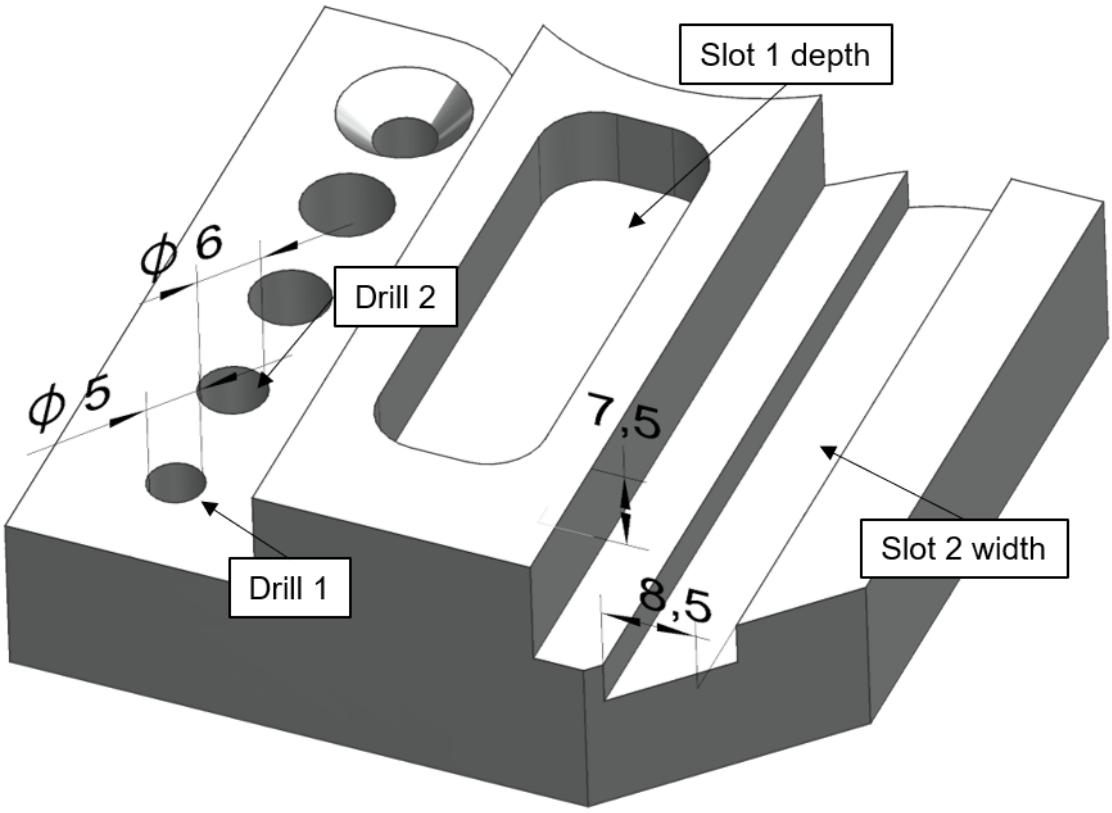

Figure 21 Aluminum test specimen. The dimensions shown correspond to the nominal values of the CAD file.

The tactile measured dimensions of the body are listed in Table 4. For the course of this work, the measured values are set as nominal values for determining the accuracy of the 3D scanner. The width of the through groove (groove 2) was not used in the course of this work because the first tests quickly showed that for an evaluation of this groove, the component must be captured from different component positions, and this was not possible under space conditions

Table 4 Tactile measured values of the form elements displayed in Figure 20.

Parameter	target value in mm	actual value in mm
drill 1 diameter	5	5,003
drill 2 diameter	6	6,015
slot 1 depth	7.5	7.627
slot 2 width	8.5	8.623

The results of the standardized test objects were validated using the aluminum test specimen. The influence of the glass pane installed in the vacuum chamber was tested using this body. Furthermore, the linear thermal expansion under space conditions was evaluated. For the 500-measuring field, these results were also checked on this component.

In the last step of the work, the knowledge gained up to this point was applied to satellite components. The measured components are demonstrated in Figure 21.

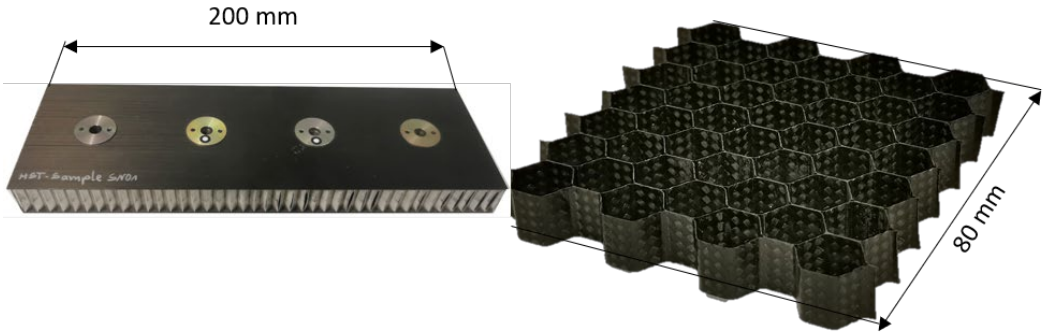

Figure 22 Measured satellite components. L. Composite component made of carbon fiber plates and aluminum. R. Honeycomb structure made of carbon fiber material.

The components are manufactured by Invent GmbH and provided for this work. For the composite component, the distance between the aluminum rivets as well as the expansion of the thickness through the aluminum fins shall be evaluated for atmospheric conditions and space conditions. Due to the use of very different materials with respect to the expansion coefficient, it can be assumed that the expansion of the rivets as well as the fins is prevented to an unknown extent by the carbon fiber material

For the CFRP honeycomb mesh, the expansions in all spatial directions under space conditions are of interest. Since the carbon fibers have different directions, the expansion behavior of the material is not fully known, so that an investigation of this can provide new data. New evaluation methods had to be used for these components, which had to be tested first. Subsequently, the measurement of the linear thermal expansions under space conditions was carried out.

4.3 3D-Scan

The theory and general procedure of 3D scanning have already been explained in a previous chapter. This chapter describes the tests performed to determine the general accuracy of the scanner. The tests performed were initially using the 100-measuring field. After the complete series of tests were completed, the results were also verified using the 500-measuring field.

The literature presented in Chapter 2 shows that a detailed investigation of the influence of the adjustable factors for 3D scanning has only been carried out selectively for strip light scanners or has been carried out for other scanning methods. For this reason, a conservative experimental design was used to conduct a thorough analysis, the goal of which was to develop parameters that would achieve the best possible results. A DoE was used to validate and optimize these results. Figure 22 describes the parameters studied.

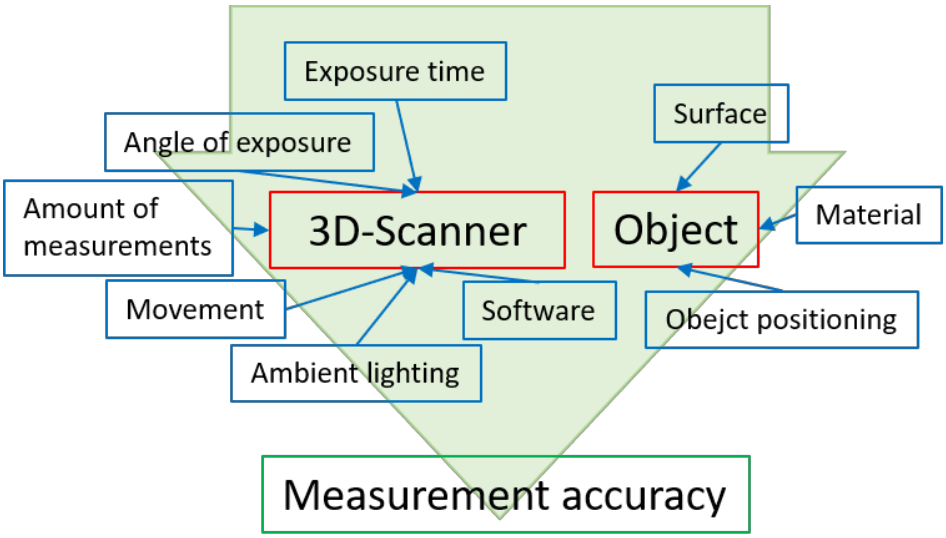

Figure 23 Investigated parameters for the development of best practice parameters.

Figure 22 displays the two systems, 3D scanner, and object, which together have an influence on the measurement accuracy. The division into two systems is necessary because the 3D scanner cannot directly influence the parameters of the object. This is particularly important for the DoE since only the factors of one system can be checked, in this case, those of the 3D scanner. The factors have shown also describe only those parameters which can be set by the user and which have been checked. The factors exposure time, exposure angle, motion, software, and ambient exposure were examined on the 40 mm gauge block. Software refers to possible optimization algorithms of the scanning software. The parameter motion describes whether the scanner is moved between two single scans or whether the part is moved. The factors number of individual measurements and object positioning were analyzed on the aluminum test specimen. The component position could not be checked for the gauge block since a meaningful evaluation from other positions was not possible.

In addition to the actual scanner, the 3D scanning system also consists of software, in this case, Collin3D from the company Zeiss in version 5, an automatic rotary table that can be controlled via the software and a mounting stand. Through Collin3D, the user can control the exposure time, the angle of exposure, the number of scans and possible optimization algorithms. The optimization algorithms improve the result of the individual stitching processes and reduce the gap between the individual object points. Measurement mark detection can also be activated via the scanning software. The measurement mark detection option was used for all experiments in this work. The position of the scanner can be changed via the scanner's tripod. The tripod itself can move the scanner in height, and the scanner can be rotated in three rotational degrees of freedom via the tripod's built-in swivel head.

For the best practice parameters, the parameters exposure time, exposure angle, movement, software, and ambient lighting were analyzed for their influence on the measurement accuracy of the 3D scanner. This analysis followed a conservative

experimental design in which only one factor was changed and the remaining factors remained constant.

For the DoE performed, the factors of exposure time, shooting angle, ambient exposure, and software were each examined with two levels. For the evaluation, a full factor plan with 16 trials was used so that effects and interactions can be clearly determined. The investigated parameters and their examined levels are listed in Table 5.

Table 5 Representation of the factors used and their levels for the DoE.

Factor	Levels	
Exposure time in ms	650	1000
Angle of exposure in °	35	45
Ambient lighting	On	Off
Software	Yes	No

The experimental setup for the conservative determination of the best practice parameters and for the DoE is described in chapter 4.6.1. The full factor plan of the DoE used is also presented there.

In addition to the best-practice parameters, the influence of the glass pane on the accuracy of the 3D scanner was investigated. The experimental setup used for this purpose is explained in chapter 4.6.2. The effect of the glass pane is checked using several adjustable parameters. These include the distance of the glass pane from the scanner, the angle of the glass pane, and the number of scans. It is expected that the angle of the glass pane exerts the greatest influence, and a systematic deviation from the nominal value can be detected. The influence of the glass pane is checked in detail using the test sphere and the 40 mm gauge block. These results are checked against all other bodies used. It should be said at this point that a glass pane was used for the initial detailed tests, which could not be used further in the later course of the work; more details follow in subchapter 4.6.2. For this reason, the verification of the initial results is carried out for all components.

4.4 Evaluation methods

The InspectPlus software from the Zeiss company was used to evaluate the 3D measurements. The program allows complete nominal/actual comparisons between the scanned 3D point clouds and CAD models, as well as the analysis of the geometric dimensions of the 3D point clouds. The supported formats are STL. IGES or STP.

For the gauge block, the evaluation of the distance between the parallel surfaces was performed. For this purpose, a plane was created using a best-fit algorithm of the software, based on a lasso selection of the respective parallel surfaces. The distance between the centers of the planes was then measured and evaluated within the program. This was done five times for each generated point cloud of the gauge block. The mean value of these five measurements was then used for the respective evaluation. Figure 23 shows the method using a point cloud of the 40 mm gauge block for a pair of planes.

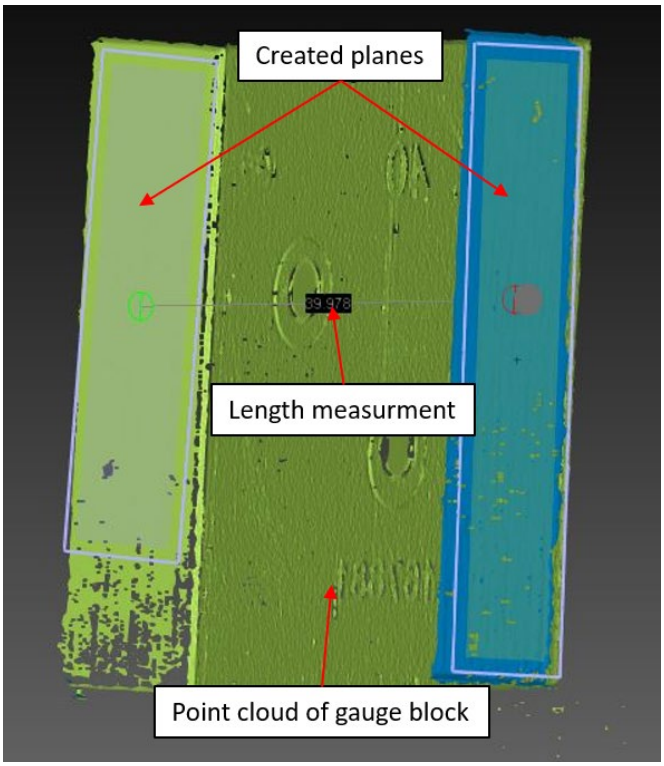

Figure 24 Representation of the evaluation method for the 40 mm gauge block

In the first step, the repeatability of this evaluation procedure was checked. For this purpose, the distance measurement was carried out 50 times in a randomly selected point cloud of the gauge block. The standard deviation of the method should be below 1 µm.

Using the 40 mm gauge block, another evaluation method was investigated. In this method, the distance between two measuring marks serves as the base length so that linear thermal expansion can be checked for components without significant form elements. To determine the length between the measuring marks, their scanned position is exported as spatial coordinates. Subsequently, a vector can be drawn between these points, the length of which is determined by InspectPlus. The principle is illustrated in Figure 24.

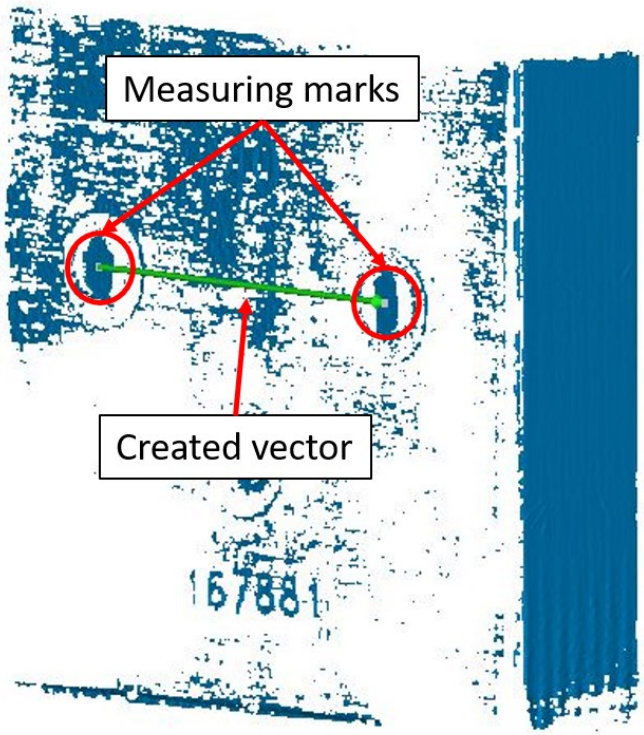

Figure 25 Illustration of the vector evaluation method

The evaluation for the form elements of the aluminum body follows the same principle as shown in Figure 23. For the depth of the pocket, five levels each were generated on the upper and lower surface of the pocket, and the average value was then calculated. For the holes, best-fit cylinders can be generated within the software based on the hole shell surface. This was also performed five times with subsequent averaging. The principle of the evaluation is presented in Figure 25.

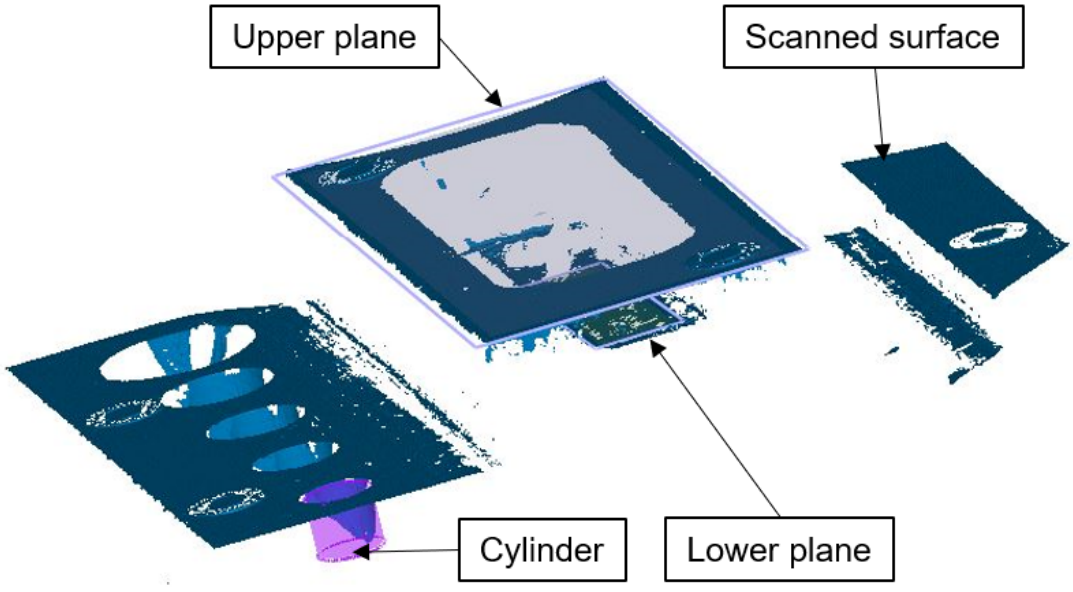

Figure 26 Illustration of the evaluation method for the aluminum body

For the composite part shown in Figure 21, the distance between two rivets was measured. For this purpose, the centers of the rivets had to be determined first. For this purpose, circles can be generated in InspectPlus on the basis of a selection with the help of another best-fit algorithm. Thus, five circles were generated for each rivet and the distance measured between their center points. The principle is illustrated in Figure 26.

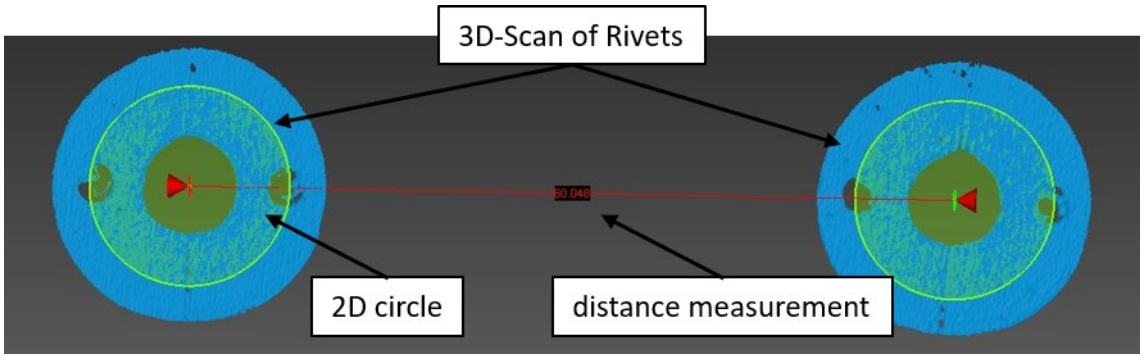

Figure 27 Evaluation of the rivet distance for the satellite part in InspectPlus.

For the CFRP honeycomb structure shown in Figure 21, the "inner diameter" of a honeycomb is measured. For this purpose, five planes are created on each of two opposite honeycomb surfaces, and the distance is measured. The principle is thus like the evaluation for the 40 mm gauge block.

4.5 Vacuum Chamber

In this subchapter, the construction and reconstruction of the utilized vacuum chamber is described. The vacuum chamber forms an important part of the work, since this represents the environmental conditions for the measurements under space conditions. For review, the requirements described at the beginning of this thesis are listed here again.

1. the inside of the vacuum chamber must have a space-like atmosphere
2. the components must be able to be heated. Thereby temperatures of at least 120°C should be reached
3. the components must be able to be cooled. Cooling with liquid nitrogen is desirable but not mandatory.
4. the vacuum chamber must have at least one sight glass so that the components can be measured from the outside.

The fourth requirement results from the fact that the scanner is not placed inside the chamber, which is also described in chapter 1.3. By completing the vacuum chamber, a functional laboratory scale is obtained. This differs from industrial plants especially in the general size, the achieved vacuums, and achieved temperatures inside the chamber. The advantages of the laboratory scale are that the experiments can be carried out much faster since, in large chambers, the evacuation of the air takes much longer and is more expensive. This is due to the vacuum pumps used, some of which

use liquid nitrogen to generate the vacuum. The following sections explain step by step how the respective requirements are met.

4.5.1 General layout

Figure 14 indicates that space conditions begin at a pressure of 10^{-5} hPa or mbar. Guidelines such as [QB5-15] also indicate that a vacuum of at least 10^{-5} mbar must be present for the vacuum tests of the cubsats [QB5-15, p.38]. A turbopump is connected to the vacuum chamber used, which can achieve the required vacuum. Thus, the first requirement is fulfilled.

For the fourth requirement, two sight glasses were installed on the chamber. The sight glasses have different diameters. The large sight glass has a diameter of approx. 150 mm (sight glass 1) and the small glass of 100 mm (sight glass 2). Apart from the diameter, both glasses are identical in construction. The glasses are flat and do not show any strong curvatures except towards the flange where a thickening occurs, which also leads to distortions in the scans. The 100 mm sight glass is shown in Figure 27.

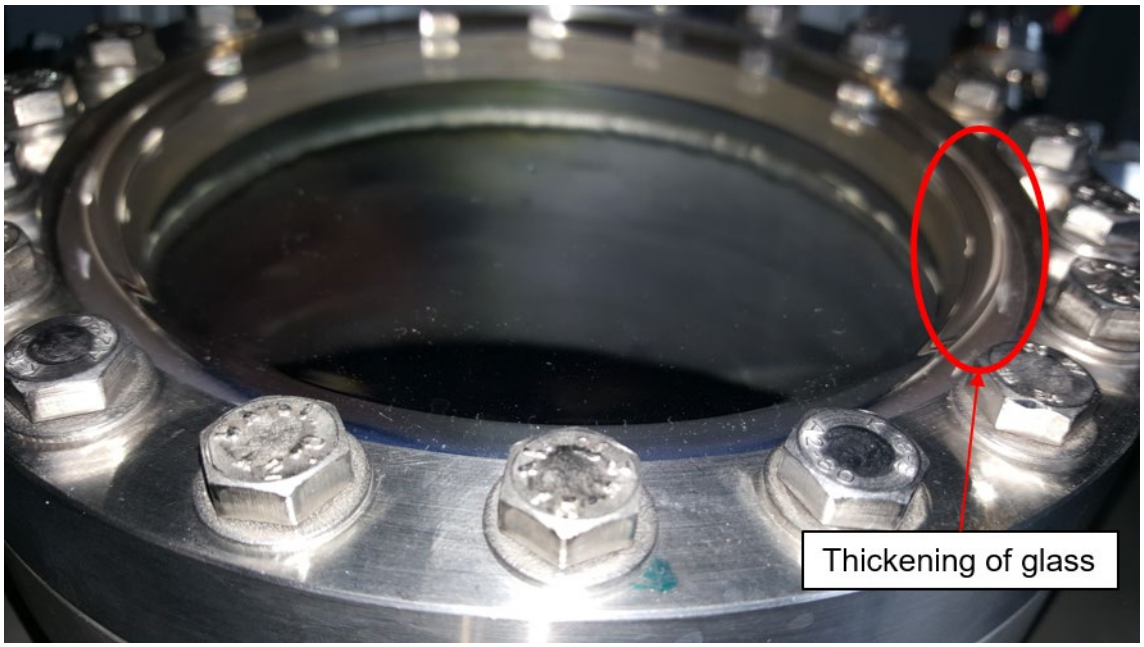

Figure 28 Illustration of the glass thickening on the basis of the 100 DN glass.

The rest of the requirement results in some additional logical requirements, which will also be briefly described below.

a. The chamber must have an internal heating and cooling source.
b. It must be possible to measure temperatures inside the chamber.
c. A support surface for the scan objects is required inside the chamber, which is adjustable in height if possible.

The temperature of the experiments from [QB5-15] is 50°C [QB5-15, p.38], which is well below the target temperature of 120°C. Data for cold or temperatures below 0°C

are not available in [QB5-15]. However, the cooling was not done with liquid nitrogen, as desired in the third requirement, because the handling of this liquid is associated with some difficulties. A continuous and controlled cycle of liquid nitrogen requires special pumps as well as internals for the vacuum chamber, which could not be used due to high costs. It is possible to let the liquid nitrogen flow into the cooling block unregulated through a special feed-through. The feedthrough basically consists of an open cup, a fluid inlet and outlet, which lead to the vacuum chamber. The feedthrough uses gravity to distribute the fluid in the refrigeration block, which requires installation on the upper connecting flanges of the chamber. However, this complicates the repeatability of the experiments, since the necessary amount of nitrogen can only be estimated and the amount has to be adjusted according to the temperature. Instead, cooling was done with the help of a Peltier element.

Heating of the component and cooling of the component is done by two different experimental setups, which cannot be installed in the chamber at the same time due to lack of sufficient space. The reason for the division is the use of the Peltier element since it must be cooled continuously with cold water to reach the lowest possible temperatures. The description of the two setups follows in the next two subchapters.

Basically, it can already be stated here that the requirements for the environmental conditions of the evaluation procedure are met. With the available laboratory scale, components can be measured that have a volume of approximately 150 x 150 x 150 mm. This makes the laboratory scale particularly suitable for components of the Cubesat satellite class, since these fit completely into the vacuum chamber with their standardized size of 100 x 100 x 110 mm per unit [NAS-17, p. 4].

4.5.2 Test setup for warm temperatures

Since heat in a vacuum can only be transferred by direct contact or radiation, a radiant heater with a heating power of 1 kW was installed inside the chamber. Figure 28 demonstrates the setup used inside the chamber.

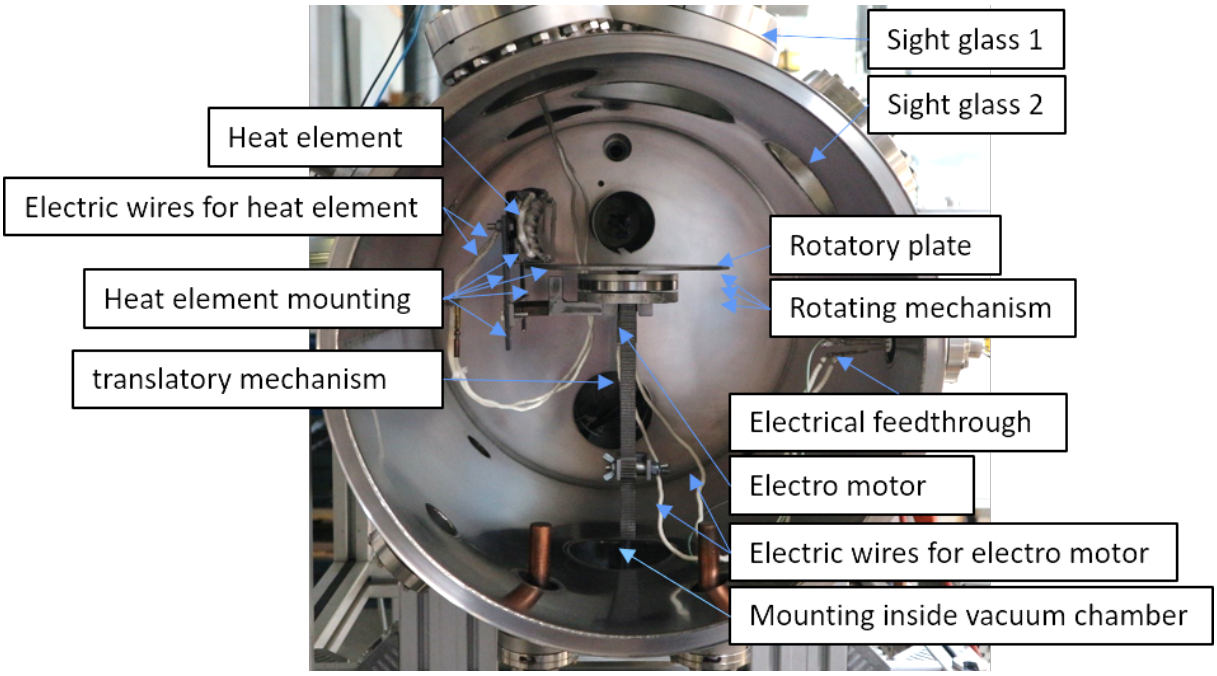

Figure 29 Experimental setup for hot temperatures inside the vacuum chamber

The shown rotating mechanism is a part of a developed rotating disk, which will be explained in a separate chapter. With the help of this setup, it is possible to generate temperatures of up to 150°C inside the chamber. This corresponds to a 45% output of the heating element. The element is controlled by a rotary transformer, which is safely located outside the chamber. The rotating plate allows the component to be positioned inside the chamber and scanned through the two built-in sight glasses. The electrical feed-through also makes it possible to connect thermocouples, which can be used to measure temperatures at specific points. In the course of the work, temperature measurements were carried out throughout the chamber. The description of these tests is given in Chapter 4.6.4. The test setup shown in Figure 28 allows all requirements to be met except for the cooling requirement, which means that the environmental conditions for the measurement procedure have been successfully established.

4.5.3 Test setup for cold temperatures

In order to use the Peltier element for cooling, direct surface contact must be made with the component, as the radiant energy of the Peltier element is not sufficient for cooling. To create a better transition, a special thermal paste was used between the component and the element. The experimental setup for the cold temperatures can be seen in Figure 29.

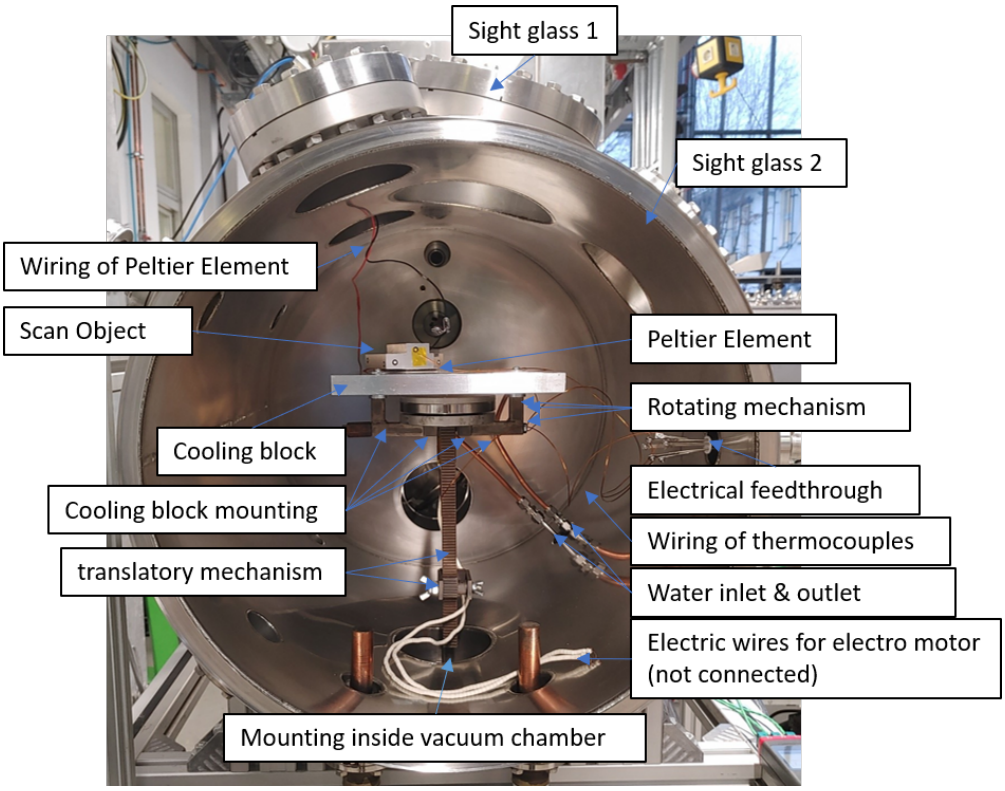

Figure 30 Experimental setup for cold temperatures always inside the vacuum chamber

The cooling block is made of aluminum and is constantly flushed with ice water during the cooling tests with the aid of a small water pump. This ensures the lowest possible temperatures for the Peltier element. The mechanism of the turntable is also installed here, but is not functional due to the cooling block. Temperature measurements were also carried out for the cooling tests. With the help of this setup, all requirements except for the heating requirements are fulfilled so that the environmental conditions for the measurement procedure were also successfully established for the cold temperatures.

4.5.4 Electric rotary table

One of the great advantages of 3D scanning is that objects can be completely mapped, and a three-dimensional surface comparison or evaluation can be created. To do this, however, the object must be scanned from several views, which is not directly achievable inside the vacuum chamber. For this reason, an electrical rotary table was manufactured and installed, which makes it possible to rotate the component. As already described, this is only available within the framework of the heating experiments. The most important components of the rotation mechanism will be briefly shown and described below. The complete setup in an exploded view is shown in Figure 30. This setup corresponds to the setup shown in Figure 28.

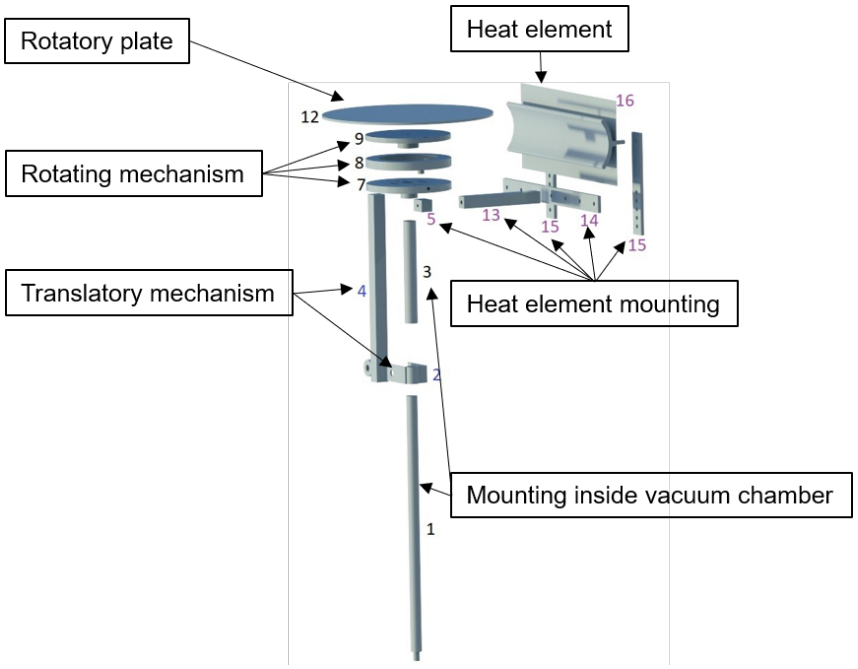

Figure 31 Exploded view of the experimental setup for hot temperatures.

The installed components are almost all made of metal or heat-resistant plastics such as Teflon. Components 1 and 3 from Figure 30 are the foundation of the complete setup. Part No. 1 is directly built into the vacuum chamber. A translatory mechanism for the rotatory table is achieved by component No. 2 and No. 4. The heater (Part No. 16) sits on the heat element mounting parts, which are No. 5 and No. 13 – 15. The rotatory plate (No. 12) is on top of the rotating mechanism, which Figure 31 demonstrates in detail. The rotation of the components is solved by an electrically driven turntable. The degreased electric motor is installed directly in the vacuum chamber. By degreasing the motor, no contamination can occur due to chemical reactions of the lubricants inside the vacuum chamber. The core of the manipulator is the rotary mechanism from Figure 31.

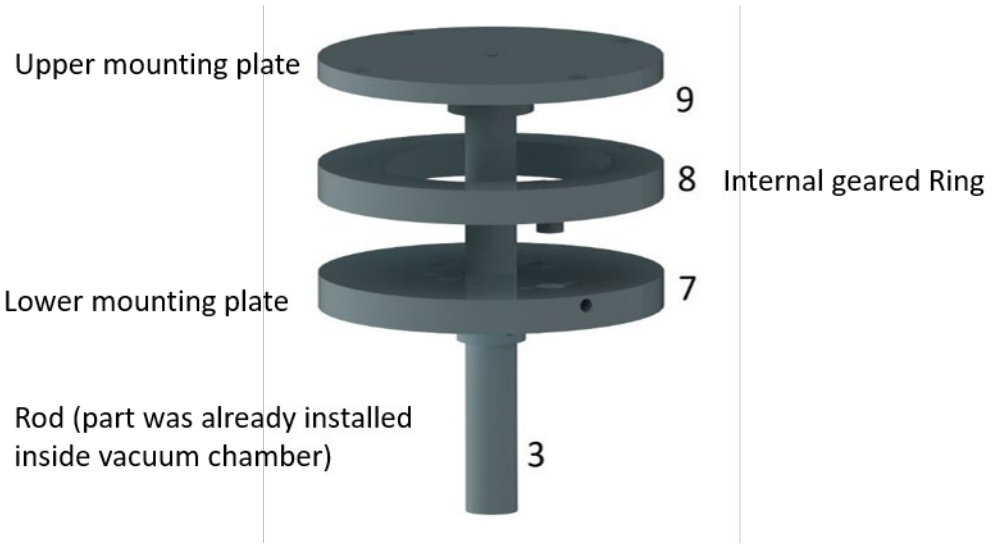

Figure 32 Centerpiece of the rotary manipulator.

The lower plate (No. 7) is firmly screwed to the cylinder (No. 3). This cylinder was already installed in the vacuum chamber at the beginning of the project and was ideally suited as a mounting for the entire turntable. The electric motor (not shown) is attached to the underside of this plate. The electric motor drives the gear of the internal ring gear (No. 8). The internal ring gear is bolted to the upper plate (No. 9) so that both the upper plate and the ring gear rotate. To ensure that the rotation is as frictionless as possible, a Teflon washer is placed between the upper and lower plates; this is not shown in Figure 31.

With the aid of the rotation manipulator, the results for the influence of the glass plate can be checked in relation to the number of scans. This check is carried out on the aluminum test specimen since the parallel surfaces of the gauge block could not be measured meaningfully by the sight glasses.

4.6 Test setups

In this subchapter, all experimental setups used in the course of this work will be demonstrated. The setups describe the position and orientation of the scanner and the component in relation to each other. For the experimental setups inside the vacuum chamber, please refer to the corresponding chapters that have already been described. It is important to note that the description of the experimental setups does not follow the chronological order of the project but is organized by category. It is started with the description of all experimental setups that were carried out under atmospheric conditions and without a glass pane. Then the experiments with glass pane under atmospheric conditions are explained. Finally, the experimental setups under space conditions follow, as well as the description of the temperature measurements. Furthermore, scans under space conditions always include a scan through a sight glass.

4.6.1 Scans under atmospheric conditions and without glass pane

For the determination of the best-practice parameters, the simple experimental setup shown in Figure 32 was used.

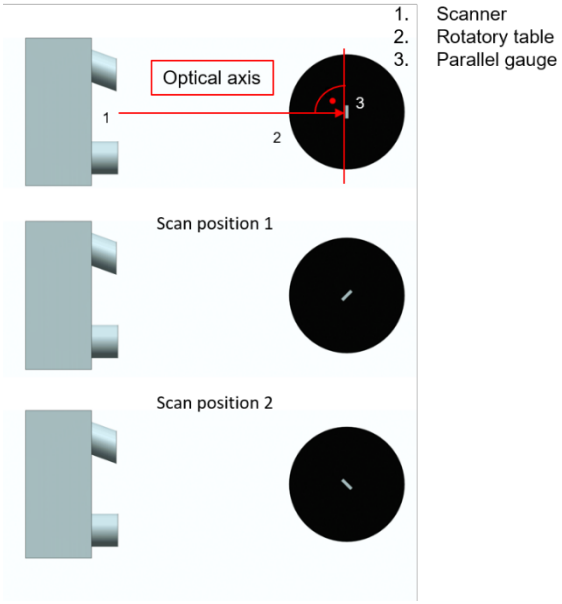

Figure 33 Schematic representation of the experimental setup used to determine the best-practice parameters

The position of the scanner is selected in such a way that the optical axis of the scanner is perpendicular to the 40 mm gauge block. For this purpose, the orientation of the angular positions of the scanner's swivel head is 0° ±2° in all directions. The height of the tripod is at the minimum level. For the conservative experimental design, the parameters were examined in the order given in Figure 33.

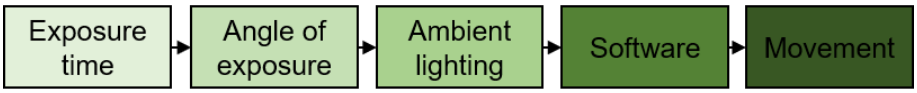

Figure 34 Order of the conservative experimental design for the best practice parameters.

The angle of exposure was set via the rotary table. For the motion parameter, the scanner was moved instead of rotating the part. The repeatability of this examination is lower than the rotation by means of the rotary table. For each parameter, 20 measurements were taken. Each measurement captures the 40 mm gauge block from two views. The evaluation is performed according to the principle described in chapter 4.4. The aim of the tests was to find parameters with which a deviation of less than 20 µm from the nominal value is possible for a worst-case component. The test setup from Figure 33 was also used for the DoE. The test plan used can be seen in Figure 34.

No.	Exposure time	Angle of exposure	Ambient lighting	Optimization/ Software
1	1000	35	Off	On
2	500	45	Off	Off
3	500	35	Off	On
4	500	45	Off	On
5	500	35	On	On
6	500	45	On	Off
7	500	35	On	Off
8	1000	35	Off	Off
9	1000	45	On	On
10	1000	35	On	On
11	1000	35	On	Off
12	500	45	On	On
13	1000	45	On	Off
14	500	35	Off	Off
15	1000	45	Off	On
16	1000	45	Off	Off

Figure 35 DoE experimental design for the best practice parameters

For each test, 5 measurements of the 40 mm gauge block were made from two views each. For the evaluation of the DoE, the mean value of the 5 measurements for the respective test was used.

The best practice parameters were tested using the aluminum specimen. Here it was shown that the exposure time is not the same across the board for each metallic object. At 250 ms, the exposure time for the aluminum test specimen is significantly lower than the settings tested previously. However, a new evaluation was not performed with regard to this parameter. The aluminum body was used to check the remaining results. The test setup from Figure 35 was used to check the results of the best practice parameters. For each measurement, the part was scanned from three views (0°, 35°, 325°). The results were checked against the 5 mm hole and the depth of the pocket using 50 measurements.

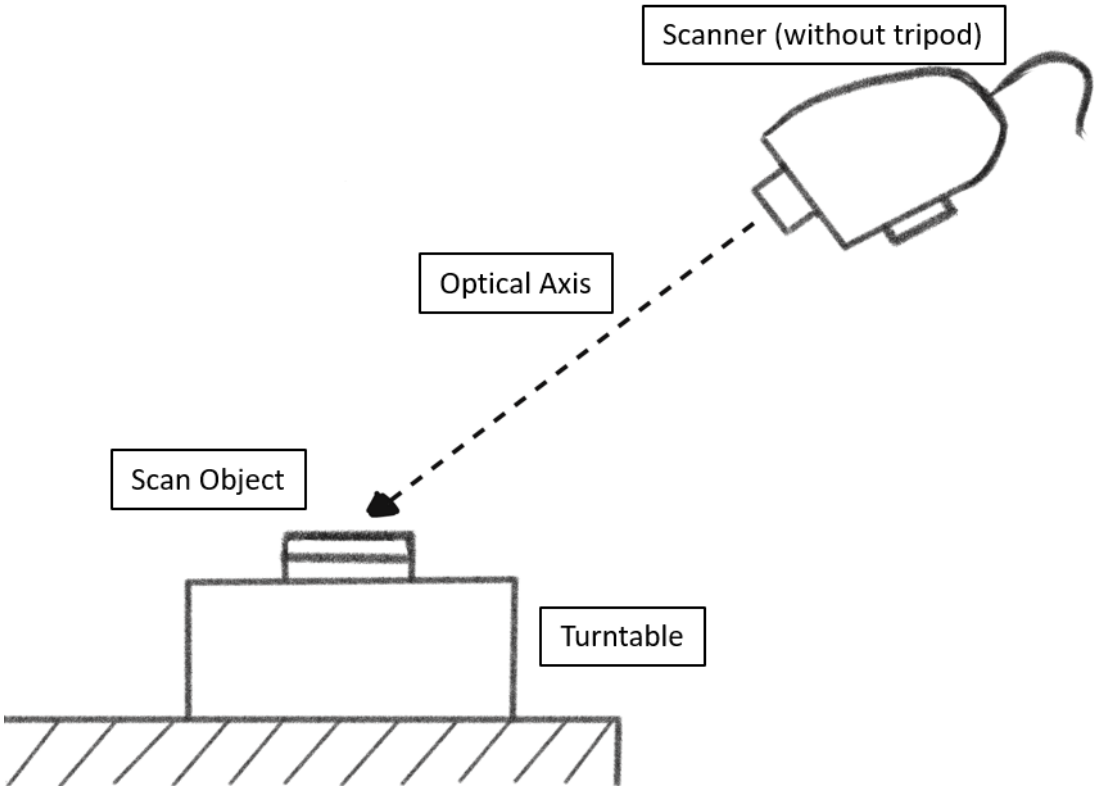

Figure 36 Sketch for the test setup for checking the best practice parameters using the aluminum test specimen

The position of the scanner used in Figure 35 is different from the position used for the 40 mm gauge block, so this factor was changed as well as the exposure time. For this reason, the influence of the component position on the accuracy was checked. This was done with the same test setup as depicted in Figure 35.

For this purpose, the aluminum test specimen was measured from two additional positions, which can be seen in Figure 36. Apart from the component positions, it was also tested to what extent a measurement from several views differs in terms of accuracy from a measurement from a single view. For each position, 25 measurements were generated from a single view. The exposure times varied slightly between the individual positions.

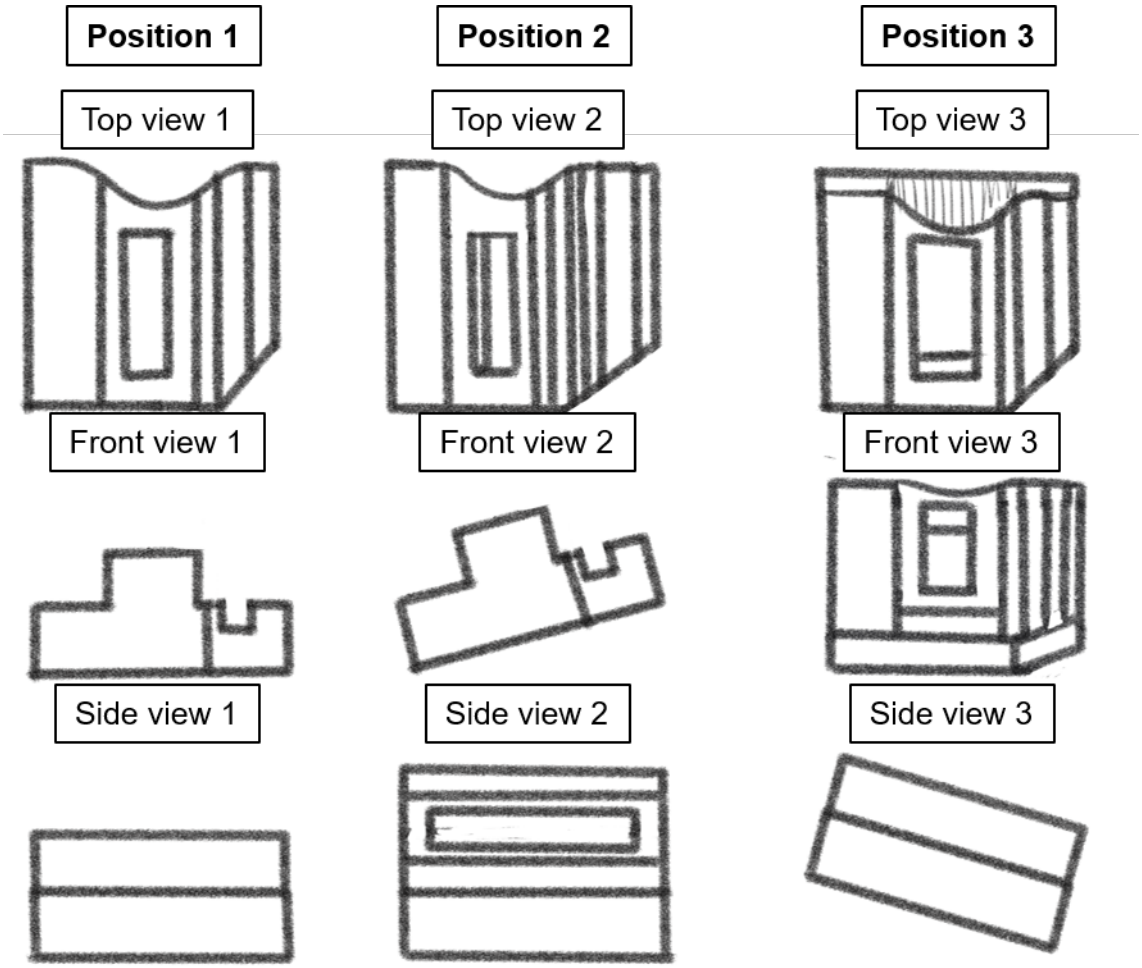

Figure 37 Sketches of the used component positions for the aluminum test specimen.

The last experimental setup to be described is the setup for the linear thermal expansion measurements under atmospheric conditions. For this purpose, the heater installed in the vacuum chamber and the 40 mm gauge block were used. The gauge block was positioned in proximity in front of the heating element and measured from two views. In this case, the component was not rotated, but the scanner was moved. The heating element is connected to the transformer, as in the vacuum chamber. For these tests, 100% of the heating power was used. Figure 37 shows the test setup used.

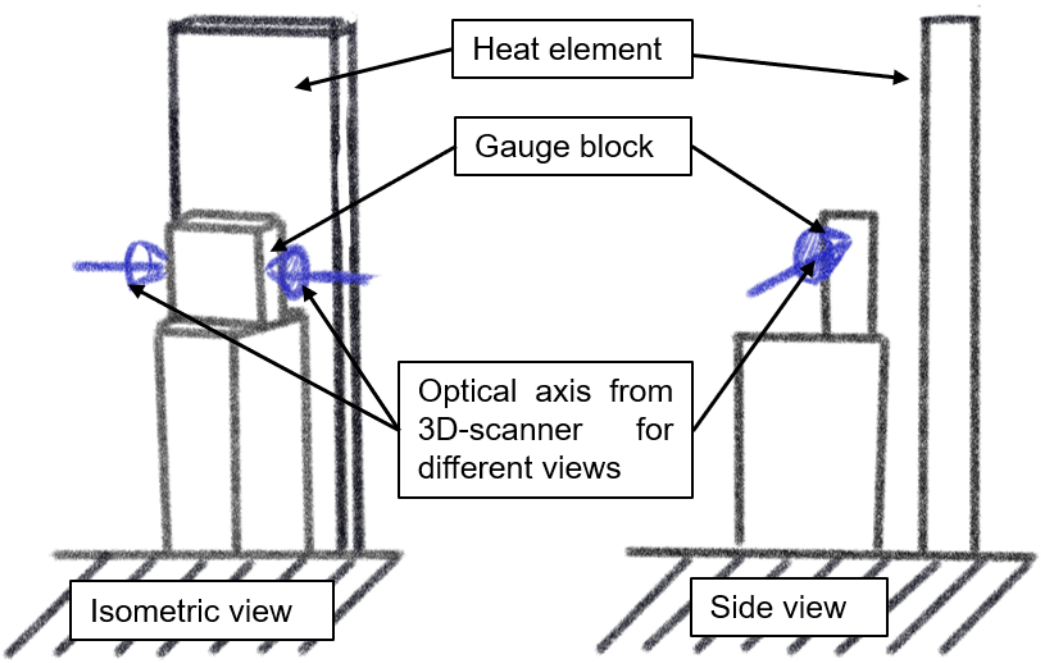

Figure 38 Sketch of the Experimental setup for the measurement of linear thermal expansions under atmospheric conditions.

The temperatures of the component were measured using two type K thermocouples. The thermocouples were measured on the front and back of the component. The component has a distance of approx. 2 cm to the heating element. For the evaluation, measurements were made at room temperature and warm temperature. For each temperature, 20 measurements were made, each consisting of two views. The coefficient of expansion α for the gauge block is $11.5 * 10^{-6} \frac{1}{K}$ [Pre-17]. For the evaluation, the vector method, and the conventional method were also compared.

Thus, all major experimental setups have been described. The satellite components have also been measured under atmospheric conditions. However, these setups do not differ from the configuration used in Figure 35, except that the angle and height setting of the scanner is different. For this reason, an explicit presentation of these setups is omitted here.

To check the evaluation procedures for the satellite parts, a series of measurements were carried out under atmospheric conditions. For this purpose, two measurement series each were generated from different component positions. Each measurement series consisted of 20 measurements. These tests were also used to validate the general accuracy of the scanner and to determine whether it is also possible to achieve the accuracy limit observed up to this point for these components. For the evaluation of the linear thermal expansion, 10 measurements were taken at room temperature and 10 measurements at hot temperatures.

4.6.2 Scans through glass

To determine the influence of the glass pane on the measurement accuracy, a glass pane was added to the test setup from Figure 32. Figure 38 schematically demonstrates the extended test setup.

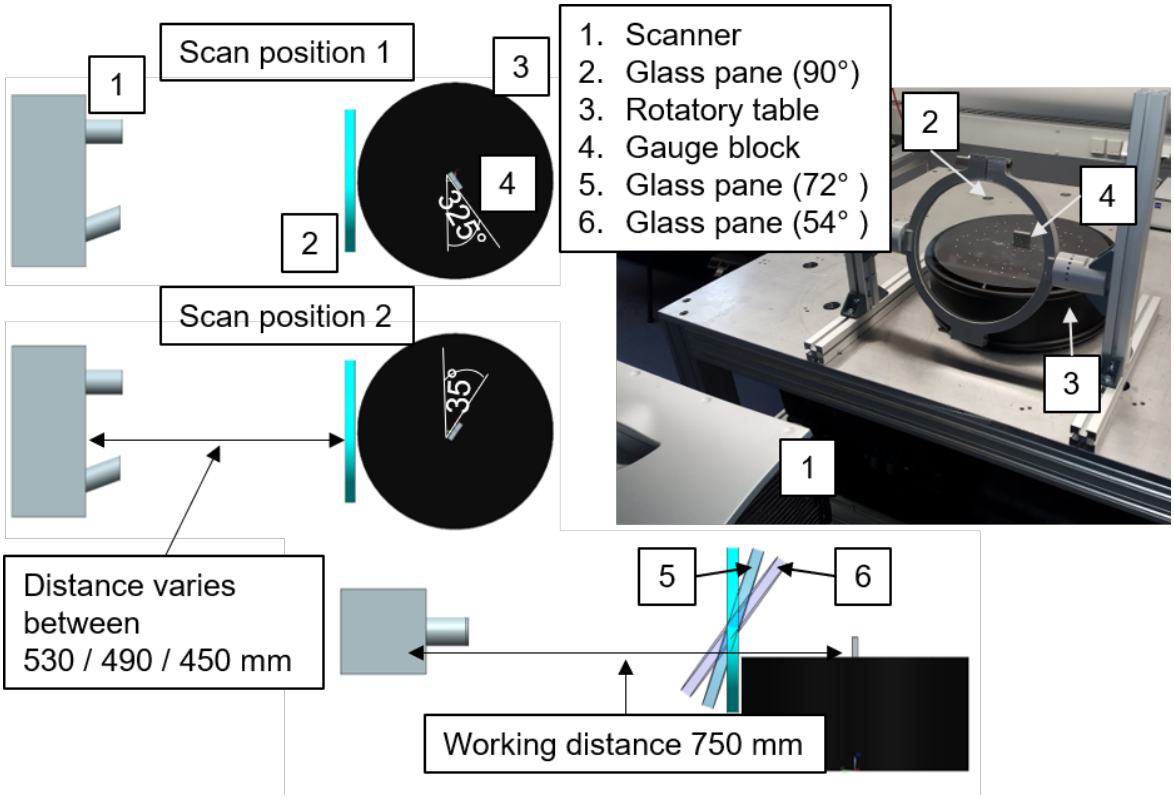

Figure 39 Experimental setup to determine the influence of the glass pane on the measurement accuracy.

The glass used is a 20 mm thick borosilicate glass pane with a diameter of 290 mm and a refractive index of 1.473 [Dor-21, p.5]. As already briefly described in chapter 4.3, this glass pane was a loan; thus, not installed in the vacuum chamber. The pane is flat and does not show any noticeable curvatures or thickenings. For this reason, it was assumed that the glass pane is a plane-parallel pane. This assumption is also used later in the ray tracing approach.

The pane was positioned between the scanner and the gauge block. The distance of the center of the glass pane to the scanner varied between the lengths 450/490/530 mm ± 1 mm during the measurement series. A fixture was used to change the angle of the glass pane during the series of measurements. The angles 90°, 80°, 72°, 60°, and 54° ± 1° were checked. The distance between scanner and gauge block was 750 mm over all tests. The scanner was positioned so that the optical axis of the camera was perpendicular to the surface of the gauge block.

For initial tests, only the angles 90°, 72°, and 54° were checked at all distances. For each distance and angle combination, 20 measurements were made, each consisting of two views. The angles of the views are noted in Figure 38. The exposure time was 650 ms, and the ambient lighting was on and the laboratory was darkened.

Subsequently, another experimental run was performed with all angle and distance variations. The 3D scanner settings remained the same, and 10 3D measurements were generated for each combination. This served to validate the previously obtained results. In addition to these measurements, the measurement sphere from Figure 19 was also measured through the glass pane. Using the experimental setup from Figure 38, a random angle was set, and then the measuring sphere was scanned 20 times. Due to the matte surface of the sphere, the exposure time settings deviated from the best-practice parameters.

With the help of the measurement series of the gauge block, which was measured through the additional glass pane, the ray tracing approach is checked (see chapter 4.6.6). For this purpose, the measured measurement marks are exported as point coordinates. These point coordinates are imported into Siemens NX and used to reconstruct the rays. The theoretical ray tracing approach is used as a basis for this.

The glass pane used for these tests could not be installed in the vacuum chamber. The reason for this is the different connection systems within the vacuum technology. The connection system of the vacuum chamber is not compatible with the flange system of the glass pane, which is why the glass pane type from Figure 27 was used.

Due to the change of the glass pane, experiments were also carried out with the glass panes of the vacuum chamber. The corresponding experimental setup is shown in Figure 39.

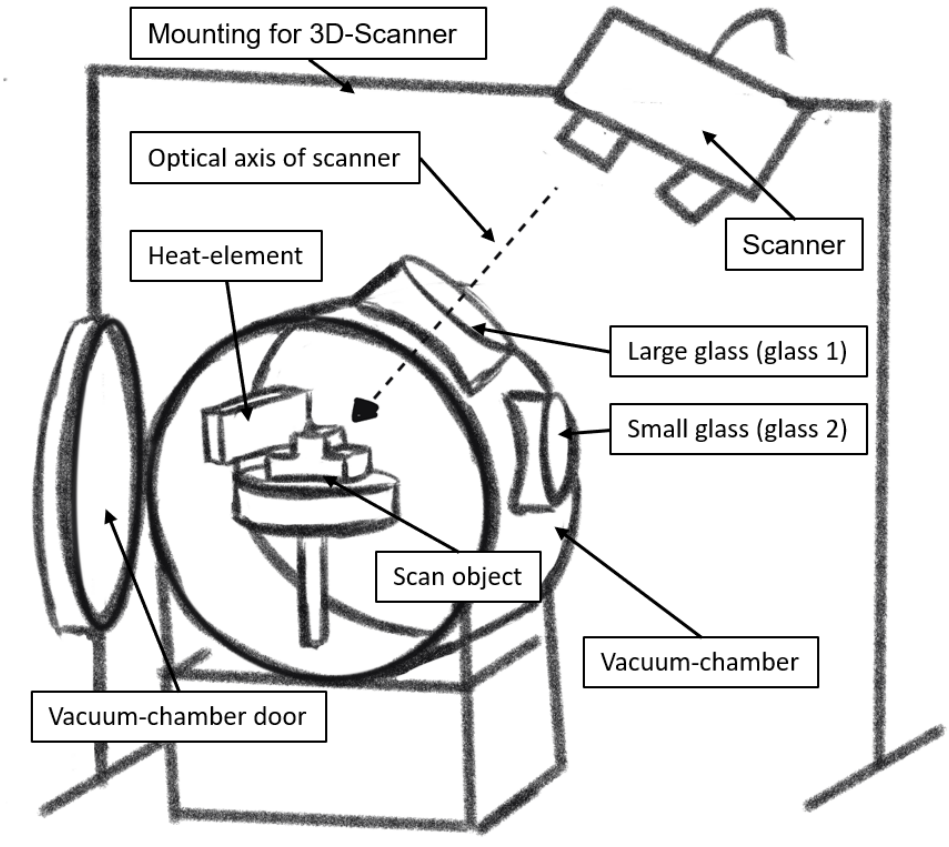

Figure 40 Sketch of the test setup for checking the influence of the installed sight glasses of the vacuum chamber, as well as for scanning under space conditions.

Figure 39 illustrates that for these experiments and for all experiments under space conditions, the scanner is mounted on a frame that was built specifically for this work. The frame allows the scanner to scan through the top of the glasses into the chamber, providing the largest possible measurement volume for surface acquisition. Linear guides allow both the height and horizontal position of the scanner to be changed. In addition, a swivel head is attached to the frame so that the three rotational degrees of freedom can also be used to adjust the scanner position.

Tests were performed for both sight glasses. For each sight glass, 25 measurements were taken, each consisting of a single view. In addition, 25 measurements were also taken through the large sight glass using the rotation manipulator. For the evaluation, the depth of the pocket and the 6-mm hole of the aluminum specimen were examined.

4.6.3 Scans under space conditions

The scans under space conditions were performed using the vacuum chamber described earlier. The experiments were all aimed at measuring the linear thermal expansions of components. For this purpose, experiments were performed at room temperature, at hot and cold temperatures. Since the experimental setup is different for hot and cold temperatures, an additional series of measurements was performed for each temperature from an additional component position. This only applies to the test series at room temperature and warm conditions. Since the component was connected to the Peltier element, and this needs as much contact as possible with the cooling block, no further component position could be checked.

Basically, the measurement series used the test setups already shown in Figure 28 and Figure 29, as well as the frame described in Figure 39. During the tests, a vacuum of at least 10^{-5} mbar prevailed inside the chamber. The room temperature was 20°C, the temperature for the warm conditions was 125°C, and the cold temperatures were -33°C. The exposure times varied depending on the series of measurements. For each temperature and component position, 20 measurements were generated from one view each. These tests were performed on the aluminum test specimen. Furthermore, test series at room temperature and under warm conditions were generated on the composite part and the CFRP honeycomb structure.

For the linear thermal expansions, it is essential to know how warm or cold the component to be measured is. For this reason, the temperature was measured at one point on the component for each measurement. This point was usually on the opposite side of the radiant heater

In addition to the scans under space conditions on a laboratory scale, a series of experiments under space conditions on an industrial scale could be carried out. The corresponding test setup can be seen in Figure 40. In this setup, the scanner had to be placed directly against the two viewing glasses so that the object inside the chamber could be measured. The object to be measured is 30 mm gauge block, which is rotated about 35 °degrees to the optical axis of the scanner. The object was measured from

one view only because the evacuation of the vacuum chamber takes significantly longer than in the laboratory scale. For the experiments, the object was measured eight times each at a temperature of 135° C and -33 °C. The vacuum inside the chamber was 10^{-8} mbar. In terms of chronology, this series of measurements took place at a time when the laboratory-scale experimental setup was not yet fully operational. Since this series of measurements only consists of eight measurements each, it only serves as an indication and was therefore not included in the complete overview in Figure 18.

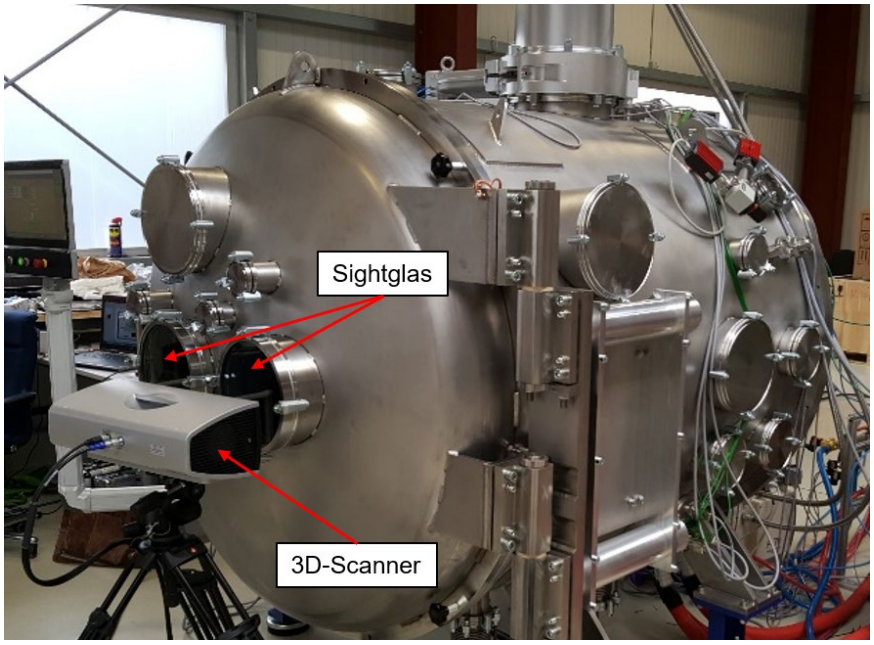

Figure 41 Experimental setup for measurements under space conditions on an industrial scale.

4.6.4 Temperature measurements in a vacuum

As already described, the temperature change in the vacuum can only occur via radiation or direct contact. Some components are installed in the vacuum chamber, such as copper seals, which can only withstand a certain temperature until a loss of function occurs. For this reason, the temperature inside the chamber must be known as accurately as possible. For this reason, extensive measurements were carried out.

These temperature measurements were carried out with thermocouples of type K. Thus, the measurement is carried out selectively on selected elements of the vacuum chamber and not completely. One possibility for full temperature measurement is a thermographic camera. However, these optical systems do not work through glass panes, as can be seen in Figure 41. For this reason, the thermographic camera would have to be installed inside the chamber. This leads to a few practical problems. First, a cable feed-through must be installed on the vacuum chamber for data transfer between the camera and the PC and for the power supply. Depending on the camera's connector, this can be a special design, which is cost-intensive. The more serious problem is the space inside the chamber.

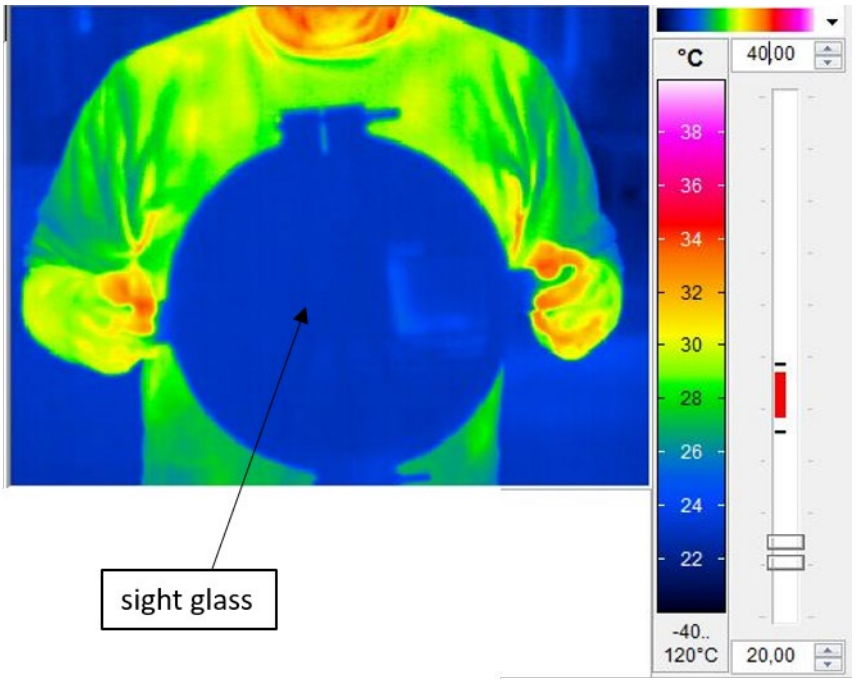

Figure 42 Thermography measurement of a person with glass pane in front of the body.

The dimensions of the chamber, including the installed heating system, are shown in Figure 42.

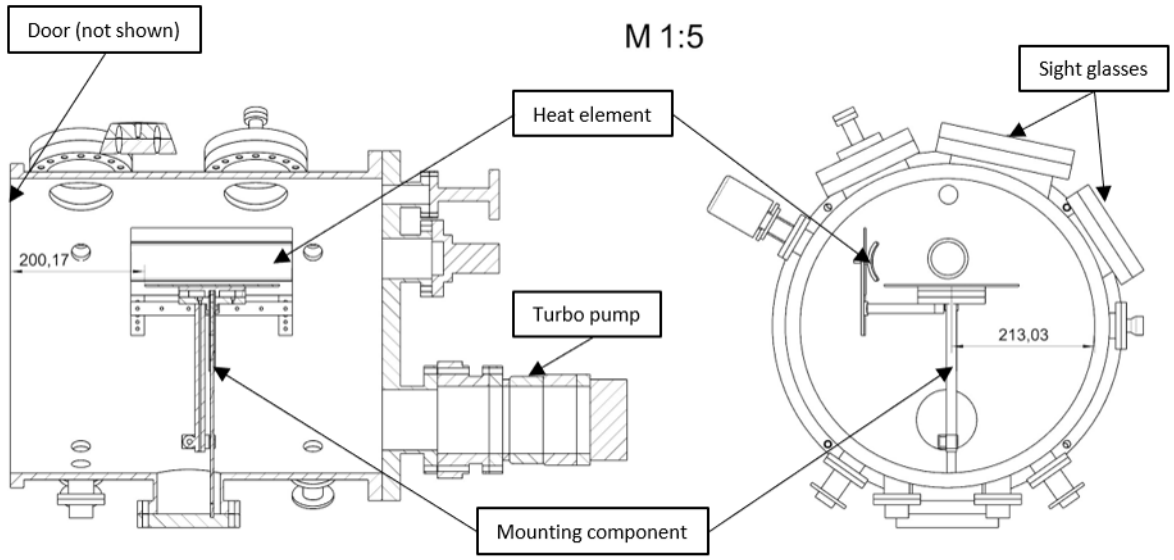

Figure 43 Technical drawing of the vacuum chamber with the heating setup installed. L: a sectional view of the chamber. R: a derived view of the chamber based on the sectional view

Figure 39 shows that there is not much space available for setting up the camera. In particular, the illustrated 200 mm; limit the camera, since this direction corresponds to the orientation of the optical axis of the camera, which must be taken approximately so that the turntable can be measured. Furthermore, the camera needs additional mounting, which might restrict the limited space even more. With the help of the thermography camera, some elements could not be measured since the components are not in the field of vision of the equipment. This includes, for example, the two glass

panes. In addition to these spatial problems, the environmental conditions for the camera itself are also critical. The high temperatures of the radiator in combination with the vacuum present leave open the question of whether the camera can function at all inside the chamber. For this reason, it was decided not to install a thermography camera inside the vacuum chamber since the necessary time and financial effort outweigh the possible benefits.

Since the temperature changes can only be recorded selectively via the thermocouples, a series of tests had to be carried out. The points checked can be seen in Figure 43. The following points were measured:

1. pirani probe
2. large sight glass (inside)
3. small sight glass (inside)
4. electric motor
5. inlet of the turbo pump
6. center of the turntable (top)
7. outside of the turntable (top)
8. center of the turntable (bottom))

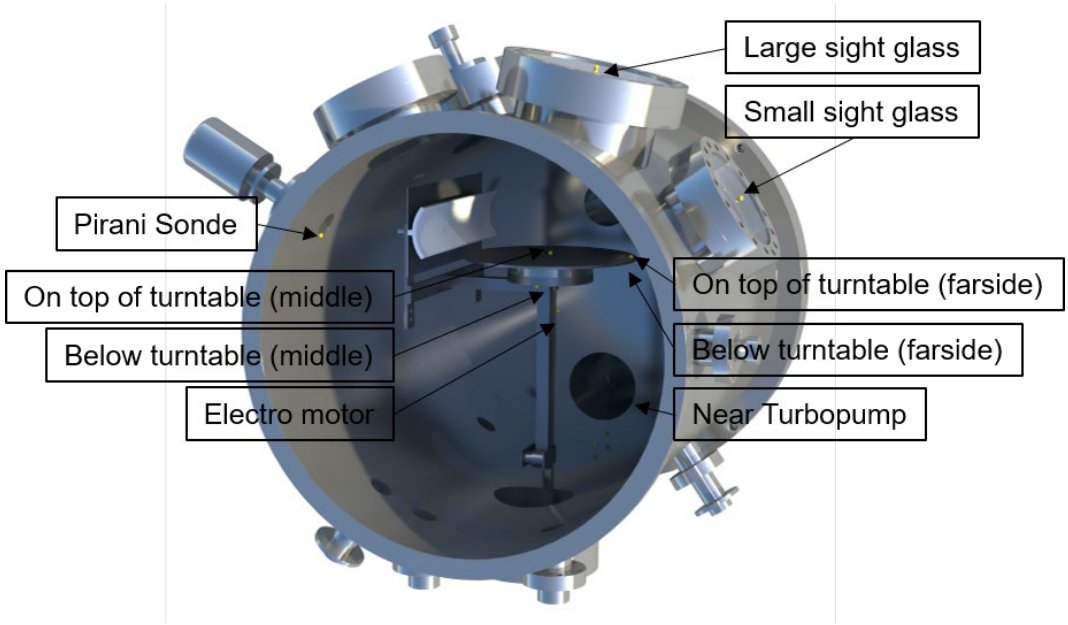

Figure 44 Representation of the checked locations for the temperature measurements at warm temperatures.

Three measurements were made for each point. Each measurement lasted 90 minutes, of which 30 minutes were used for heating. The remaining 60 minutes were used for cooling. The heater used 45% of its maximum power for these experiments. A vacuum of at least 10^{-5} mbar was maintained inside the chamber.

Similar tests were performed for the cold test setup. The points tested are demonstrated in Figure 44. The following points were tested for these temperature measurements.

1. component

2. cooling water inlet of the cooling block
3. cooling water outlet of the cooling block
4. large sight glass
5. small sight glass
6. pirani probe
7. turbo pump inlet
8. top of the cooling block next to the Peltier element
9. electric motor

These measurements lasted 40 minutes per test, of which the Peltier element was switched on for 15 minutes. Throughout the tests, the cooling block was flushed with water at a temperature of less than 4 °C. The vacuum was maintained at a constant level throughout the tests. During all the tests, a vacuum of at least 10^{-5} mbar was present inside the chamber. The shorter test times result from the type of energy transfer. The Peltier element cools the component by direct contact, which causes the temperature to change much faster than by radiation.

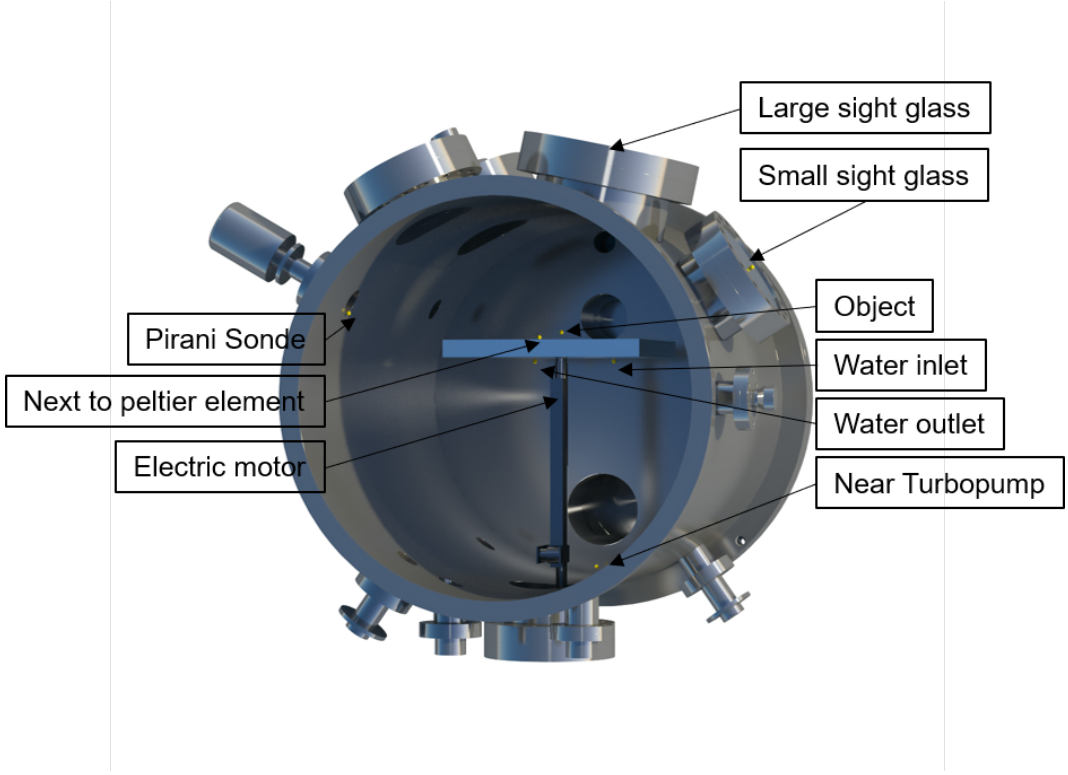

Figure 45 Representation of the checked locations for the temperature measurements at cold temperatures.

In addition to the components installed in the vacuum chamber, the temperature distribution over the component during the tests must be known. For this reason, temperature measurements were also carried out on the aluminum test specimen. For this purpose, two series of measurements were taken for the depth of the pocket and the 6 mm holes. Within the scope of these series of measurements, three measuring points were checked in each case, which are shown in Figure 45.

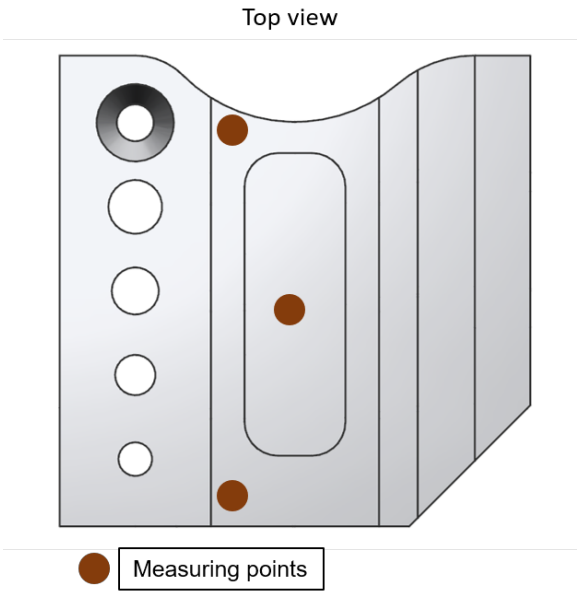

Figure 46 Representation of the measuring points for the temperature distribution over the aluminum test specimen

The time of these tests was not fixed, instead the part was heated until the rearmost of the three measuring points indicated a temperature of approx. 120 °C. Three measurements were carried out for each series of measurements.

Since these measurements can only be recorded selectively at the selected measuring points, the temperature values obtained are only indications to determine whether possible excessive temperatures can lead to potential defects in the vacuum chamber, such as leakage problems. For the examination on the component, the obtained measured values are also considered as a reference and are not to be equated with a complete temperature field examination on the entire component.

4.6.5 Validation measurements with the 500-measuring field

As already described at the beginning of the theory subchapter 3.1.4, it is possible to exchange the measuring volumes of the employed scanner. Most of the results presented in this work were obtained with the 100-measuring field. When using the 500-measuring field, the question arises to what extent the previously obtained results can be repeated. A 1 to 1 transfer of the results is excluded due to the different point distances of the measuring fields. For this reason, it is investigated to what extent the 500-measuring field performs in comparison to the 100-measuring field. The possible use of the 500-measuring field can lend more versatility to the test setup on a laboratory scale. However, it must be ensured that a meaningful analysis of the measurements of the 500-measuring field can be carried out.

For this reason, the following steps are repeated for the 500-measuring field:

- Checking the evaluation procedure in InspectPlus
- Verification of the accuracy limit at the 40 mm gauge block
- Verification of the accuracy limit on the aluminum test specimen

- Evaluation of linear thermal expansion under space conditions on the aluminum test specimen.

The test setups already described are set up and used again, with the difference of the measuring field in the scanner.

4.6.6 Raytracing approach

In this section, the ray tracing approach for this work is derived. For the calculation of the displacement, a lock camera principle consisting of two cameras is assumed for the scanner. Figure 46 presents a schematic diagram for the determination of the theoretical ray tracing approach.

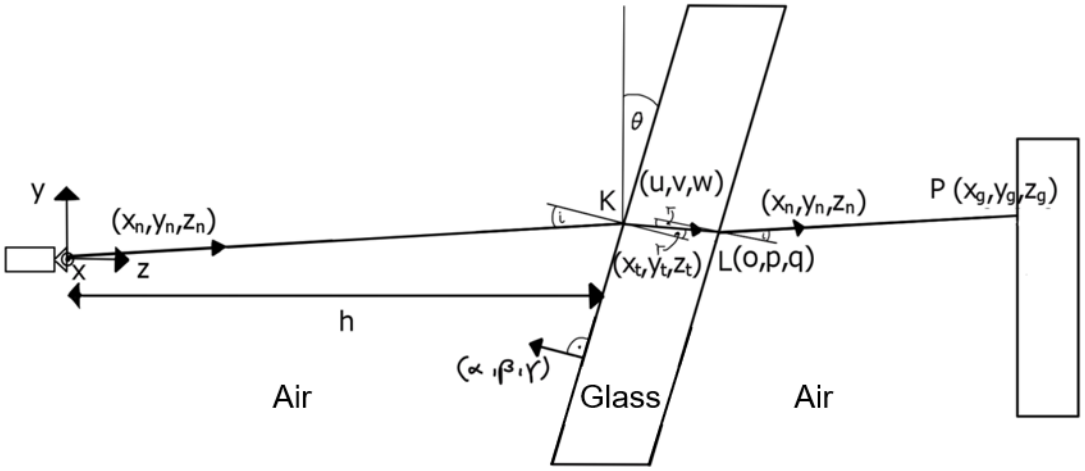

Figure 47 Schematic diagram for the theoretical calculation of the displacement.

The procedure is based on the algorithm of [Yam-04]. The scanner was simplified to two pinhole cameras, which determine the point $P = (x_g, y_g, z_g)$ in three-dimensional space. Camera 1 is the actual camera of the scanner, and camera 2 is the light source of the scanner. The origin of the system was placed in camera 1. The coordinate system was chosen so that the Z-axis corresponds to the optical direction of camera 1.

The distance of the measuring system to the object is 750 mm. The distance between the two pinhole cameras is 280 mm in the X-direction. The glass plate corresponds to a plane in the XY-plane of the coordinate system and was set up at a distance h between scanner and object. The angle change of the glass plate corresponds to a rotation around the X-axis. The angle θ describes the angular position of the glass pane in relation to the Y-axis. The beam from camera 1 to point P is described by $\overrightarrow{p_1} = (x, y, z)^T$ with the unit vector $\overrightarrow{np_1} = (x_n, y_n, z_n)^T$. The beam from camera 2 to point P is defined by $\overrightarrow{p_1}' = (x', y', z')^T$ with the unit vector $\overrightarrow{np_1}' = (x'_n, y'_n, z'_n)^T$. The normal vector

of the glass pane is represented by $\overrightarrow{n_G}(\theta) = (\alpha, \beta, \gamma)$. The meeting point of vector $\overrightarrow{p_1}$ with the glass pane is described by the point $K = (u, v, w)$. The vector of the refracted beam for vector $\overrightarrow{p_1}$ is defined by $\vec{t} = (x_t y_t z_t)^T$. With the unit vector $\vec{t}_n = (x_{tn} y_{tn} z_{tn})^T$. For $\overrightarrow{p_1}'$ of camera 2 these are $\vec{t}' = (x'_t y'_t z'_t)^T$ and $\vec{t}'_n = (x'_{tn} y'_{tn} z'_{tn})^T$ respectively. The point $L = (o, p, q)$ corresponds to the exit point of the refracted beam $\vec{t}$ and the glass pane. The meeting point of $\overrightarrow{p_1}'$ with the glass pane is the point $M = (u', v', w')$. $N = (o', p', q')$ describes the exit point of the refracted ray of camera 2 and the glass pane.

The meeting point K of Vector $\overrightarrow{p_1}$ with the glass pane can be calculated using the following formula.

Equation 14 Calculation for point of intersection K between light beam and glass surface for camera 1.

$$K(u, v, w) = \frac{h}{z_n - x_n \tan\theta} \overrightarrow{np_1}$$

The measured distance h was measured in the middle of the glass pane. Since the glass pane is rotated by the angle θ, the distance h across the surface of the glass pane is different in the y-direction shown in Figure 46. This difference is described with the term $z_n - x_n \tan\theta$ from Equation 14. The quotient of the measured distance h and the calculated difference represent a scalar. K is obtained by multiplication of this scalar with the direction vector $\overrightarrow{np_1}$.

The vector $\overrightarrow{n_G}$ can be calculated by a rotation around the X-axis. This results in $\overrightarrow{n_G}(\theta) = (0, -\sin\theta, \cos\theta)^T$. The law of Snell implies that the unit vectors of the incoming light beam, the refracted light beam, and the normal vector of the glass pane are on the same plane. This makes it possible to represent one of the three vectors as the linear sum of the other two. Thus, the refracted light beam can be described by the following formula.

Equation 15 Linear representation of the refracted light beam, as the sum of the incoming light beam and the normal vector of the glass surface

$$\overrightarrow{t_n} = \rho\, \overrightarrow{np_1} + \omega\, \overrightarrow{n_G} \text{ (I)}$$

ρ and ω are constants that must be calculated. Equation 10 applies for $\overrightarrow{np_1}$ and $\overrightarrow{t_n}$. As well as the fact that the tangential parts are equally large on the surface of the glass. From this, the following relationships result with the help of Snellius' law of refraction

$$\overrightarrow{np_1}^{\parallel} * n_1 = \overrightarrow{t_n}^{\parallel} * n_2 \text{ (II)}$$

$$\overrightarrow{t_n}^{\parallel} = \frac{n_1}{n_2} \overrightarrow{np_1}^{\parallel} \text{ (III)}$$

The vertical components of the rays run in the same direction as the normal vector $\overrightarrow{n_G}$ of the glass pane, resulting in:

$$\overrightarrow{t_n}^{\perp} = \left|\overrightarrow{t_n}^{\perp}\right| * \overrightarrow{n_G} \text{ (IV)}$$

$$\left|\overrightarrow{t_n{}^{\perp}}\right| = \frac{\left|\overrightarrow{t_n{}^{\parallel}}\right|}{\tan(r)} \text{(V)}$$

The formulae (III), (IV), (V) then yield the following result:

$$\overrightarrow{t_n{}^{\perp}} = \frac{n_1}{n_2}\frac{\left|\overrightarrow{np_1{}^{\parallel}}\right|}{\tan(r)} * \overrightarrow{n_G} \text{ (VI)}$$

In addition:

$$\overrightarrow{np_1{}^{\parallel}} = \overrightarrow{np_1} - \overrightarrow{np_1{}^{\perp}} \text{(VII)}$$

$$\overrightarrow{np_1{}^{\perp}} = \overrightarrow{n_G} * \cos(i) \text{ (VIII)}$$

The angle i between $\overrightarrow{np_1}$ and $\overrightarrow{n_G}(\theta)$ is determined via Equation 6.

$$\cos i = \frac{\overrightarrow{np_1} * \overrightarrow{n_G}}{|\overrightarrow{np_1}| * |\overrightarrow{n_G}|} \text{ (IX)}$$

Since $\overrightarrow{np_1}$ and $\overrightarrow{n_G}$ are unit vectors the following, holds true:

$$|\overrightarrow{np_1}| * |\overrightarrow{n_G}| = 1 \text{ (X)}$$

This results in:

$$\cos i = \overrightarrow{np_1} * \overrightarrow{n_G} \text{ (XI)}$$

If equation (XI) is inserted in (VIII), the result is:

$$\overrightarrow{np_1{}^{\perp}} = \overrightarrow{n_G} * (\overrightarrow{np_1} * \overrightarrow{n_G}) \text{ (XII)}$$

By inserting (XII) in (VII) the following, is obtained:

$$\overrightarrow{np_1{}^{\parallel}} = \overrightarrow{np_1} - \overrightarrow{n_G} * (\overrightarrow{np_1} * \overrightarrow{n_G}) \text{ (XIII)}$$

Now equation (XIII) is inserted into equation (III):

$$\overrightarrow{t_n{}^{\parallel}} = \frac{n_1}{n_2} * \left[\overrightarrow{np_1} - \overrightarrow{n_G} * (\overrightarrow{np_1} * \overrightarrow{n_G})\right] \text{ (XIV)}$$

Now equations (VI) and (XIV) are used in Equation 15 for the refracted beam $\overrightarrow{t_n}$. This results in:

$$\overrightarrow{t_n}. = \frac{n_1}{n_2} * \left[\overrightarrow{np_1} - \overrightarrow{n_G} * (\overrightarrow{np_1} * \overrightarrow{n_G})\right] + \frac{n_1}{n_2}\frac{\left|\overrightarrow{np_1{}^{\parallel}}\right|}{\tan(r)} * \overrightarrow{n_G} \text{ (XV)}$$

By multiplication and conversion equation (XV) becomes the following equation:

$$\overrightarrow{t_n}. = \frac{n_1}{n_2} * \overrightarrow{np_1} + \overrightarrow{n_G} * \left[\frac{\left|\overrightarrow{np_1{}^{\parallel}}\right|}{\tan(r)} * \frac{n_1}{n_2} - (\overrightarrow{np_1} * \overrightarrow{n_G}) * \frac{n_1}{n_2}\right] \text{(XVI)}$$

By inserting Equation 7, a converted Equation 8 and equation (XI) into (XVI), the result is:

$$\overrightarrow{t_n}. = \frac{n_1}{n_2} * \overrightarrow{np_1} + \overrightarrow{n_G} * \left[\frac{\left|\overrightarrow{np_1^{\parallel}}\right| * \cos(r)}{\sin(r)} * \frac{\sin(\mathrm{r})}{\sin(\mathrm{i})} - \cos(\mathrm{i}) * \frac{n_1}{n_2} \right] \text{(XVII)}$$

Due to the normalization of the vectors, the following applies:

$$\left|\overrightarrow{np_1^{\parallel}}\right| = \sin(i) \text{ (XVIII)}$$

By equation (XVIII), and further simplifications of equation (XVII), the vector $\overrightarrow{t_n}$ can be calculated with the following formula:

Equation 16 Calculation formula for a refracted beam at an interface in vector form

$$\overrightarrow{t_n}(x_t, y_t, z_t)^T = \frac{n_1}{n_2}\overrightarrow{np_1} + (\cos(r) - \frac{n_1}{n_2}\cos(i))\overrightarrow{n_G}$$

The point of intersection $L(o, p, q)$ of $\vec{t}$ and the glass pane at the exit can be determined using the following equation.

$$L(o, p, q) = s\,\overrightarrow{t_n} + \vec{K}$$

The Y-component of L can be determined using the offset a from Equation 9 and the Y-component of $K(u, v, w)$. For this purpose, the following equation is established

$$p = s * y_t + v \text{ (XIX)}$$

$$p = a + v \text{ (XX)}$$

If equation (XX) is inserted into (XIX), the result after a transformation is

$$s = \frac{a}{y_t} \text{ (XXI)}$$

With the help of s the remaining space coordinates of L can be calculated. The direction vector of the outgoing beam has the same direction as $\overrightarrow{np_1}$ (Figure 15). The displaced point $P(x_g, y_g, z_g)$ is defined by

Equation 17 Formula to determine point $P(x_g, y_g, z_g)$ for camera 1.

$$P(x_g, y_g, z_g) = b\,\overrightarrow{np_1} + \vec{L}$$

Once the constant *b* is known, the position of the point *P* is known.

The calculation of the displacement for camera 2 is the same as for camera 1. The only difference is the determination of the meeting point $M(u', v', w')$ between $\overrightarrow{np_1}'$ and the glass pane. The Z- and Y-components of *M* correspond to those of *K*. The X-component can be determined by means of the triangulation angle σ via the following formula:

$$u' = 280 - \frac{w'}{\tan\left(\frac{\pi}{2} - \sigma\right)}$$

The included angle i' between $\overrightarrow{np_1}'$ and $\overrightarrow{n_G}$ can be calculated via Equation 6. The angle r' is determined by Equation 8. $\overrightarrow{t_n}'$of $\vec{t}'$ is the result of Equation 16 and the previously calculated angles i' and r'. The intersection N between $\overrightarrow{t_n}'$ and the glass pane is given by.

$$N(o', p', q') = c\,\overrightarrow{t_n}' + \vec{M}$$

The calculation of the Y-component of N is carried out in the same way as the calculation of the Y-component of L. Thus, the constant c can be determined in the same way as the constant s. Using $N(o', p', q')$ the point $P(x_g, y_g, z_g)$ can be determined via the equation below.

Equation 18 Formula to determine point $P(x_g, y_g, z_g)$ for camera 2

$$P(x_g, y_g, z_g) = f\,\overrightarrow{np_1}' + \vec{N}$$

By equating Equation 17 and Equation 18 the constants b and f are determined, whereby the point $P(x_g, y_g, z_g)$ can be calculated.

5 Results and discussion

In this chapter, the results of the individual tests are presented and discussed directly afterwards. The reason for this is the large number of results, some of which change by only one factor and can therefore easily be confused. The results are listed according to the diagram in Figure 18. To make it easier for the reader to distinguish the results visually, the first step is to create a color code for the results. The colors refer to the background of the following diagrams.

Table 6 Color coding for the later diagrams. The colors correspond to the diagram background.

Conditions	Standardized bodies	Tactile bodies	Satellite components
simple conditions			
behind glass			
space conditions			

Once again, it should be noted that the standard deviations listed in this paper cover a 95% confidence interval. Therefore, the values correspond to twice the standard deviation calculated with Equation 2.

5.1 Results on standardized bodies

In this subsection, all the results obtained from the sphere and the 40 mm gauge block are presented. These results include the evaluation and analysis of the evaluation procedure, the elaboration of the best-practice parameters, the influence of the glass pane, the verification of the ray tracing approach, and the measurement of linear thermal expansions.

5.1.1 Verification of the evaluation procedure in InspectPlus

A random point cloud of the 40 mm gauge block was selected to check the evaluation procedure of the standardized specimen and the aluminum specimen. Using this 3D measurement, the procedure described in Chapter 4.4 was carried out 50 times. Figure 47 shows the results.

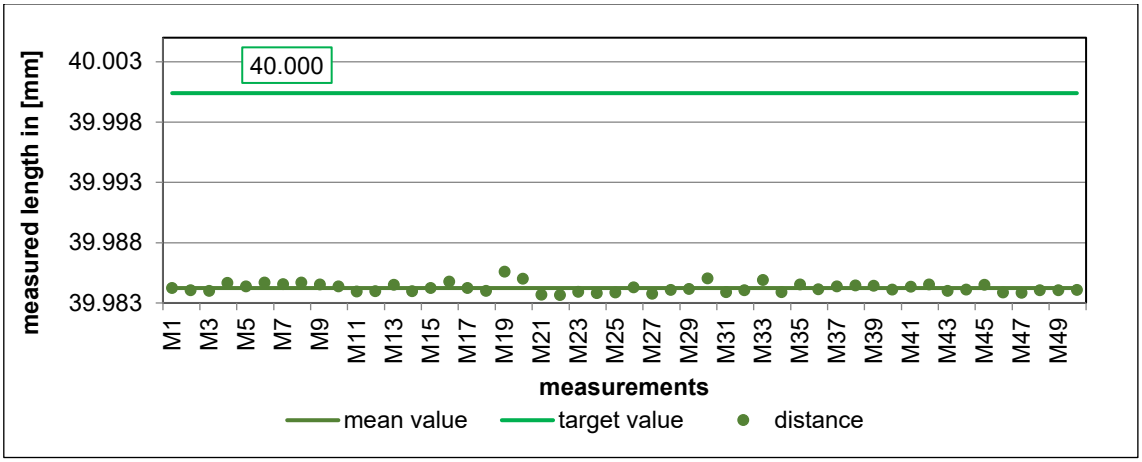

Figure 48 Evaluation of the repeatability of the evaluation procedure in InspectPlus

The evaluation shows that the maximum deviation from the mean value is 1.3 µm and the standard deviation is 0.6 µm. The precision of the evaluation is more than sufficient with 0.6 µm and is neglected for the remaining results.

5.1.2 Elaboration of the best-practice parameters

In the next step, the best practice parameters for the 40 mm gauge block are evaluated. The test setup used can be seen in Figure 32. For each series of measurements, 20 measurements were generated. The sequence of the changed parameters is described in Figure 33. The following start parameters were used for the first series of measurements.

- Exposure time: 1000 ms
- Exposure angle 45
- Ambient exposure: Off
- Additional software algorithms: Yes
- Motion: Object rotation

The result of the whole evaluation is presented in Figure 48.

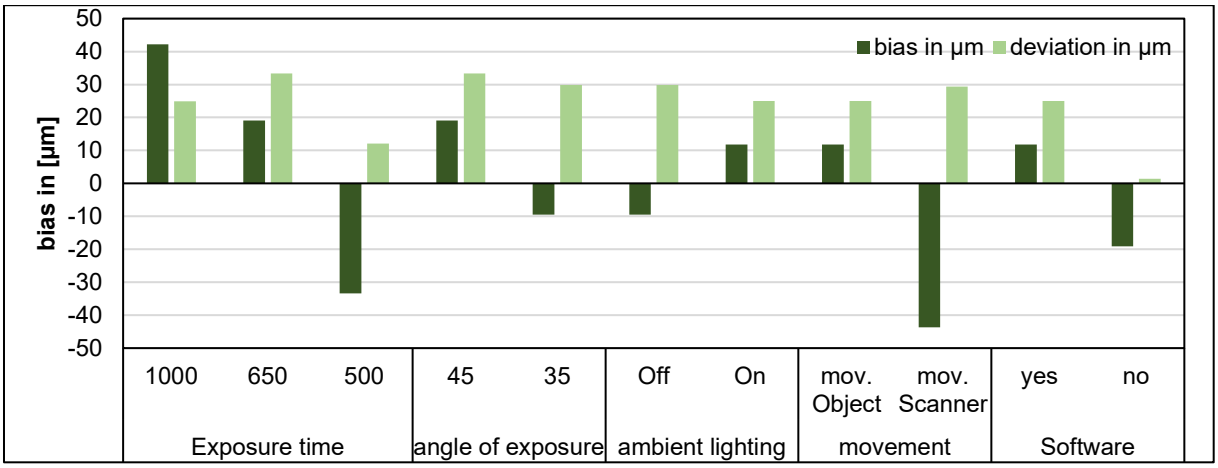

Figure 49 General overview of the best practice parameters evaluation

The demonstrated deviation values of the individual measurement series in Figure 48 are the calculated mean values from 20 3D measurements. For a better overview of the values obtained, the calculated differences and the standard deviations (s) in µm are listed in Table 7. The green columns represent the selected settings that were used for the subsequent experiments. Since the parameters were changed one after the other, the results for the 650 ms exposure time and the 45° exposure angle, for example, are the same since the initial parameters are identical except for the exposure time.

Table 7 overview of the measured biases and standard deviations of the best practice parameters evaluation

	Exposure time			Angle of exposure		Ambient lighting		Movement		Software	
	500	650	1000	45	35	Off	On	Obj	Sca.	Yes	No
bias	42	19	-33	19	-9	-9	12	12	-43	12	19
s	25	33	12	33	30	30	25	25	29	25	1

The frequent changes from oversize measurements to undersize measurements in the course of the results are striking. The results do not allow a general statement as to which parameter influences the accuracy the most. It is clear from the results that the movement of the object provides significantly better results than the movement of the scanner. However, it should be noted that the repeatability of the scanner's movement is significantly lower than the positional accuracy of the rotary table. Furthermore, it can be seen from the results that the use of additional software algorithms for the evaluation of the gauge block is not advantageous. The reason for this is the geometric simplicity of the gauge block. For a more complex component, this issue should be re-examined.

The results show that the individual parameters influence the accuracy of the scanner. The following settings were worked out as best practice parameters:

- Exposure time: 650 ms
- Acquisition angle 35
- Ambient exposure: On
- Additional software algorithms: No
- Motion: Object rotation

Using these parameters, settings were elaborated which show a systematic bias of about 20 µm with a standard deviation of 2 µm. For the following evaluations, a lower standard deviation over a lower systematic bias was preferred. Thus, a higher precision was aimed at compared to a higher accuracy.

The DoE should verify the effect of the different parameters on the accuracy of the 3D scanner. For each experiment of the DoE, the same experimental setup was used, and 5 3D measurements were created for each experiment. The evaluation of the effects can be seen in Figure 49.

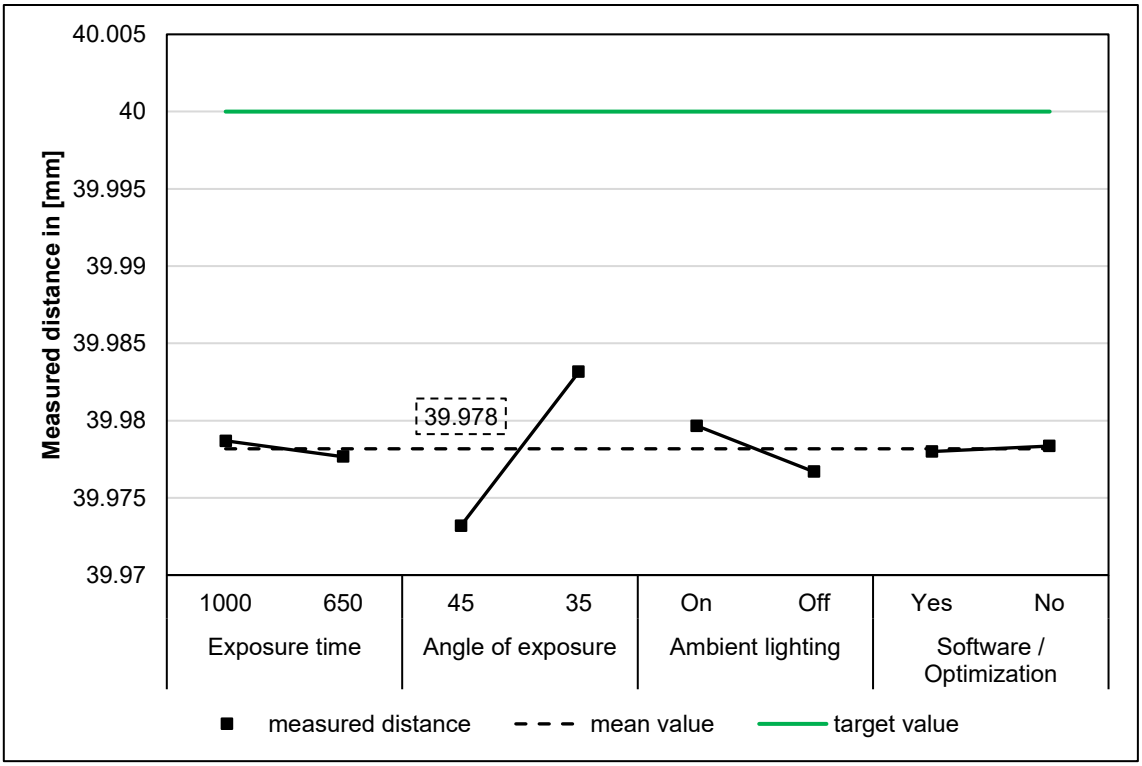

Figure 50 Representation of the effects of the individual parameters on the measured distance

From the representation of the effects, the parameter of the exposure angle has the strongest influence on the accuracy of the 3D measurement with a change of 10 µm, followed by the ambient exposure. It is noticeable that in the context of these experiments, the influence of the additional software algorithms is significantly weaker than in the previous series of experiments. An explanation for this cannot be found based on the data produced. The achieved accuracy of 20 µm from the previous experiments can also be achieved for some measurements within the scope of the DoE investigation. The mean value of the entire series of measurements is 39.978 mm, resulting in a systematic bias of 22 µm, which is slightly higher than the previously calculated bias of 20 µm. The reason for this is probably the use of the 45° acquisition angle, which was used for half of all measurements within the DoE.

In addition to the effect, the interactions of the parameters with each other could be evaluated with the help of the full factor plan. The graphical evaluation of these results is demonstrated in Figure 50. In interaction diagrams, the effects of the other parameters can be read along one row. In the diagram of Figure 51 the target value of 40 mm is not included. This was done for a better visualization of the diagram.

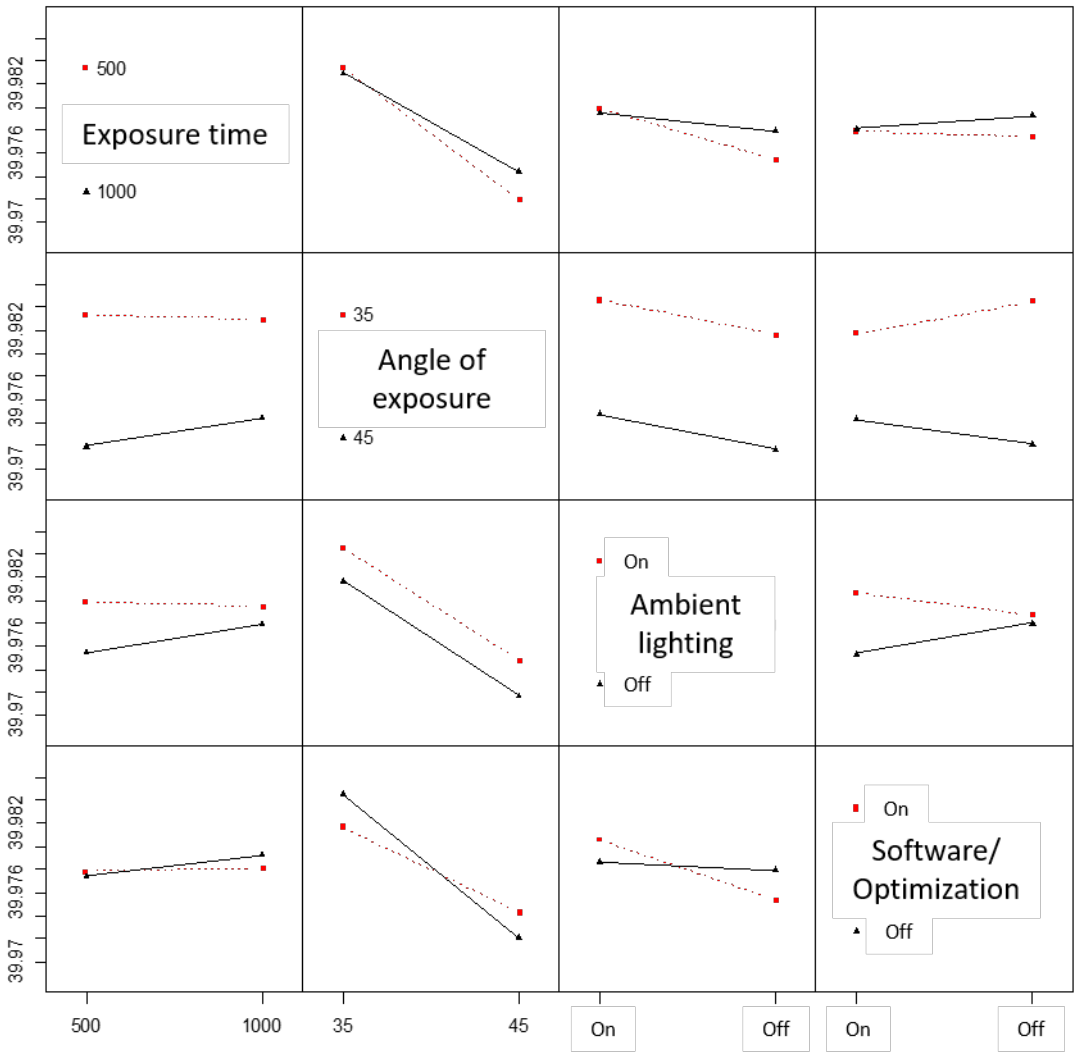

Figure 51 Interaction diagram of the studied parameters

The interpretation of interaction diagrams is complex and shall be reproduced here in a basic way. For the result-row of the exposure time, it is true that the other parameters influence the results of the exposure time. Thereby, the exposure angle exerts the strongest effect. The results of the exposure angle (2nd row in Figure 50) show that the results of the different angles are the furthest apart, which is why the strongest effect was found here, while the other parameters only slightly change the obtained values. From the row of the ambient exposure, it can be seen that with higher exposure times, the ambient exposure can be compensated. The results of the optimization or software usage will not be discussed, as the body used is not suitable for the algorithm, and thus, no meaningful interpretation is possible.

To ensure that the DoE results presented here are all statistically significant, an ANOVA analysis [Bas-20] was performed. The results of the ANOVA can be seen in Table 8. The null hypothesis for this analysis has an α of 0.05, and the hypothesis is that the parameters have no effect on accuracy.

Table 8 ANOVA for effect evaluation of DoE for the best practice parameters.

	Test value (F)	P-value	critical F-value
Exposure time	0.1096	0.7454	4.6001
angle of exposure	35.7268	0.0000	4.6001
ambient lighting	0.9726	0.3407	4.6001
software	0.0127	0.9118	4.6001

From the ANOVA, only the angle of exposure causes a statistically significant change in the mean values, thus disproving the null hypothesis. The remaining parameters are statistically insignificant as the P-value is greater than 0.05. For this reason, only the angle of exposure from the results of the DoE is used to determine a general accuracy limit. The mean value of the systematic deviation is 22 µm for the DoE and 19 µm for the conventional test method. For simplicity, the limit thus determined is set at 20 µm. This value is to be seen as a kind of benchmark for future measurement series and not a fixed value that has to be reached. Since this value was obtained based on a worst-case component, the results of future measurement series can be better seen and analyzed in relation. Thus, it was elaborated that the overall accuracy of the scanner for a worst-case scenario, such as the 40 mm gauge block, is 20 µm. The angle of exposure exerts the largest and only statistically significant effect on the accuracy of the scanner; this result is consistent with the results of S. Gerbino et al. [Ger-16]. That the ambient exposure is statistically insignificant is consistent with the results of F. Li et al. [Li-17]. That the exposure time has no statistical significance according to the DoE results is important for the further results, because the exposure time depends especially on the nature of the object, such as color and material.

For the continuing results, the accuracy of 20 µm achieved here is used as a limit or benchmark. This value is better than the obtained accuracies of [Ber-13] and [Geo-10] which obtained threshold values of 50 µm for matted test specimens. The strong difference between the results, especially with respect to the high standard deviation of 0.174 mm of Bernal et al. [Ber-13] may be related to the used scanning software. This software has been continuously improved and updated by Zeiss over the years. The value of 20 µm achieved here, however, is higher than the result of [Gue-20] of 5 µm, but it must be noted that M.G. Guerra et al. used a smaller measuring field and the ATOS system has two cameras.

5.1.3 Influence of the glass pane on the accuracy of the 3D scanner

The next step is to evaluate the influence of the glass pane. For this purpose, the test setup from Figure 38 was used. First, the results for the angles 90°, 72° and 54° are shown. Figure 51 shows the results of the 3D measurements.

Figure 52 Evaluation of the determined distances for the different angle and distance combinations.

Figure 51 illustrates the expected behavior of the measured values, namely that the systematic deviation also increases with increasing angle. The behavior within the respective angular position with respect to the distance is also homogeneous. The closer the scanner is to the glass, the greater the deviation. For a more detailed evaluation, the calculated mean values of all angle and distance combinations are listed in Table 9.

Table 9 Evaluation of the mean values for measurements through glass for the 90°,72° and 54° angles.

angle distance	90°	72°	54°
450 mm	40.023	40.070	40.120
490 mm	40.015	40.062	40.111
530 mm	40.010	40.059	40.096

The numerical values from Table 9 show that the difference between the individual angular positions of the glass over all distances is 46 µm on average. A change in the angular position of the glass pane by 1° changes the accuracy of the measurement procedure by 2.5 µm. To confirm this statement, the second series of tests was carried out, this time with all angle and distance combinations. The results of this evaluation are demonstrated in Figure 52.

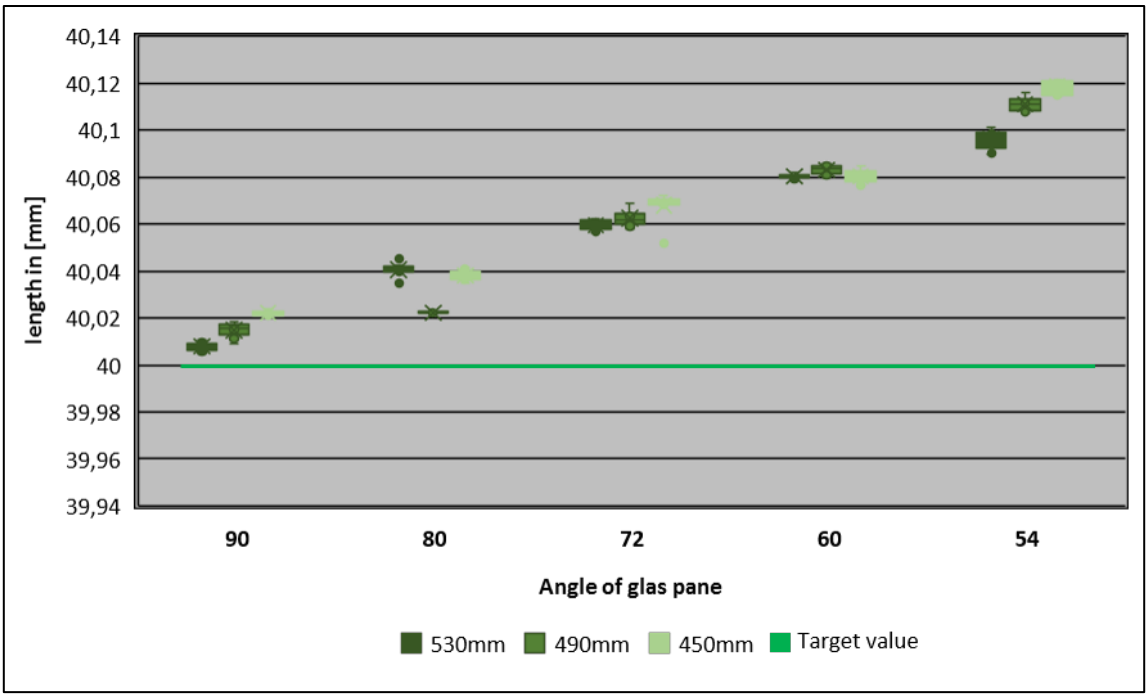

Figure 53 Evaluation of the determined distances for the different angle and distance combinations of the second test series for scanning through glass.

The general behavior of the second test series is like the previous one. The systematic deviation increases with increasing angle. The behavior of the distances is no longer homogeneous in this test. A reason for this cannot be found based on the data. In order to verify the result of 2.5 µm, the calculated mean values of the respective angle and distance combinations of the second test series are presented in Table 10.

Table 10 Evaluation of mean values for measurements through glass for all angle and distance combinations.

angle distance	90°	80°	72°	60°	54°
530 mm	40.007	40.040	40.059	40.080	40.095
490 mm	40.014	40.022	40.062	40.083	40.111
450 mm	40.022	40.038	40.068	40.080	40.118

An evaluation of the mean measured lengths from Table 10 shows that a 1° change in the angle of the glass pane increases the measured length by 2.46 ± 0.56 µm. Thus, the result of the first test series was successfully verified.

In addition to evaluating the measured lengths, possible geometric changes in the scanned object were also checked. For this purpose, a nominal/actual superimposition was performed in InspectPlus. First for 3D measurements of the 40 mm gauge block based on one scan and subsequently for scans based on two views. 3D measurements from 90°, 72°, and 54° angles were used for the superpositions. The results for the overlays of the scans based on one view are given in Figure 53.

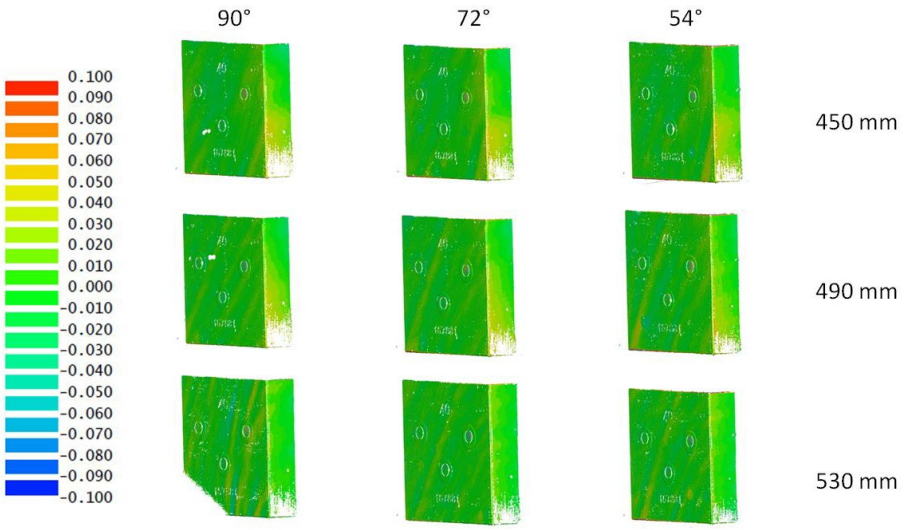

Figure 54 Overview of overlays based on 3D measurements with a single view

Figure 53 indicates that the increasing angular position does not lead to any change in the geometric shape. It is noticeable that the deviations are almost constant over all angular positions, and no deterioration occurs. Thus, it can be hypothesized that 3D measurements based on a single view are less affected by the glass pane. But first, the superpositions of the 3D measurements of the 40 mm gauge block based on two views are considered. The results of the first view are displayed in Figure 54, the overlays of the second view are presented in Figure 55.

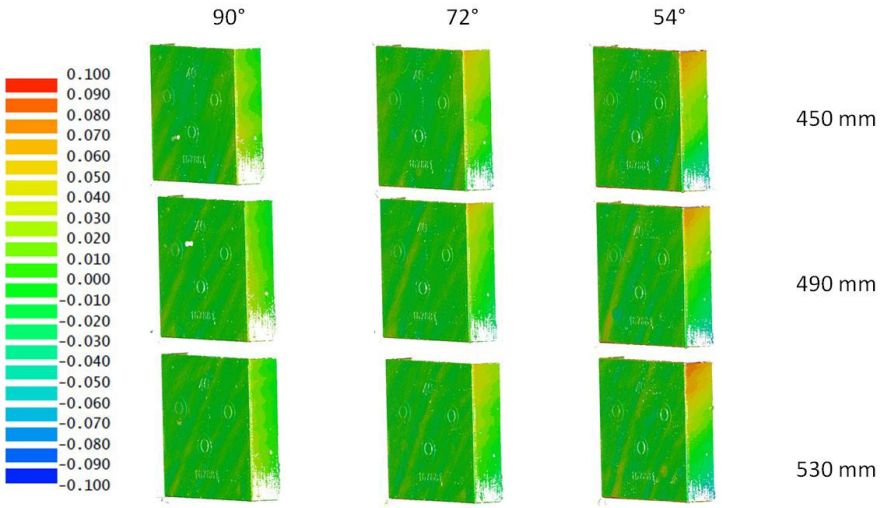

Figure 55 Overview of the overlay based on 3D measurements with two views (view 1)

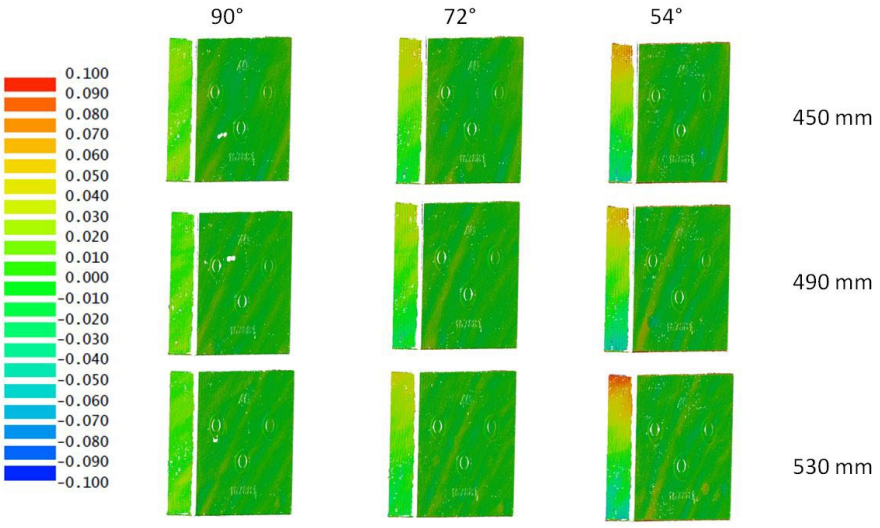

Figure 56 Overview of the overlay based on 3D measurements with two views (view 2)

A clear effect of the glass pane can be seen from the two figures. The overlays for the 3D measurements of the 54° angular positions show most clearly that the parallel faces of the gauge block have an inclined position to each other, and the scanned gauge block takes on more of a trapezoidal shape instead of a square. This shows that the glass pane not only affects the length measurements between the relevant planes but also changes the geometric shape of the object.

The hypothesis that scans based on a single view are less affected by the glass pane was tested using the measurement sphere from Figure 19. The comparison of the results with and without the glass pane for the sphere is shown in Figure 56.

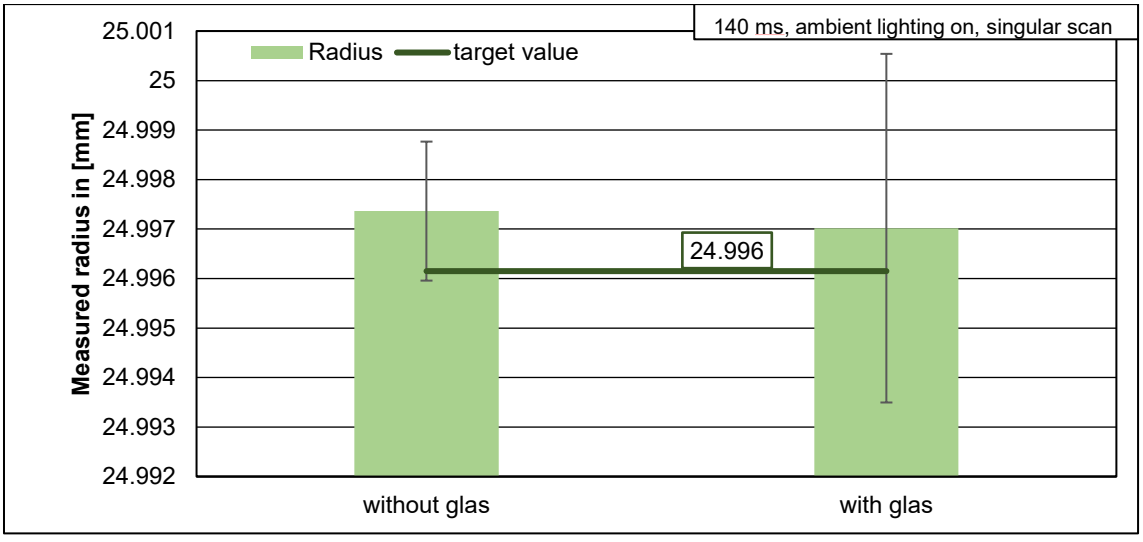

Figure 57 Comparison of scans based on a view with and without glass for the measuring sphere

The comparison in Figure 56 demonstrates that the glass pane does not cause any systematic deviation for scans based on one scan. From the higher standard deviation of the measurement series with the glass pane, it can be concluded that the glass pane also slightly deforms these scans geometrically and thus causes the evaluation to fluctuate more. Nevertheless, the deviation of the worst scan with the glass, which

measured a radius of about 25.0005 mm, is 4 µm, which is well below the established 20 µm limit. This initially proved the previously stated hypothesis that the glass pane affects 3D measurements based on a single view less. This fact is still validated on the tactile measured aluminum body within the scope of the work.

5.1.4 Testing the ray tracing approach

The ray tracing approach is checked with the help of exported point coordinates. For the point coordinates, one data set comes from a measurement with an angular position of 90° and another data set from a measurement with an angular position of 72°. Both measurements were made with the same distance between scanner and glass. Table 11 lists the spatial coordinates of the points and their direct distances to each other.

Table 11 Listing of spatial coordinates of points P1 and P2 for both 3D point clouds in mm

coordinates test series	X	Y	Z
P1 90° 530 mm	-21.194	-7.007	9.533
P2 90° 530 mm	-3.075	-6.370	-2.952
P1 72° 530 mm	-21.263	-4.803	9.508
P2 72° 530 mm	-3.147	-4.168	-2.984
distance P1 90° to72°	0.069	-2.204	0.025
distance P2 90° to 72°	0.072	-2.202	0.032

The average change in the X and Z directions over the different angular positions of the glass pane from Table 11 with 70 µm and 28 µm each and with 3.8 µm and 1.5 µm per degree change of the glass pane, respectively, are in the immediate scale of the experimentally worked out change of 2.4 µm. However, the displacement must be considered as a 3D dimensional problem. The performed distance measurements include possible rotations of the created planes with respect to each other and are therefore not simple length measurements in only one spatial direction.

For this purpose, a graphical verification of the ray path based on the ray tracing approach was performed. The described formulas were used to reconstruct the rays in Siemens NX. The result of the check can be seen in Figure 57.

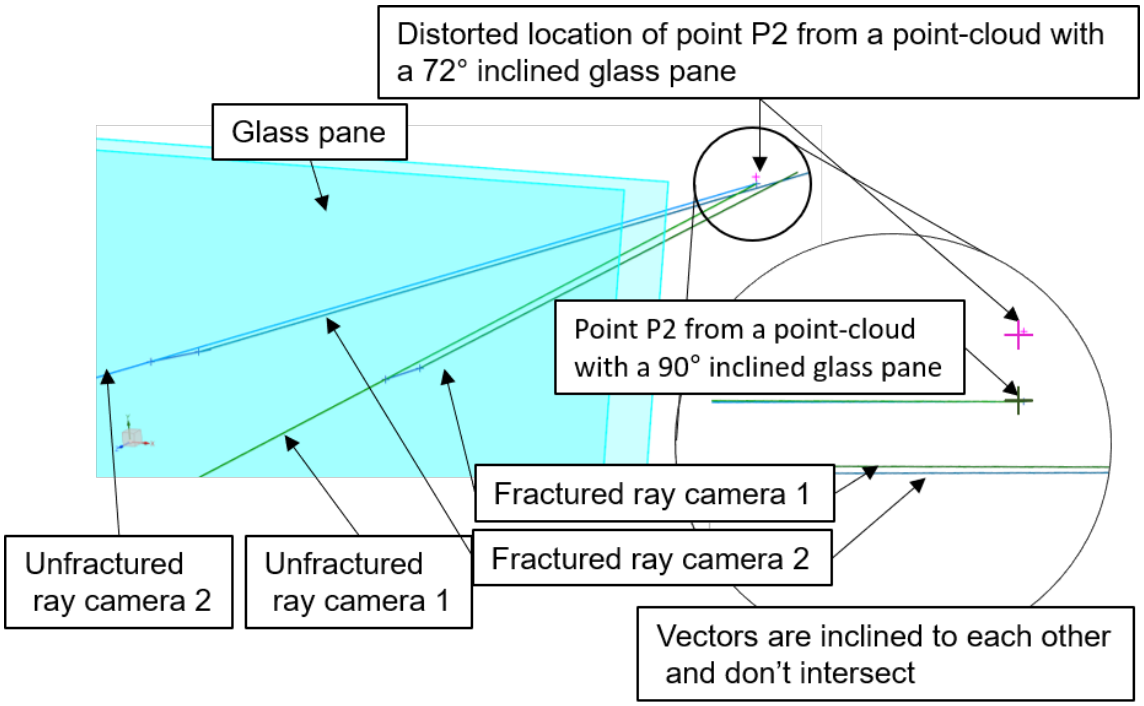

Figure 58 Graphical representation of the ray path based on the assumptions and the elaborated theory.

The figure indicates that the rays from camera 1 and camera 2 are at an angle to each other and therefore have no point of intersection. This result was also obtained by the calculation of the point coordinates from Table 11 with the formulas from chapter 4.6.5. Furthermore, it can be seen in Figure 57 that the actual displacement of the points in the Y-direction is in the opposite direction as the theoretical displacement. However, the value of the displacement of approx. 2 mm agrees. That the used approach of [Yam-04] shows measurement errors or calculation errors was already shown in the work of Pallone et al. [Pal-12]. The errors shown here seem to be smaller than 1.863 mm [Pal-12].

Thus, it can be stated that with the developed ray tracing approach the displacement of the point coordinates cannot be predicted or calculated. This can have a variety of reasons. On the one hand, the ray tracing approach is a model of static assumptions, whereas reality requires a certain dynamic. Due to the manual set-up of the experimental setup, it is quite possible that the glass pane has a twist around an additional axis; even if this twist is minimal, it influences the course of the ray. Furthermore, in the elaborated theoretical approach, only vectors are used for the calculation of points, whereas the scanner uses planes and vectors for the calculation of three-dimensional coordinates. In addition, it must be noted that the point coordinates are obtained by a rotation of the object, which is not considered in the ray tracing approach. This means that the coordinate system of the scanner remains constant over all measurements, but the coordinate system of the object rotates by a defined angle from measurement to measurement.

Since the use of the ray tracing approach does not provide the hoped-for results, the focus of the following series of measurements was shifted to the use of scans based on a single view by adding an additional glass pane.

5.1.5 Measurement of linear thermal length expansion

The test setup from Figure 37 is used for the results of the linear thermal expansions. For the evaluation of the measurements, the already used method of the planes as well as the method based on the vectors, is used. First, the measured temperatures at the front and back of the gauge block are demonstrated in Figure 58 so that the linear thermal expansions can be calculated.

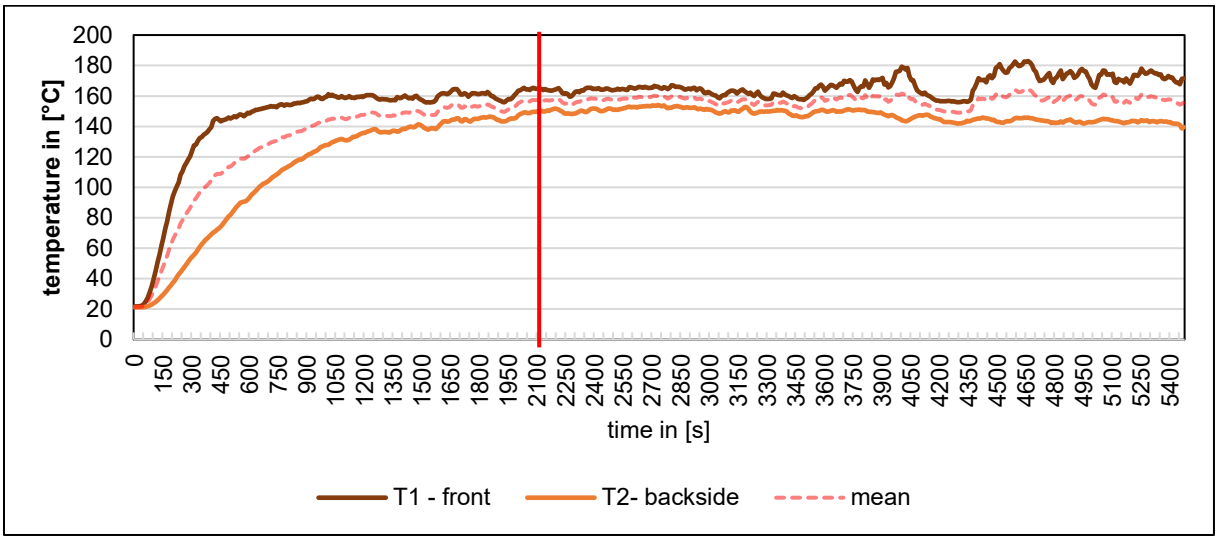

Figure 59 Temperature measurement on the front and back of the 40 mm gauge block for measuring linear thermal expansion.

Using the determined mean temperature shown in Figure 58, the theoretical linear thermal expansions for the 40 mm gauge block were calculated. The coefficient of expansion used is $11.6 * 10^{-6} \frac{1}{K}$ [Pre-17]. The results for the plane-based evaluation are shown in Figure 59.

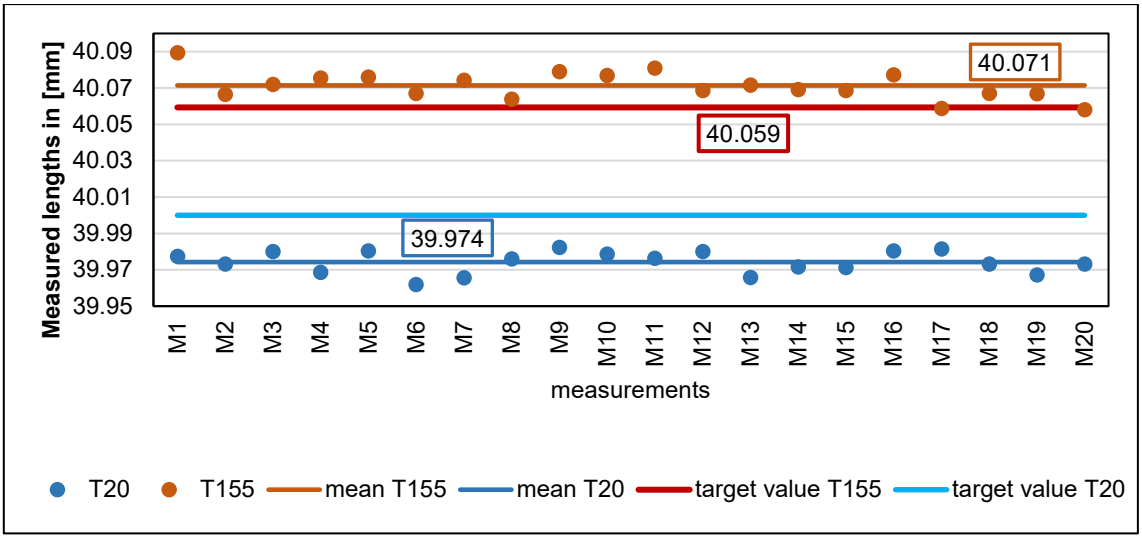

Figure 60 Evaluation of the linear thermal expansion with the aid of the plane method

The diagram in Figure 59 presents the measured lengths based on the plane method at room temperature (blue data series) and at a temperature of 155 °C (red data

series). For the test series at room temperature, the accuracy achieved is just above the target limit of 20 µm, with a deviation of 26 µm. For this evaluation, however, it must be noted that in this test series, the scanner was moved instead of the object. For this circumstance, the result obtained is significantly better than the results from the evaluation of the best practice parameters in Figure 48.

The observation of the series of measurements at 155 °C reveals a better result in comparison to the series of measurements at 20 °C. The deviation of the measured expansion from the theoretical expansion for this test series is 12 µm and thus below the 20 µm limit. This demonstrated, using a normalized measurement scanner, that it is possible to measure linear thermal expansion using a 3D scanner.

Since the ray tracing approach did not yield the hoped-for results and rotation of the components in a vacuum is only possible to a limited extent, another evaluation method for the measurement of linear thermal expansions is being tested. This vector method was explained in chapter 4.4. The underlying measurements were obtained using the same experimental setup. The results of the evaluation are demonstrated in Figure 60.

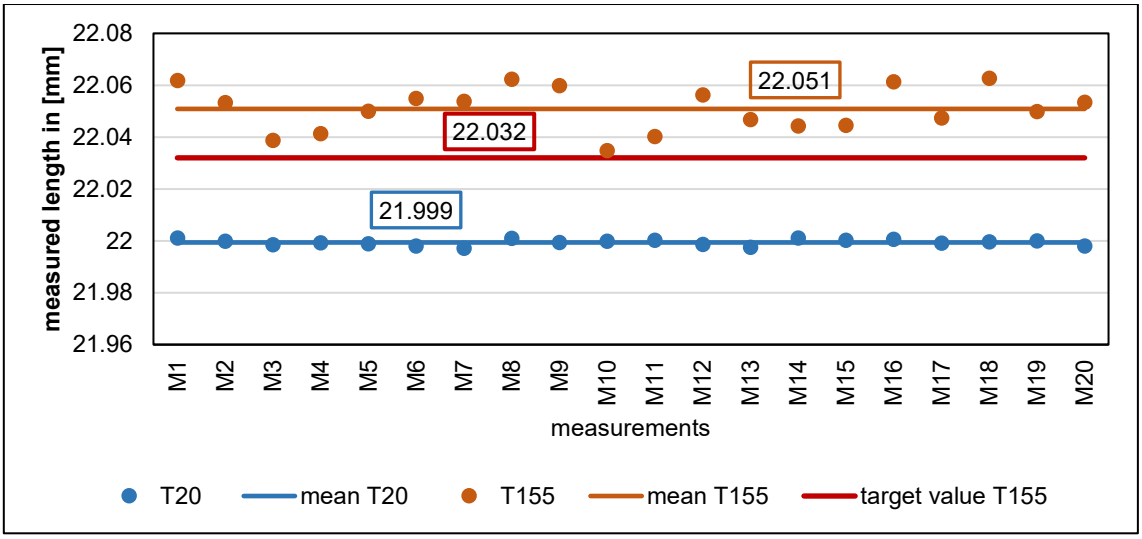

Figure 61 Evaluation of linear thermal expansions using the vector method

The results from Figure 60 show that the vector evaluation for the measurements at 20 °C is subject to only minor fluctuations. For the measurements at 155 °C, the fluctuations are significantly higher, but no direct explanation can be found. The measured lengths show that the deviation from the theoretical value of the expansion is 19 µm. Thus, the thermal length expansions can also be done with the help of the vector method and the underlying measurement marks.

5.1.6 Measurements under space conditions on an industrial scale

The vector method was used to evaluate the measurements in the vacuum system of the JUST company. The experimental setup is shown in Figure 40. The results of the evaluation are displayed in Figure 61.

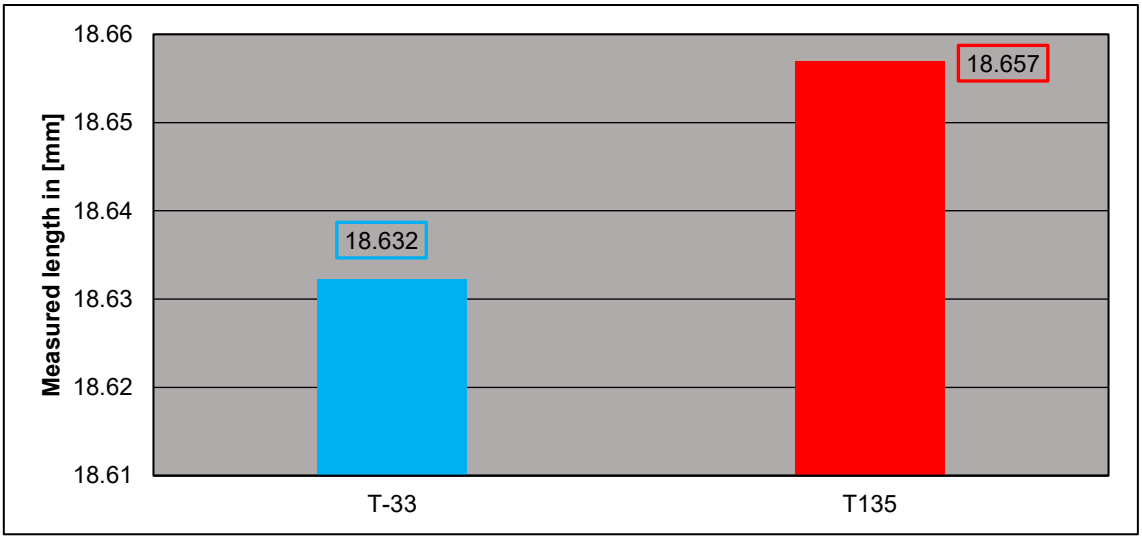

Figure 62 Evaluation of the linear thermal expansion under space conditions on an industrial scale for a standardized measuring body (30 mm gauge block)

The values shown are the calculated average values of the 8 measurements. The expansion coefficient of the gauge block is also $11.6 * 10^{-6} \frac{1}{K}$ [Pre-17]. For a better overview of the theoretical expansion and the measured expansion, the values are listed in Table 12.

Table 12 Theoretical and measured linear thermal expansion of the 30 mm gauge block under space conditions.

Theoretical extension	Measured expansions	Difference
0.036	0.025	0.011

The evaluation demonstrates a deviation of 11 µm for the series of measurements under space conditions on an industrial scale. With this satisfactory result, it was demonstrated on a standardized measuring body that the linear thermal expansions under space conditions can be evaluated using a 3D scanner. However, since the measurement consists of only eight measurements, this statement is verified using the tactilely measured aluminum body.

5.1.7 Conclusion for the results on standardized test specimen

Using the standardized measuring bodies, in this case, a 40 mm gauge block and a measuring sphere, the evaluation procedure was first verified. With a standard deviation of 0.6 µm for the plane measurements, the evaluation procedure was successfully validated. The standard deviation of the measurement procedure in InspectPlus was ignored for the rest of the work. Furthermore, using the worst-case scenario of the 40 mm gauge block, the accuracy limit of 20 µm was developed and set as a benchmark for this project.

The influence of an additional glass pane increases the systematic deviation of the length measurement by 2.5 µm per degree of angle change of the glass pane. This statement is only valid for 3D measurements based on two views. 3D scans based on one view are less to not influenced by the glass pane, but this statement still needs to

be confirmed using the tactile measuring body. Through the superpositions, it became apparent that the glass pane not only influences the length measurement but also changes the geometric shape of the scanned object. The developed ray tracing approach does not show positive results and will not be used for the further work of this thesis.

Based on the presented experiments, it can also be confirmed that thermal length expansions can be measured with the help of a 3D scanner. The plane method as well as the vector method, can be used.

5.2 Results on tactile measured bodies

In this chapter, the results obtained from the tactile measured aluminum body are presented. First, the results obtained are validated on the standardized bodies. This includes the developed accuracy limit of 20 µm as well as the confirmation of the hypothesis that an additional glass pane only minimally influences the measurement results of the 3D scanner if the 3D scans only consist of a single view. Throughout this subsection, temperature measurements within the vacuum chamber are presented. Furthermore, linear thermal expansions under space conditions are performed and evaluated. Measurements based on a single view are created, as well as measurements using the rotation manipulator.

5.2.1 Validation of the scan accuracy

The test setup from Figure 35 was used to validate the results already obtained on the aluminum test specimen. The exposure time had to be adjusted due to the surface of the body and therefore did not match the best practice parameters. The point clouds for the validation consist of three views. A total of 50 measurements were made. The results of the validation are shown in Figure 62.

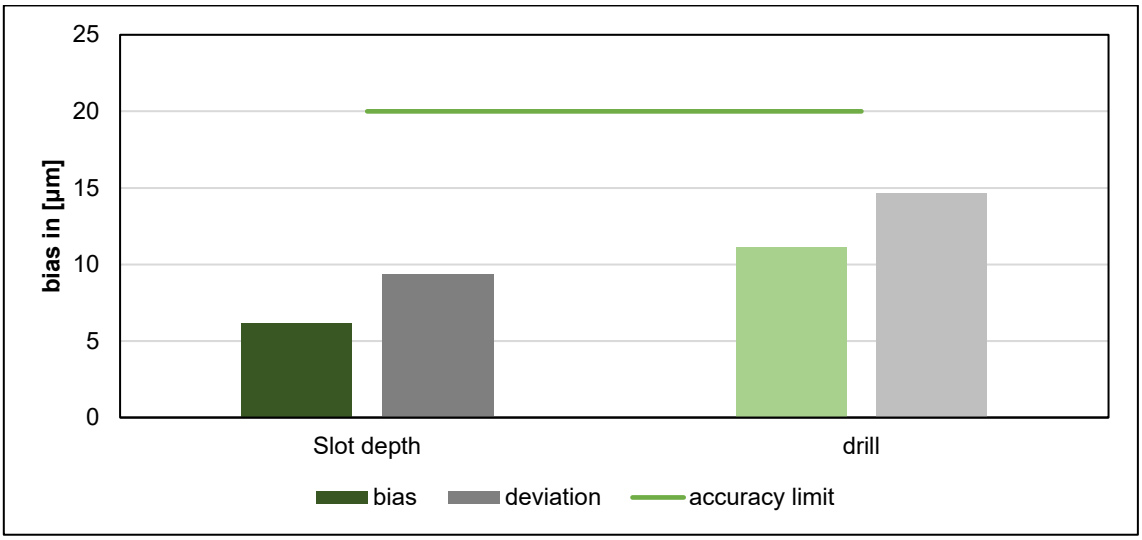

Figure 63 Results for the measurement series to validate the 20 µm limit on the aluminum test specimen

From the diagram in Figure 62 the results obtained for the depth of the pocket and the 5 mm hole are below the 20 µm limit. That the results for the drill hole are less good was to be expected. The cylindrical surface of the drill hole cannot be measured in its entire depth. Furthermore, the three views are not sufficient to completely scan the cylindrical surface. For this reason, the deviation, as well as the standard deviation of the results of the bore, is larger than the results of the depth of the pocket. Through these results, the accuracy limit for the aluminum gauge body could be validated.

5.2.2 Influence of component position and number of scans

Due to the different test setups within the vacuum chamber, the component must be repositioned during the alterations. For this reason, the aluminum body is used to check the influence of the component position. In addition, a comparison is made between 3D scans with multiple views and 3D scans from a single view to reveal a possible effect of the number of views. The test setup from Figure 35 was also used for these measurements. The three positions checked are shown in Figure 36. For each position, 25 measurements were generated. The exposure times vary across the different component positions. The comparison of the results is shown in Figure 63.

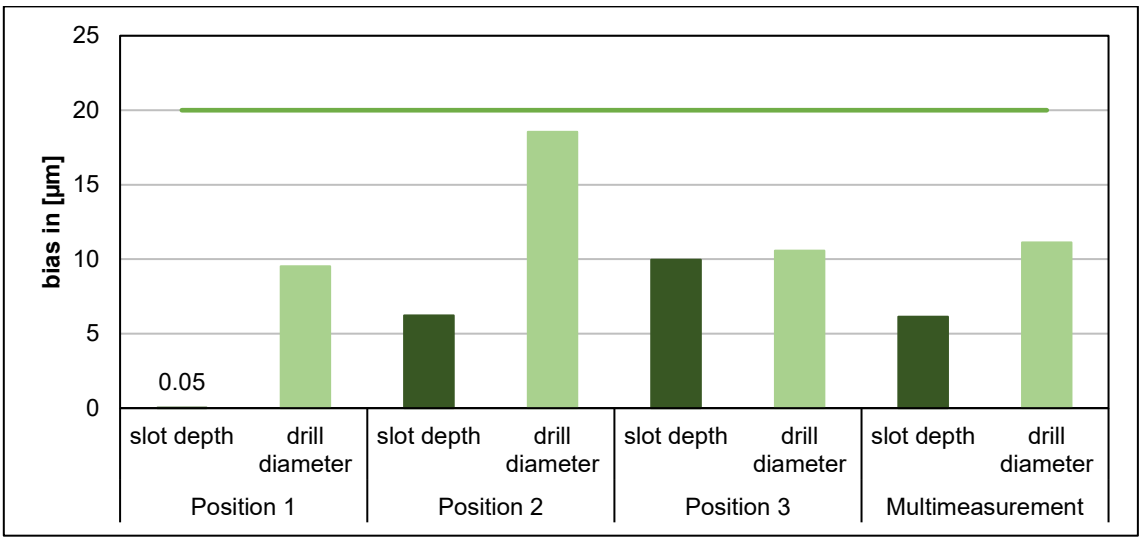

Figure 64 Results for the different component positions and number of scans for the aluminum test specimen.

The results show that the component positions evidently have an influence on the results obtained. Furthermore, no direct difference is seen between the series of measurements based on a single view and the series of measurements using multiple views. All results are below the 20 µm limit and, as before, the measurements for the drill hole achieve less good results. Whether the differences for the component positions are statistically significant is shown by another ANOVA. The null hypothesis that the component position has no influence occurs with a probability of 0.05. The results of the ANOVA are shown in the following table. The results of the ANOVA are listed in Table 13.

Table 13 ANOVA results for the studied form elements under different component positions.

	Test value (F)	P-value	critical F-value
slot depth	157.9389	4.6 E-27	3.1239
5 mm drill	219.2464	2.3 E-31	3.1239

Evaluation of the single factor analysis of variance shows that the differences between the individual component positions are statistically significant. The test variable F exceeds the critical F value enormously in both cases, and the calculated P value is well below 0.05. Thus, the null hypothesis that the component position exerts no influence was refuted. For further tests, this means that at least two different component positions should always be checked if this is possible.

5.2.3 Influence of the glass pane

The glass pane used in the vacuum chamber is not the same pane that was used for the results of the standardized test specimens. With the help of the new glass panes, a series of measurements was carried out to check whether only a slight influence can be detected with these glass panes in scans based on a single view. The corresponding test setup is described in Figure 39. Due to the different angles of the glass panes, the scanner had to be repositioned between the series of measurements.

In the scans, it is immediately apparent that these glass panes strongly influence a local area of the point clouds. An example of this can be seen in the marked red area in Figure 64.

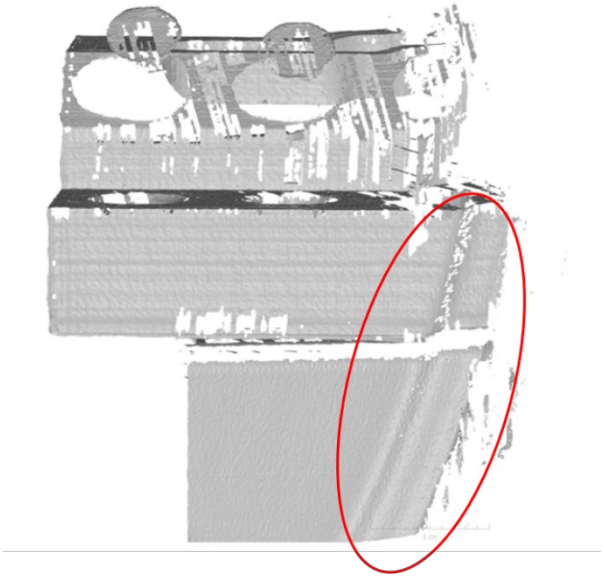

Figure 65 Scan of a component through the sight glasses installed in the vacuum chamber. Marked red area shows the displacement through the glass pane.

This local area corresponds to the bulge at the outer edge of the viewing glasses, which can be seen in Figure 27, and is directly transferred into the point cloud. The test series carried out should show that this local area does not influence the rest of the point cloud and that a meaningful analysis of the scanned areas is possible. The

result of the two series of measurements through the sight glasses is presented in Figure 65. Glass 1 corresponds to the large viewing glass, and Glass 2 to the small viewing glass.

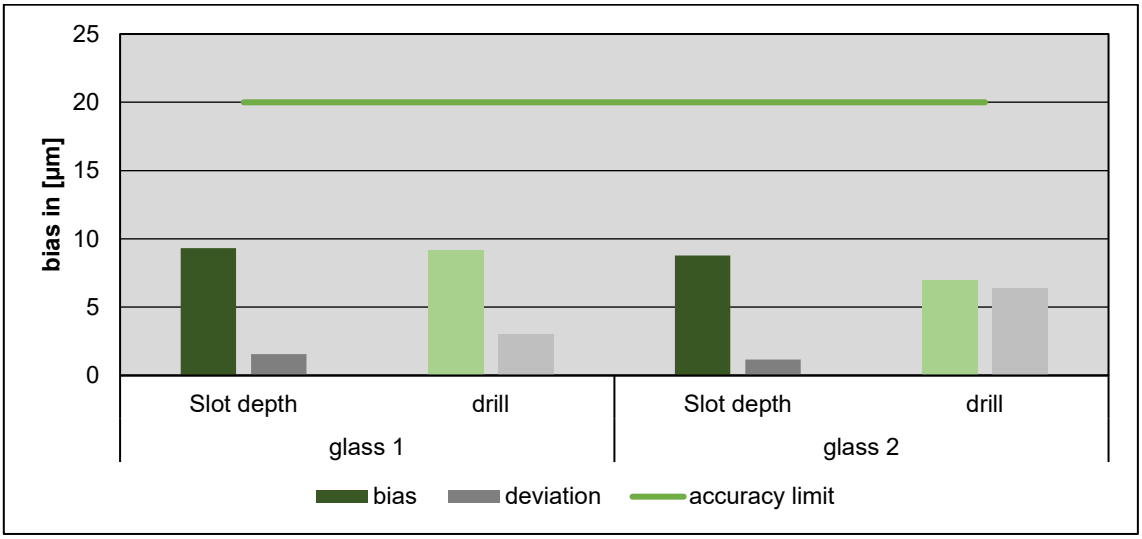

Figure 66 Results for the measurement series through the sight glasses installed in the vacuum chamber.

The results in Figure 60 show that there is no obvious difference between the glass panes. In general, the results also show that for both series of measurements, the deviations are below the 20 µm limit, and therefore, no direct effect of the glass pane on the systematical bias can be detected. To ensure that the different glass panes do not have a statistically significant effect on the results, a single factor analysis of variance was also performed for these results. The null hypothesis that the glass panes do not exert a differential effect on the measurement results occurs with a probability of 0.05. The results of the ANOVA are listed in Table 14.

Table 14 ANOVA results for the studied mold elements by the different glass panes of the vacuum chamber.

	Test value (F)	P-value	critical F-value
slot depth	2.5205	0.1189	4.0426
5 mm drill	2.3039	0.1356	4.0426

The ANOVA indicates that the results through the different glass panes do not show a statistically significant difference since the test size is smaller than the critical F-value and the P-value is larger than 0.05. Overall, the results of the normalized test specimens were thus validated on the tactile measured test specimen and extended to include the glass panes of the vacuum chamber.

5.2.4 Results under space conditions

The next step is the evaluation of linear thermal expansions under space conditions. For this purpose, the results of the temperature measurements inside the vacuum chamber are shown first. The measuring points are shown in Figure 43 for the warm temperatures, and Figure 44 illustrates the measuring points for the cold temperatures. For the heating experiments, the evaluation of the recorded temperatures is shown in Figure 66. The temperatures for the cold tests are demonstrated in Figure 67.

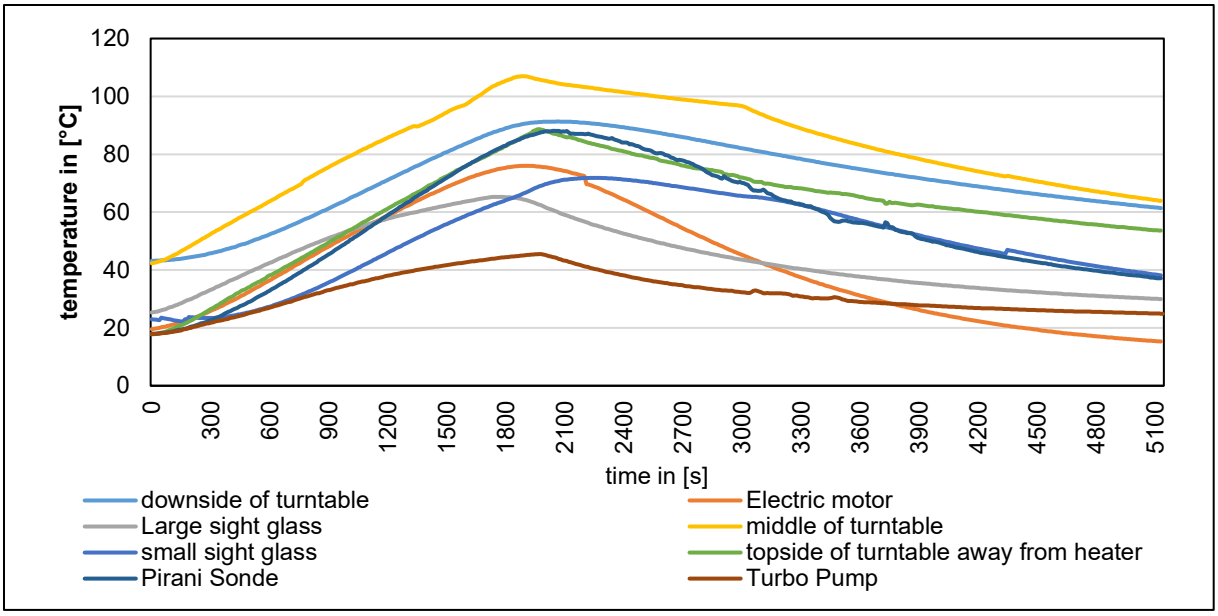

Figure 67 Overview of the measured temperatures for the heating experiments under space conditions.

The evaluation of the temperature data shows that no critical values, such as those of the copper seals, the glass panes, and the Pirani probe, are exceeded. This ensures that the temperature tests with components do not endanger the proper functioning of the vacuum chamber. These tests only represent the measured temperature at the specified locations and do not represent the complete temperature behavior inside of the vacuum chamber. This would require more comprehensive tests.

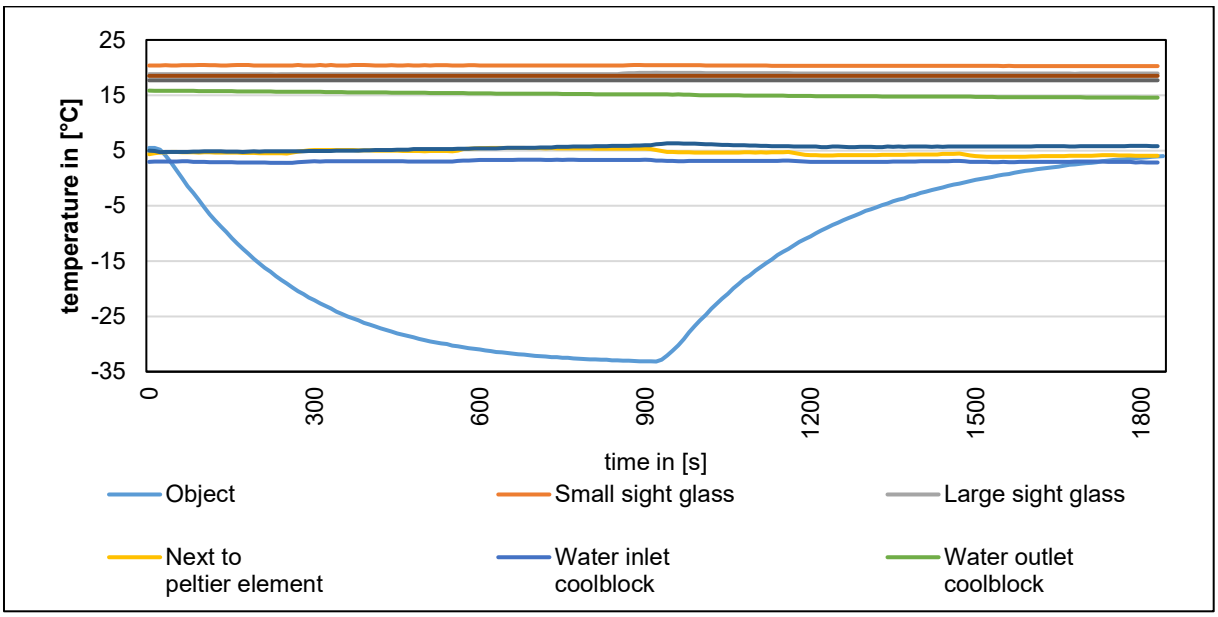

Figure 68 Overview of the measured temperature for the cold tests under space conditions

The evaluation of the cold tests shows that the Peltier element cools the component to approx. -33 °C, but the rest of the chamber does not change the temperature. The aluminum cooling block through which ice water flows also does not have a constant temperature, which is approximately the temperature of the ice water of about 3 °C.

The next step is to evaluate the temperature distribution along the component under space conditions. For this purpose, the temperatures were measured at three points along the body. The measurement locations are shown in Figure 45. The results of the evaluation are shown in Figure 68.

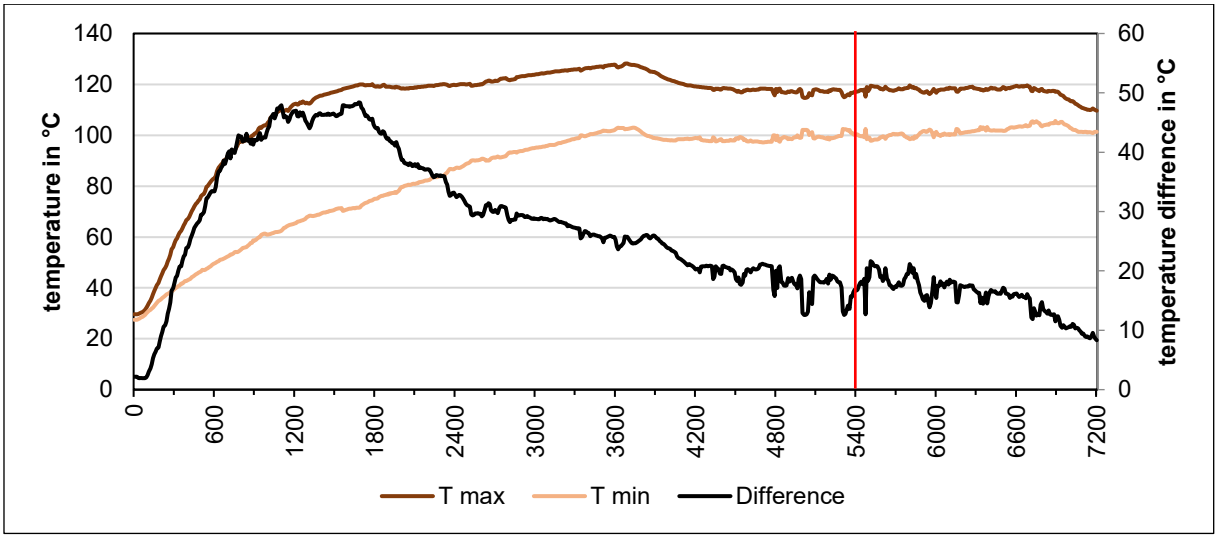

Figure 69 Representation of the minimum and maximum temperauts along the aluminum measuring body under space conditions.

The temperature curves shown correspond to the measuring point closest to the heating element (T_{max}) and the measuring point at the other end of the component (T_{min}). As expected, the temperature difference is very high at the beginning of the test series, but it continues to decrease with increasing time. The diagram shows that the temperature tests must be heated up for at least 90 minutes (5400 s) so that the temperature difference is less than 25 °C. Such a difference makes only a minimal change for the evaluated form elements or their length. Table 14 lists the differences in µm.

Table 15 Listing of the different thermal length changes for the measured minimum and maximum temperature.

	ΔT 105 °C	**ΔT 85 °C**	**difference**
slot depth	18.50 µm	14.09 µm	4.40 µm
6 mm drill	14.59 µm	11.11 µm	3.47 µm

However, in order to be able to make a better statement about the effects of the temperature difference, the results of the evaluation of the thermal length change must be demonstrated. An overview of all the series of measurements carried out and their results can be seen in Figure 69.

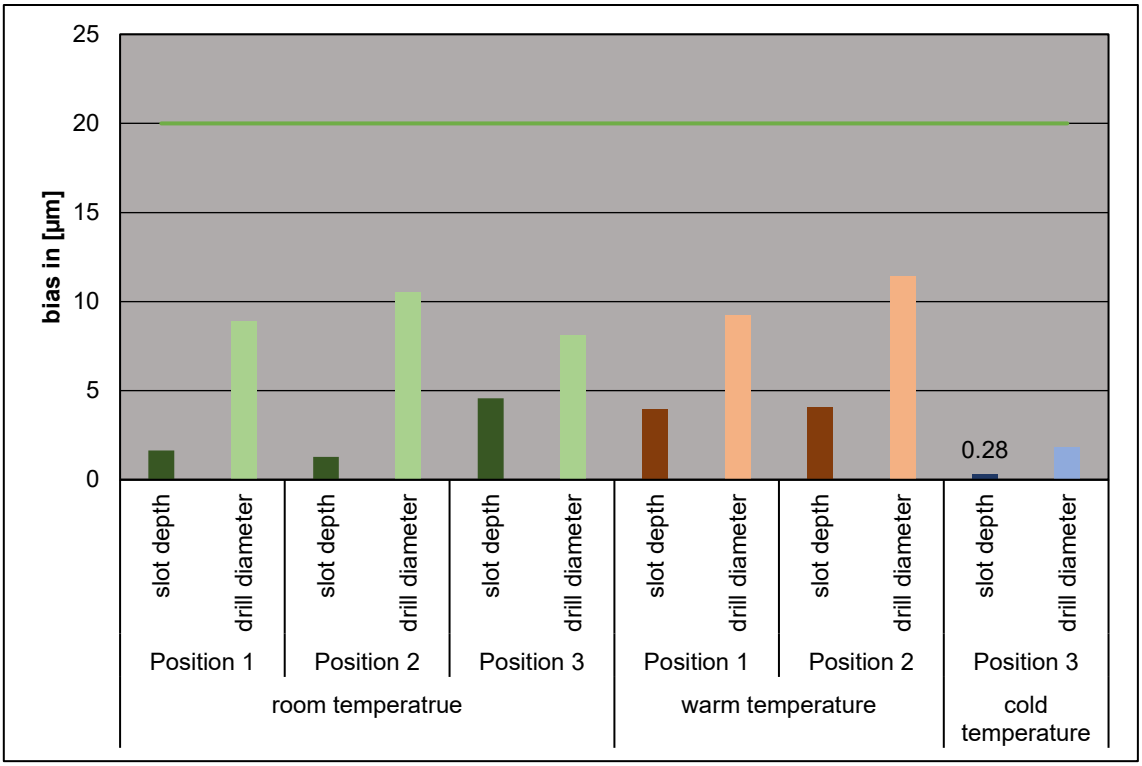

Figure 70 Overview of the results for the evaluation of thermal length changes under space conditions.

The evaluation shows that all measurement series are below the 20 µm limit. As already with the results under atmospheric conditions, the results for the drilling consistently achieve less good results. The deviations for the warm and cold results refer to the theoretical length extensions. The calculated deviations and the standard deviations for the depth of the pocket are listed in Table 16. The values for the drilling are given in Table 17.

Table 16 Calculated bias in µm for the linear thermal expansions of the depth of the pocket under space conditions.

	T120		T-33
	Position 1	**Position 2**	**Position 3**
bias	3.97	4.07	0.28
deviation	2.06	3.90	1.24

Table 17 Calculated bias in µm for the linear thermal expansions of the 6 mm hole under space conditions.

	T120		T-33
	Position 1	**Position 2**	**Position 3**
bias	9.24	11.41	1.80
deviation	3.17	7.29	5.70

With the variations described in Table 15 due to the temperature difference, the results from Table 16 and Table 17 change only minimally, by the difference given in Table 15. Even with an increase in the deviations calculated in the experiments, all measurement series are still below the 20 µm limit. This demonstrated that the evaluation of linear thermal expansion under space conditions is possible for the metallic test specimen and that a meaningful evaluation is feasible with the aid of the 3D scanner. This applies to measurements consisting of only a single view.

The next step is the evaluation of the tests that were created with the help of the rotation manipulator. For this purpose, a series of measurements was created,

consisting of a total of 20 measurements. Each measurement records the component under space conditions from five different views. The results of the evaluation are demonstrated in Figure 70.

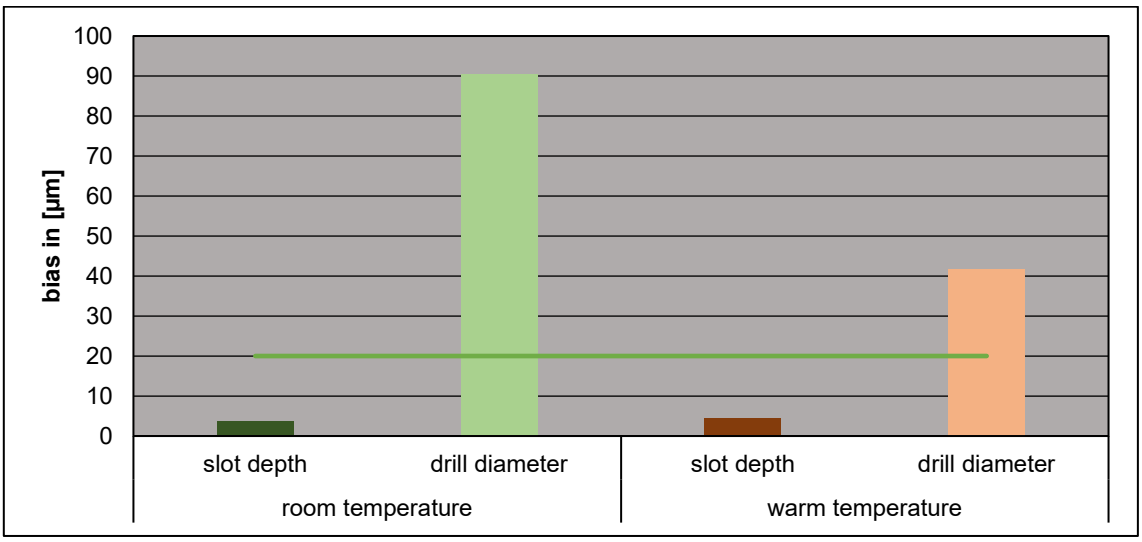

Figure 71 Evaluation of linear thermal expansions under space conditions based on rotational measurements.

The results for the turntable measurements indicate that the depth of the pocket could be evaluated without any visible influence of the glass pane. The results for the bore, on the other hand, showed enormous deviations. During the test series, the optical axis of the camera (Z-axis) ran in the same direction as the depth of the pocket. The diagram in Figure 71 illustrates the simplified test setup of the test series.

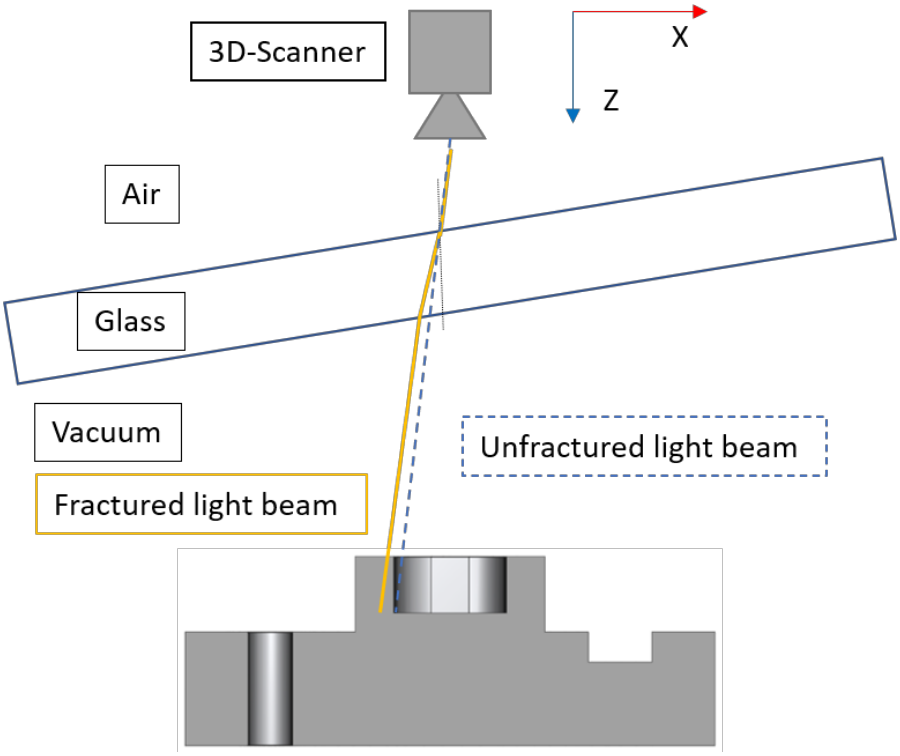

Figure 72 Sketched representation of the ray path in the XZ plane.

In the example shown, a point on the lower surface of the pocket is to be measured. Due to the experimental setup, the displacement through the glass pane has an effect in the X and Y directions. This is shown by the yellow beam for the X direction. The refraction of the beam takes place according to the optical laws of Snellius [Tip-19]. In the example shown, no displacement in Z takes place. The measurement of the depth of the pocket corresponds to a length measurement in the Z direction, which is only minimally changed. Thus, the depth of the pocket can be evaluated using the rotary table without any influence of the glass pane becoming apparent. The evaluation of the bore is a measurement of the diameter, which is based on points that are displaced by the glass pane. This results in strong deviations for the bore.

5.2.5 Conclusion for the results on tactile measured test specimen

In this chapter, the validation of the results of the normalized test specimens was successfully performed on the aluminum test specimen. The outcomes shown here are all below the 20 µm limit, and it was demonstrated that the position of the component has a statistically significant effect on the accuracy of the scanner. This made it necessary to always verify at least two component positions under space conditions whenever possible. For the tests inside the vacuum chamber, it was proven that both glass panes had the same effect on the measurement results. In addition, linear thermal expansion was evaluated under space conditions. All demonstrated results on the aluminum specimen achieved results below the 20 µm limit. Furthermore, it was shown that rotational measurements through a glass pane are possible, provided that the length to be evaluated is only in the same direction as the optical axis of the scanner.

5.3 Results on satellite components

This chapter presents the results for the evaluation of the tested satellite components. The tested components are shown in Figure 72. The components have already been described in chapter 4.2.

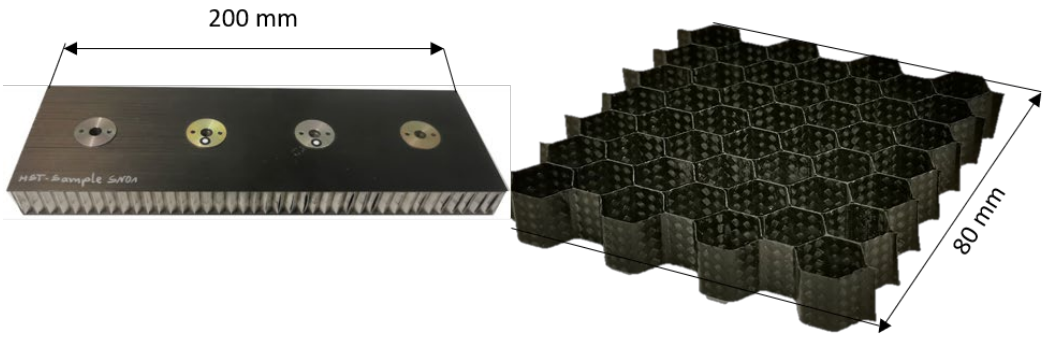

Figure 73 Satellite components. Left: Composite component. Right: Carbonfiber Honeycomb structure.

For these components, the evaluation methods are first described and validated, and then the respective measurement series are presented. We will start with the CFRP honeycomb structure and then demonstrate the results for the composite component.

5.3.1 CFRP honeycomb structure

For this component, the thermal expansions in all spatial directions are of interest to the manufacturer. The investigated component sample has the following dimensions 80 x 80 x 17 mm. The distance within one honeycomb between two opposite sides is about 10.2 mm. In the case of this component, the manufacturer was informed from the outset that an evaluation based on a 3D scan was more than unlikely. This is due to the surface properties of the CFRP honeycombs, which reflect in different directions. In addition, as much surface area of a honeycomb as possible would be necessary for an evaluation, but at a certain point, the surfaces are obscured by surfaces of the surrounding honeycombs. Due to these intersections, a repeatable evaluation is difficult simply because of the geometry. Thus, this component is a worst-case scenario due to the material on the one hand and the geometry on the other. In order to establish a comparison with the gauge block, which is also considered a worst-case scenario, a simple scale of 1-10 is to be introduced. 1 corresponds to the test sphere, 5 to the aluminum test specimen, 8 to the gauge block, and 10 to the CFRP honeycomb structure. A scan of the honeycomb structure is demonstrated in Figure 73.

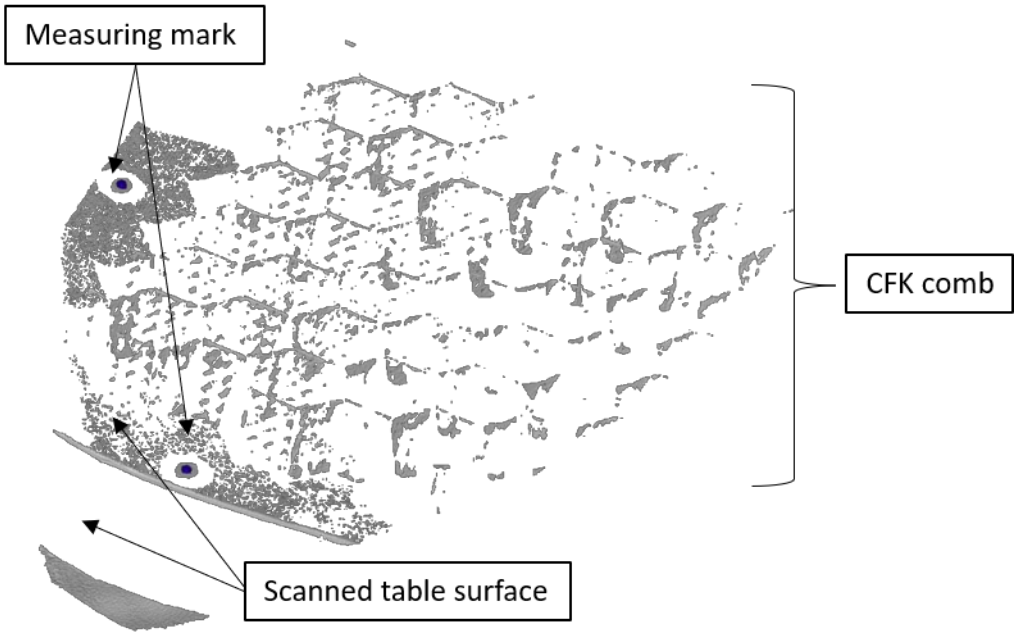

Figure 74 Scan of the CFRP honeycomb structure

It is clearly visible that only a very small area is available for evaluation. The results of the evaluation were insufficient. For this reason, the results were not presented.

An evaluation for the expansion by means of a 3D scan can also not be carried out since the expansions of the component are simply too small. According to the manufacturer, at a temperature difference of 120°C and an initial length of 80 mm, the CFRP honeycombs expand by only 3 µm with an expansion coefficient of $0.3 * 10^{-6}\ \frac{1}{K}$. This assumes that the total length of the specimen can be evaluated. However, since the total length of 80 mm was not successfully evaluated; the only option left is to check a single honeycomb. The extension of a single honeycomb with a width of 10.2 mm is only 0.4 µm. This theoretical expansion is not possible with the help of the 3D scanner. Even with the 3 µm for the entire length of the component, an evaluation would be questionable because the surface of the component is difficult to scan.

5.3.2 Composite component

For the composite part, a smaller test part was first examined, which can be seen in Figure 74. Since the part has only one rivet, a direct evaluation of the rivet spacing is not possible, but the feasibility of analyzing the rivets, in general, was investigated.

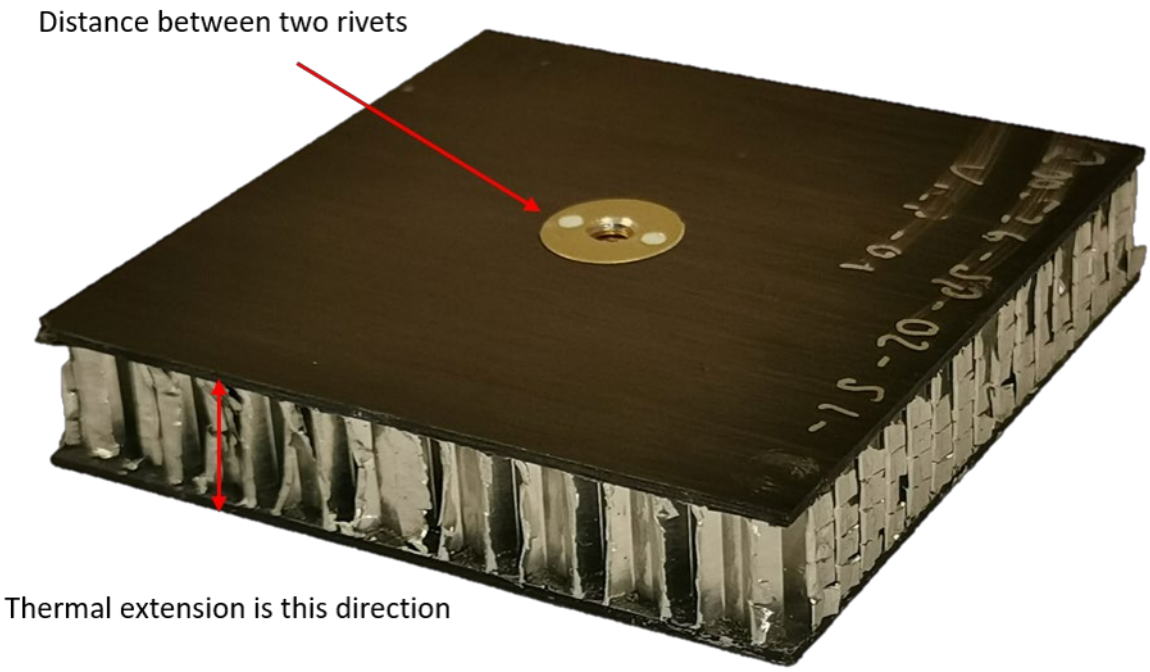

Figure 75 Small composite panel of the company Invent GmbH

The component has a size of 80 x 80 x 17 mm. The black plates are made of a CFRP material. The aim of this initial study was to investigate whether the component could be evaluated using a 3D-Scanner.

This component is also difficult for 3D scanning. The reason for this is the strong contrast between the dark CFRP plates and the metallic (light) aluminum fins. A direct scan of both surfaces with a combined exposure time did not produce positive results, making the measurement of the thermal expansion of the aluminum fins extremely difficult. For the evaluation of the expansion of the aluminum lamellae, an attempt was

made to scan the lamellae themselves and then to evaluate them using vectors within InspectPlus to calculate the length. Figure 75 shows the principle of the measurement. This was tested at three different locations.

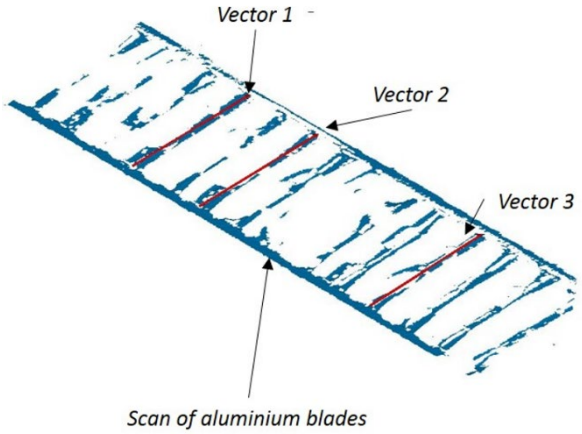

Figure 76 Illustration of the evaluation method based on vectors for the aluminum lamellae.

For each location, 20 vectors were generated and evaluated. The plot in Figure 76 demonstrates the calculated mean values over the 20 measurements and the standard deviation. Table 18 lists the measured values.

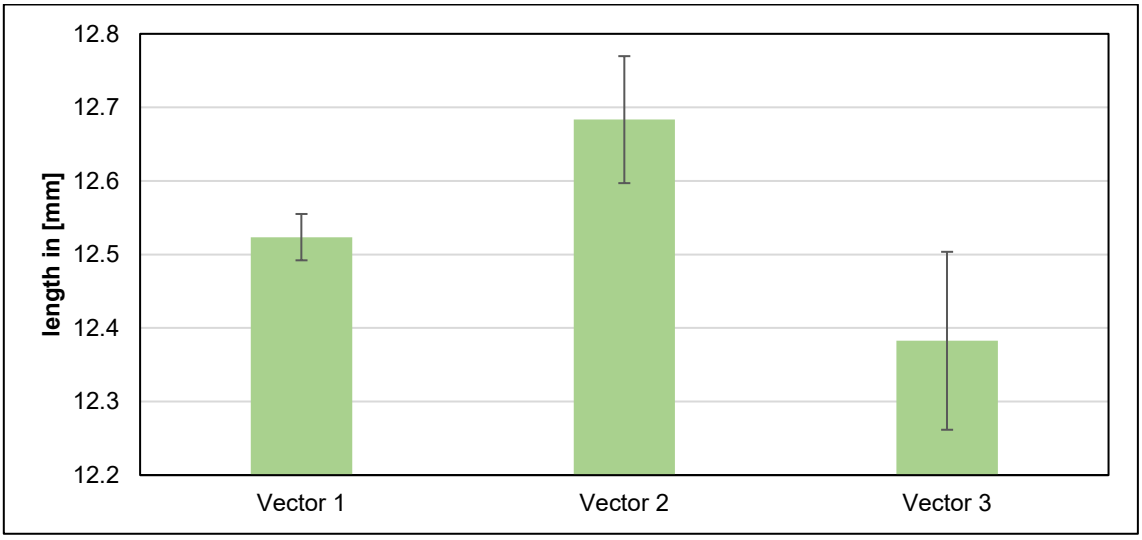

Figure 77 Evaluation of the created vectors for the aluminum panel

Table 18 Comparison of the measured lengths of the three vectors for the aluminum panel.

parameter	Vector 1	Vector 2	Vector 3
measured length	12.524	12.683	12.383
standard deviation	0.032	0.086	0.121

The evaluation shows that this method is unsuitable for a meaningful measurement. The individual vectors have a standard deviation that is higher than the determined accuracy of the scanner. In addition, the difference between the three vectors of up to 0.3 mm is also clearly too high. Therefore, the expansion of the lamellae cannot be evaluated for the time being with the help of the 3D scanner.

An evaluation procedure was also tested for the spacing of the rivets. For this purpose, a circle was generated in InsepctPlus based on the recorded rivet area and then evaluated. Figure 77 illustrates the evaluation within InspectPlus. The center of the created circle can used so that the distance between the rivets can be measured for the large test specimen.

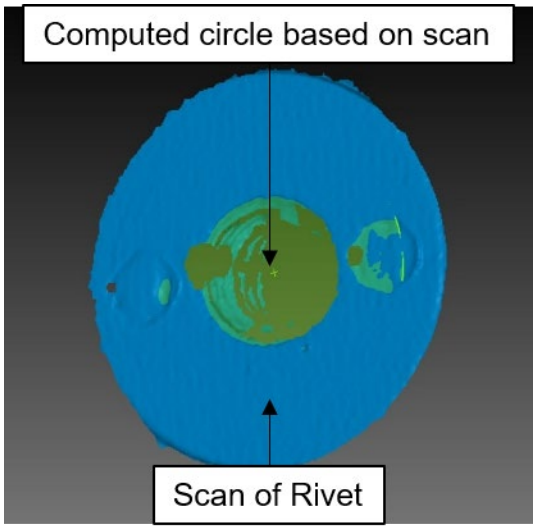

Figure 78 Evaluation of the rivet within InspectPlus.

In principle, it must be explicitly ensured here that the underlying point cloud is not cut in the area of the rivet, as otherwise, the generated circles may show great differences. This diameter evaluation based on the rivet area was performed for 10 measurements at 20 °C and at 120°C. The results of the evaluation can be seen in Table 19. The material of the rivet is aluminum and thus uses the same coefficient of expansion as the previously tested aluminum test specimen.

Table 19 Comparison of the evaluated rivet diameters at 20°C and 120°C. All values in mm

parameter	target value	actual value	bias	standard deviation
rivet diameter 20°C	unknown	9.949	---	0.004
rivet diameter 120°C	9.971	9.954	0.017	0.006

The evaluation shows a deviation of 17 µm, which is just below the 20 µm limit. However, based on this evaluation, an attempt can basically be made to determine and evaluate the distance between the rivets.

For this purpose, the large composite panel was first measured under atmospheric conditions. For this purpose, measurement series were created from two views. For the evaluation of the rivet spacing, a vector was generated between the two rivets. Figure 26 shows a sample measurement of the distance. The result of the evaluation is demonstrated in Figure 78.

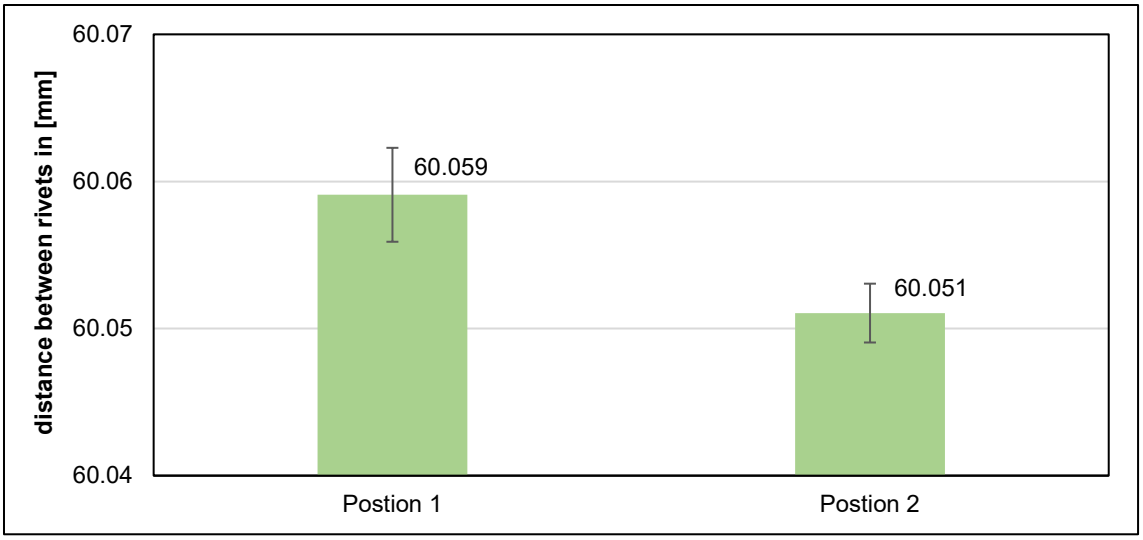

Figure 79 Plot of measured rivet spacing for the large composite panel under atmospheric conditions.

The evaluation shows that the difference between the two component positions is 9 µm. This difference could already be determined in the measurement series for the aluminum test specimen. The actual distance between the rivets is unknown to the author of this thesis, which is why no representation of the deviation can be made.

For the representation of the linear thermal expansions, the distance between the rivets must first be considered. The schematic diagram in Figure 82, which shows only a section of the component, is used for this purpose.

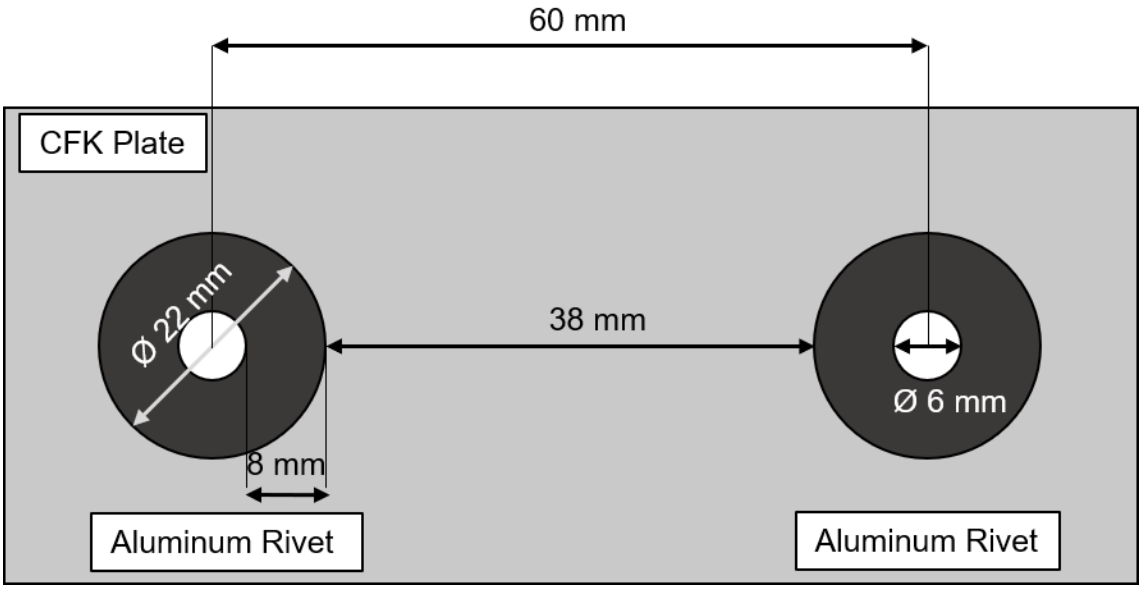

Figure 80 Schematic representation of the rivet spacing measurement from the top view.

The numerical values shown in Figure 76 are measured values, some of which originate from the previous 3D measurements or were obtained with a caliper gauge. The distance of approx. 60 mm is not a simple length of a material that expands linearly with the increase in temperature. Rather, it is the case that two metallic inserts, made of aluminum, are enclosed by a CFRP material. The inserts have a diameter of 22 mm on the upper side of the panel, each with a 6 mm hole. It follows that out of 60 mm of

total distance, 16 mm is made of the aluminum material, 38 mm is made of the carbon fiber material, and the remaining 6 mm corresponds to the hole diameter. The theoretical expansions of the respective sections are listed in Table 20. A temperature difference of 115 °C was used for the calculation, the CFRP material has an expansion coefficient of $0.3 * 10^{-6} \frac{1}{K}$[4] and aluminum of $24.7 * 10^{-6} {}^{1}/_{K}$.

Table 20 Theoretical expansions for the respective section of the panel from Figure 79.

Material	theoretical distance in mm	linear thermal length expansion in µm
Aluminum	16	44.1
CFK	38	1.3

Table 20 demonstrates that there are great differences in the expansions between the materials so that it can be assumed that the length change of the rivets does not take place completely but is prevented by the CFRP sheet. As a result, it will not be easy to predict a theoretical expansion. The measured distances at 20°C and 135°C are presented in Figure 80. For this series of measurements, only one component position could be checked since it was only possible to measure two of the four rivets in one view from one position. From other positions, the rivets were always only partially included on the scan.

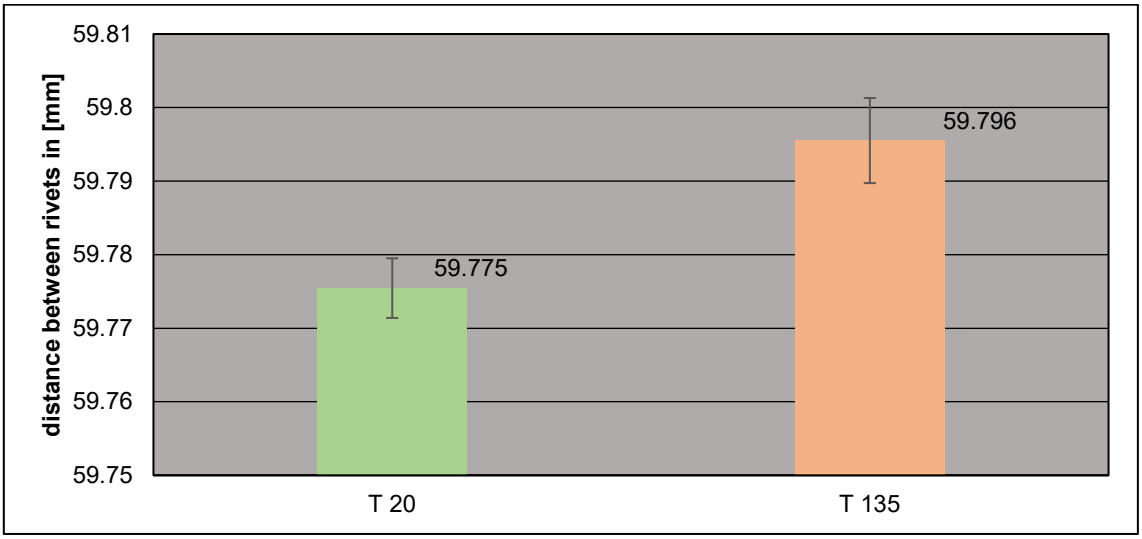

Figure 81 Plot of measured rivet spacing for the large composite panel under space conditions.

The evaluation reveals directly that the measured distance at room temperature differs enormously from the distance under atmospheric conditions. This again illustrates the influence of the component position. The difference between the two series of measurements is 20 µm. Due to the previously described problem, no direct comparison can be attempted here. However, the following points can be ruled out based on this result.

The difference between the scans is too large to be a pure statistical variation, so it can be stated that there is a change due to the heating of the component. If the rivets were allowed to expand freely, the theoretical expansion would be a length of 44 µm.

[4] Specifications according to manufacturer

With a measured change of 20 µm, at least part of the distance was measured and is thus still in the approximate vicinity of the theoretical expansion. However, a deviation of 24 µm is very high and did not occur in previous measurement series, but this is not a criterion for exclusion. If it is considered that the CFRP sheet prevents the expansion of the rivets, it seems logical to be able to detect only part of the length change. For the evaluation of the rivet spacing, however, this means that it is not possible to directly determine the significance of the evaluation without further ado.

With the aid of a finite element method (FEM for short), the expansion of the rivets could be determined theoretically. However, this presupposes that all material parameters and the ambient conditions must be known. In the context of this work, such a FEM was not carried out. The reason for this is that FEM simulations are extremely complex and time-consuming. For meaningful FEM calculations, the underlying calculation system must be validated using simple models or simulations. On this basis, the results of complex systems, such as that of the composite component, can be used.

5.3.3 Intermediate conclusion Satellite components

In the context of this chapter, the results for the measurement of satellite components were presented. For the CFRP honeycomb structure, no successful evaluation could be performed because the combination of the material and the geometry of the component makes it extremely difficult to measure using a 3D scanner even under atmospheric conditions. These difficulties are exponentially increased by the limited options within the vacuum chamber so that no measurement was possible here anymore. In addition, the linear thermal expansions at the laboratory scale used are too small to be captured by a 3D scanner.

Results could be obtained for the composite part, but these findings cannot be confirmed directly. Due to the different material properties of the materials used, the expansion of the measured rivets is not directly evident. The presented results seem to be in a logical range, for validation of the data a FEM calculation of the test setup can probably be used.

The evaluation of the two components shows the limitations of the system. The previously obtained results on metallic materials, which were consistently positive, cannot be directly repeated for the panel elements.

5.4 Results for the 500-measuring field

It is possible to exchange the measuring volumes for the Comet L3D 5M 3D scanner. The previous results were all obtained with the 100-measuring field. In this subchapter, results obtained with the 500-measuring field are presented. It is expected that the measured values and accuracies of the 500-measuring field will be higher. Due to the larger point spacing between the pixels, the scans will be less well resolved, which will

also decrease the accuracy of the system. Nevertheless, there is the question of how big this difference is and to what extent the results achieved so far or the tested parameters influence the scans of the 500-measuring field.

The results will start with a review of the evaluation procedure in InspectPlus. This is followed by the determination of the accuracy limit on the 40 mm gauge block and on the aluminum test specimen. The test specimen is also used to test how strongly the component position influences the accuracy. The results for the measurement of the linear thermal expansion are then presented.

5.4.1 Evaluation method

The same methodology that was used for the 100-measuring field was used to check the evaluation procedure. The graphical evaluation of the 50 length measurements can be seen in Figure 81.

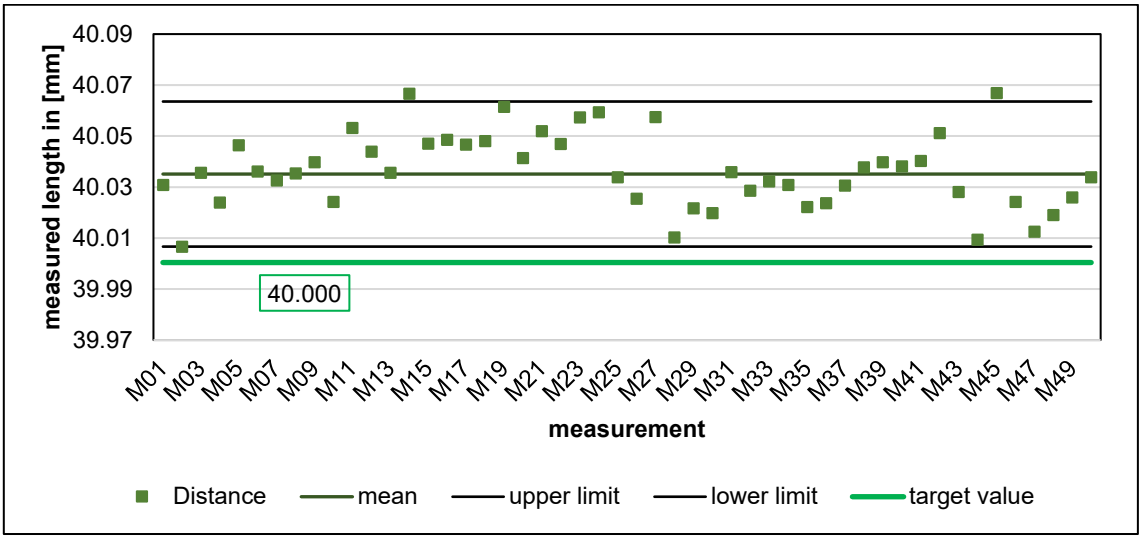

Figure 82 Evaluation of the repeatability in InspectPlus for a point cloud of the 500-measuring field.

Figure 81 clearly shows that the standard deviations within InspectPlus are significantly higher than before. The limits shown symbolize the standard deviation for 95% limit, which is ±26 µm. For comparison, the value for the 100-measuring field was ±0.6 µm. ±26 µm is an amount that cannot be ignored for further evaluations and must be considered for the evaluation of the measurements. An increase in the value was expected, but the evaluated amount is above these expectations. A reason for the height of the standard deviation can be the size of the object or the size difference between objects and used measuring volume. For the evaluation of the gauge block with the help of a 3D scanner, its side surfaces are important. These side surfaces have a width of 10 mm, which corresponds to a relative length of 4% in the Z direction (250 mm) of the 500-measuring volume. For the 100- measuring field, the length of 10 mm corresponds to a relative length of 16.5% in the Z direction. For the other spatial directions, the relative lengths are even smaller. Since in the context of this work the

comparison between the different result series is aimed at, no evaluation of a larger measuring body is carried out.

5.4.2 Determining the accuracy limit at 40 mm gauge block

For the determination of the accuracy limit, the best-practice parameters for the 500-measuring field were not worked out; instead, a comparative measurement was carried out with the parameters obtained. The test setup is shown in Figure 32, as for the 100-measuring field. The graphical evaluation of the measurement series is presented in Figure 82.

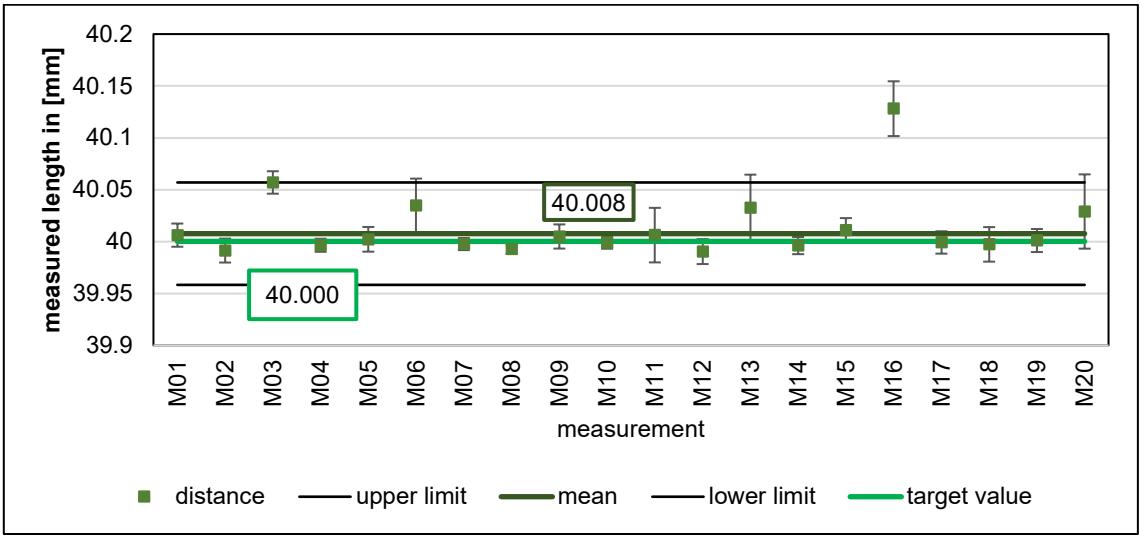

Figure 83 Graphical evaluation of the measurement series for the 40 mm gauge block based on scans of the 500-measuring field

Figure 82 indicates that the measured deviation is 8 µm, which is an extremely positive result considering the previously determined standard deviation of ±26 µm. The variation within the individual measurements (green squares) amounts to ±14 µm on average. The standard deviation of the entire series of measurements, represented by the upper and lower limits, is approximately ±36 µm.

The result shows that, in principle, even a small object such as the gauge block can be measured relatively accurately, but the standard deviations are significantly higher than before. The comparison of the calculated deviation and standard deviation for the different measurement fields can be seen in Figure 83.

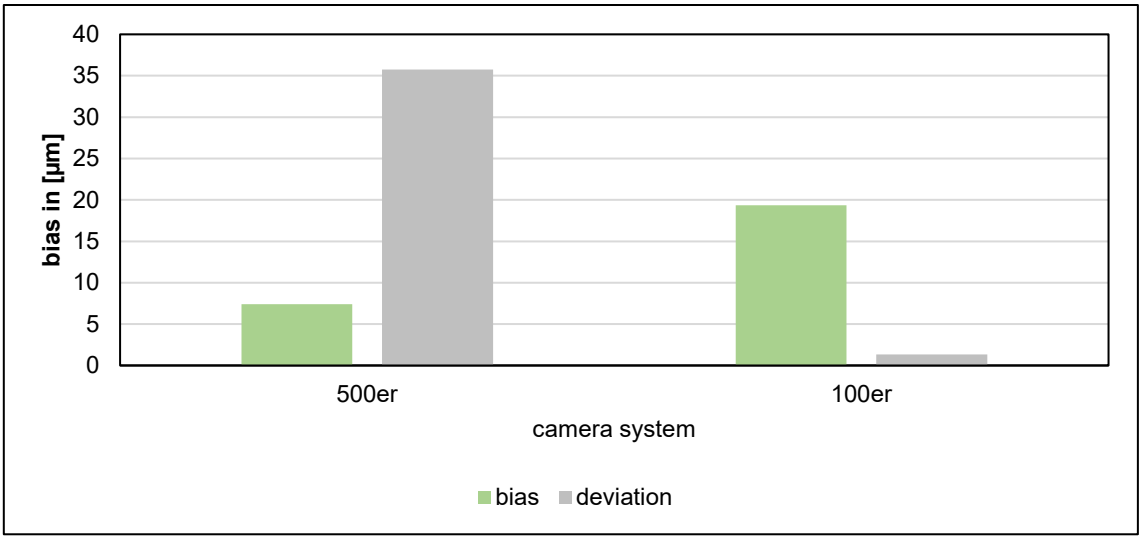

Figure 84 Comparison of the measurement series for the 40 mm gauge block based on the different measurement fields.

The comparison from Figure 83 shows that the measurement series of the 500-measuring field has a lower deviation, but the standard deviation is significantly higher. A direct reason for the lower deviation of the 500-measuring field cannot be found based on the data. However, the measured values of the 500-measuring field also fluctuate strongly, so the deviation achieved must be viewed critically. The accuracy limit of 20 µm is adjusted for the continuing results of the 500-measuring field. The limit for the 500-measuring field should be 45 µm for the remaining measurement series. This means that the results obtained in Figure 82 and Figure 83 would still be below this limit, even with maximum utilization of the standard deviation.

5.4.3 Validation on the aluminum test specimen

For the evaluation of the aluminum test specimen, the object was recorded and evaluated from two different positions. The test setup corresponds to the setup shown in Figure 35. During the measurement of the component, no position could be found in which it was possible to evaluate the drill holes. For this reason, the following evaluations only cover the depth of the pocket. The results of the measurement series are shown in Figure 84.

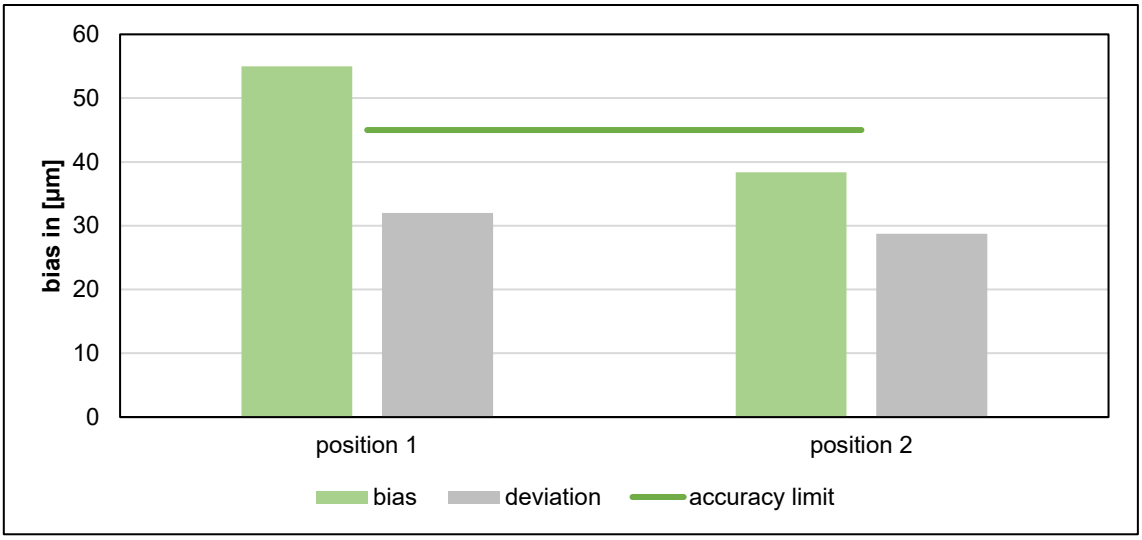

Figure 85 Comparison of the results for the aluminum test block from different component positions for the 500-measuring field.

The comparison from Figure 84 demonstrates that the calculated deviation for position 1 is above the 45 µm limit. Including the standard deviation, the results for position 2 are also higher than the 45 µm limit, and the deviation for position 1 is even larger. Considering the good results for the gauge block, the results for the aluminum specimen are in strong contrast. One reason for the large difference may be the number of scans. The gauge block was measured from two views, and the measurement series for the depth of the pocket is based on only a single view. Furthermore, no suitable view was found for the holes, so the size of the form elements to be measured seems to play a decisive role.

In order to determine whether the weaker results for the aluminum body resulted from the number of scans, a series of measurements were performed in which the object was measured from 3 views. The results of this test series can be seen in comparison to the single view results in Figure 85

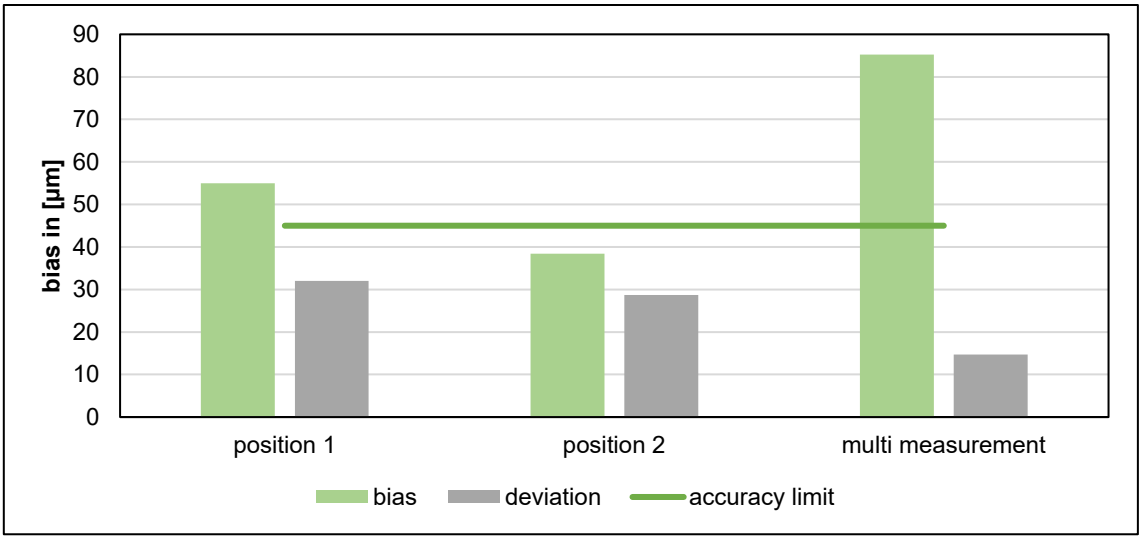

Figure 86 Comparison between single view measurements and measurements from multiple views.

Figure 85 indicates that the number of scans did not improve the result, so it can be assumed that the shape element size is the decisive factor.

The next step is the evaluation of the linear thermal expansions under space conditions. The measurements with the 500-measuring field did not yield the expected effect of having much more measuring volume inside the chamber. The reason for this was the displacement of the point cloud due to the installed glass panes. The effect of the bulge was much stronger for the 500-measuring field and can be seen in Figure 86.

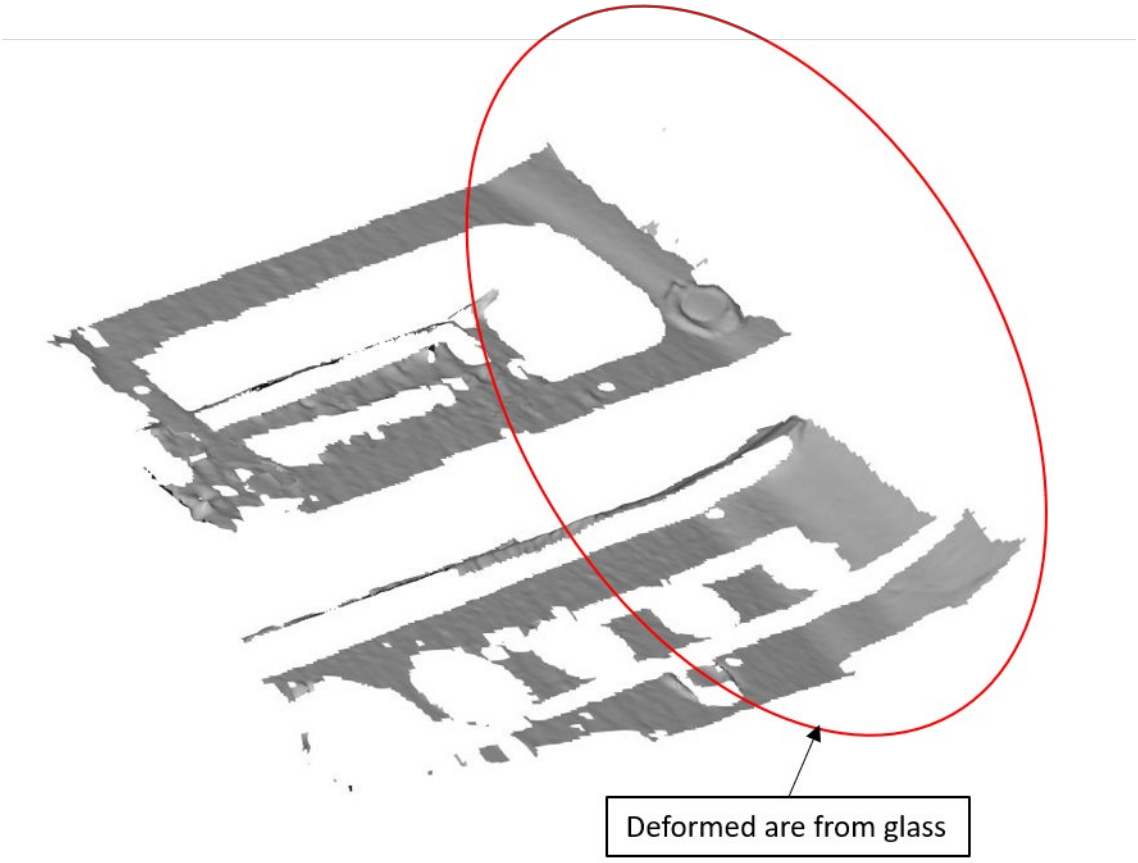

Figure 87 Deformation based on a scan through glass with the 500-measuring field.

This effect also made it impossible to perform a rotation measurement since the displacements then also affected relevant areas for evaluating the depth of the pocket. For this reason, measurements were made based on a single view. The result for the evaluation of the thermal expansion in length is demonstrated in Figure 87. The test setup and the parameters used are the same as for the measurement series of the 100-measuring field.

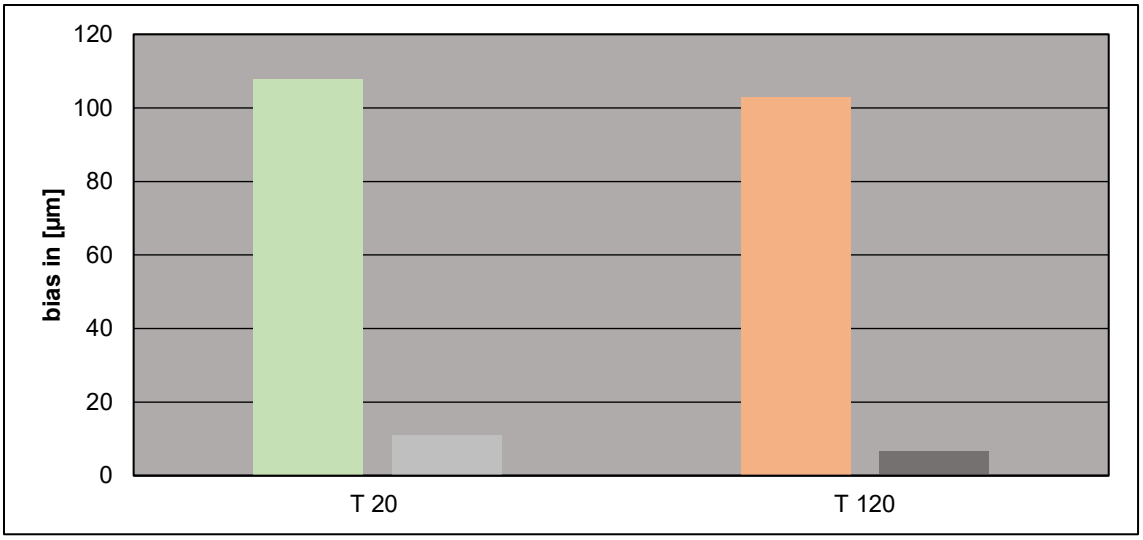

Figure 88 Evaluation of linear thermal expansions under space conditions for the depth of the pocket.

As expected, based on the results under atmospheric conditions, the results under space conditions fall in approximately the same spectrum. The deviation from the nominal value is again higher for both series of measurements, but the standard deviations are lower. If the measured value of the room temperature is used for the theoretical linear expansion, the measurement series at 120 °C achieves significantly better results. The representation of these numerical values is listed in Table 21.

Table 21 Representation of the relative theoretical linear thermal expansions

	Base value	Theoretical linear thermal length extension	measured bias in µm
target value	7.627	7.645	102
measured value	7.734	7.752	-5

The representation of these relative values shows that the thermal expansions are basically measured correctly with a deviation of 5 µm, only in relation to the actual value of the pocket, the deviation is too high. What is striking about these measurement series is the very low standard deviation compared to the previous results. One reason for this could be the selected component position.

5.4.4 Intermediate conclusion 500-measuring field results

The test series for the 500-measuring field delivered mixed results. As was to be expected, due to the increased point spacing, the accuracy of the measuring field is less good than that of the 100-measuring field. For this reason, the accuracy limit was raised from 20 µm to 45 µm. A striking aspect is the standard deviation of up to ±26 µm obtained for these measurement series, which is significantly higher than for the 100-measuring field. However, the larger measuring volume covers about four times the area. The test series showed that this effect had no positive effect for the measurements behind glass. The displacements caused by the glass bulge were much greater, so that the available field of view or scanning area of the scanner remained the same. Due to the relative size of the object to the measurement volume of the 500-measuring field, the holes of the aluminum test specimen could not be successfully

measured. The results for the depth of the pocket demonstrated large deviations relative to the 45 µm accuracy limit. Basically, the test series showed that the 500-measuring field in combination with the installed glass panes and the relatively small objects is not suitable for the evaluation of components under space conditions. This fact must be checked again with larger components, but more space must be available in the vacuum chamber for this purpose.

6 Conclusion

The results obtained and their significance for the project "Optical metrology under space conditions" are summarized in this chapter. The work was concerned with the development and testing of a new evaluation method of the linear thermal expansions of components under space conditions with the help of a 3D scanner. For the analysis of the objects, which are located inside a vacuum chamber, the scanner must measure the components through an additional glass pane. At the beginning of the present work, the following requirements and questions were listed which, are briefly repeated here.

Measuring method

- The evaluation should be fast
- The evaluation must be able to detect linear thermal expansions of components
- The evaluation should have the largest possible measurement volume
- The evaluation should have a high accuracy and repeatability
- The evaluation must work for as many surfaces as possible.
- The evaluation must work through an additional glass pane
- How accurately can a stripe light scanner scan a reflective object?
- Which environmental parameters or setting options affect the result of the 3D scan the most?
- Will a ray tracing method be necessary to perform three-dimensional measurements behind a glass pane?

By the obtained results of this work, the requirements and questions can be fulfilled and/or answered.

First, the general accuracy limit of the 3D scanner used was determined based on standardized test specimens. The influence of various parameters on the accuracy of the scanner was examined. The object examined was a 40 mm gauge block, which can be described as a worst-case scenario for the 3D scan due to its reflective surface. The results showed that the accuracy limit of the utilized scanner is 20 µm. Of the parameters studied, only the acquisition angle between the object and the scanner exerts a statistically significant effect on the accuracy of the measurements. These results are consistent with the results of the work of S. Gerbino et al. [Ger-16] and F. Li et al. [Li-17]. Gerbino et al. [Ger-16] also concluded that only the angle of exposure has a significant effect on the laser line scanner. The effect of the ambient exposure

and the camera filter were also statistically insignificant [Ger-16]. For ambient exposure, this result was additionally confirmed by F. Li et al. [Li-17]. In relation to the presented work, especially the fact that the exposure time and the ambient exposure do not exert a significant influence on the accuracy are important. Regarding the exposure time, it always depends on the material of the object to be measured and thus, must be set differently from component to component. With different components, this influence would always have to be determined so that a strong influence of the exposure time on the accuracy would be disadvantageous. The interior of the vacuum chamber is not well illuminated by the ambient lighting, but since this parameter has no statistically significant effect, this circumstance did not have to be changed for the 3D measurements. This answers the questions about the accuracy of reflective surfaces and to what extent the adjustable parameters influence the scan.

The effect of the additional glass pane was also investigated using the 40 mm gauge block. The results showed that changing the angle of the glass pane by 1° increases or changes the systematic deviation by about 2.5 µm due to the change in the beam path. This result is only valid for 3D measurements based on at least two views. For scans consisting of only a single view, no change could be detected. In addition to the increase in systematic deviation, it was also found that the geometry of the point cloud no longer matched the original geometry of the scanned component. The point clouds of the 40 mm gauge block, which were acquired by an additional glass pane with a large angle change (> 45°), tended to have more of a trapezoidal shape than a cuboidal shape. Using the measurements of the 40 mm gauge block, an adapted ray tracing approach by [Yam-04] was tested. The results of the approach did not show positive results because the reconstructed ray paths of the scanner were skewed to each other. The reason for these results could be insufficient or inappropriate and deviating assumptions to reality. For the measurement of the component under space conditions inside the vacuum chamber, the approach of single view measurement was followed.

For this approach, it was necessary to determine beforehand whether the position between the scanner and the component exerted an influence on the results of the 3D scan. For all measurement series, results were obtained which were below the 20 µm limit. This involved the evaluation of two different shape elements, the depth of the pocket and the 6 mm hole. The results showed that the position of the component or the scanner had an influence on the results. For this reason, an attempt was always made to test at least two views for the subsequent series of measurements. On closer consideration, this fact is an extension of the results of the angle of exposure. By changing the position of the component or the scanner, the reflection behavior of the light on the object surface changes, whereby the scanner receives different information depending on the position for the respective surface. The change of the pickup angle corresponds to the same situation in the end because the position of the object to the scanner changes.

Based on these results, a series of tests were conducted to determine the linear thermal expansion of the aluminum test specimen under space conditions. Initial tests using the 40 mm gauge block already showed that the expansions could be recorded

under atmospheric conditions. The results of all tests under space conditions based on the aluminum test specimen are shown in Figure 88.

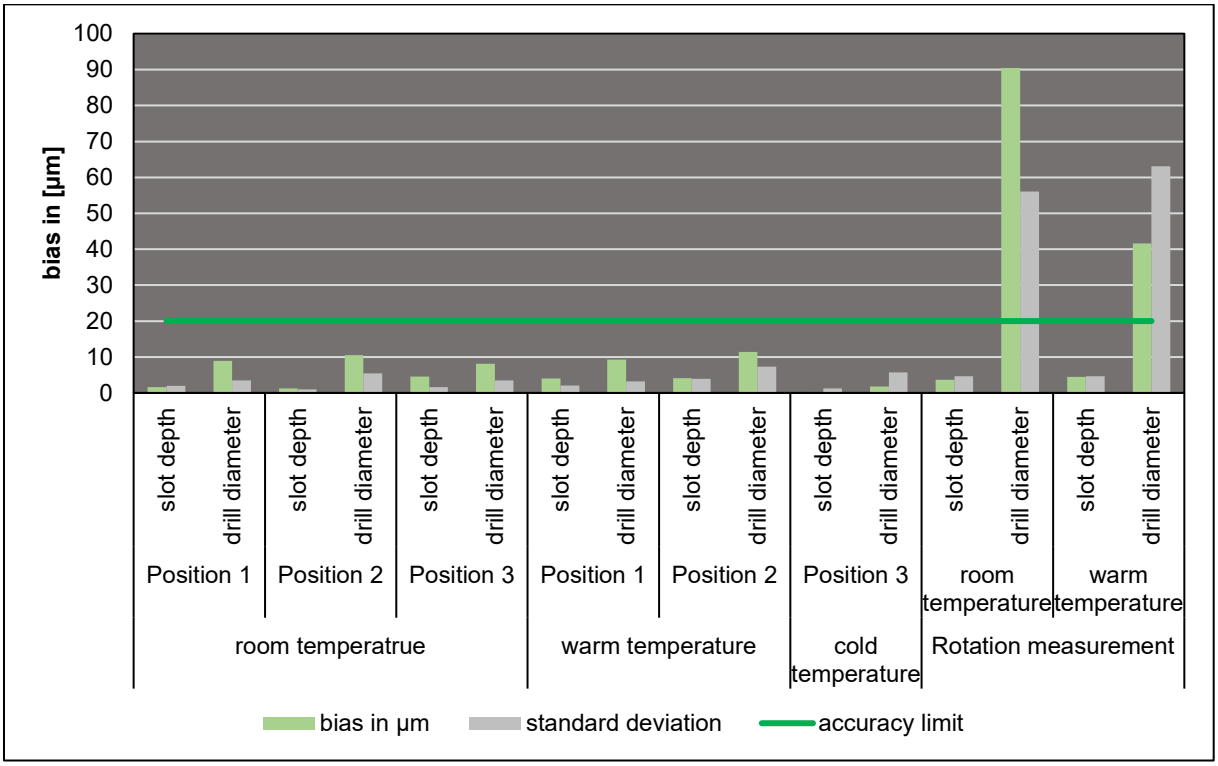

Figure 89 Total overview of all obtained results under space conditions for the aluminum test body.

From the results, the measurements based on a single view are consistently below the 20 µm limit, with many of the results even showing a deviation smaller than 10 µm. Coupled with the low standard deviations of the results, it was shown that the evaluation method has high accuracy and repeatability. The results of the rotational measurements confirm the result of Hadjimichael [Had-10] that the optical displacements are smallest in the direction of the optical axis of the scanner. This can be seen from the depth of the pocket, which in the experimental setup used was in the same direction as the optical axis of the scanner. In the specific case of the presented work, no difference between these measurement series and the single view measurements can be observed. The measurement series for the drill hole, on the other hand, is strongly influenced by the optical displacement of the glass pane. For this reason, the deviation in these results is also extremely high.

In summary, these results demonstrated that the linear thermal expansions under space conditions can be evaluated using a 3D scanner for a metallic body. It was also demonstrated that the evaluation procedure works through an additional glass pane without having to use a ray tracing approach.

The series of tests for the two satellite components yielded mixed results. The CFRP honeycomb structure clearly showed where the limitations of the evaluation method lie in two ways. First, carbon fiber components are extremely difficult to capture using a 3D scanner. The reason for this is the interweaving of the individual fibers as well as the reflectivity of the material. The other limit, which the honeycomb structure revealed,

is that the vacuum chamber used cannot be made sufficiently hot or cold. The low coefficient of expansion of the carbon fiber material allows the components to become only minimally larger or smaller under the conditions used, making evaluation using the 3D scanner impossible. The results for the composite component show that the data obtained cannot be evaluated without further considerations and assumptions. In principle, the series of measurements demonstrated that the metallic part of the composite component can be evaluated. However, the data cannot be validated without, for example, a FEM. Based on these results, the requirement that as many surfaces as possible should work is only partially fulfilled. The evaluation procedure remains subject to the already existing restrictions of the 3D scanner so that e.g., transparent, or partially transparent objects cannot be captured. In addition, there are the restrictions added by the limits of the laboratory scale, including the already mentioned carbon fiber materials and other special high-temperature materials. For concrete applications from the aerospace industry, metallic components, or composite components, in which the metallic part is to be investigated, are thus considered.

The last open points of the list of requirements are the demand for the speed of the evaluation procedure as well as a measuring volume as large as possible. Considering the test procedures otherwise used in aerospace, which can take days in some cases, the developed procedure is fast. The biggest time factor of the procedure is the generation of the vacuum and the time needed to heat up or cool down the component. Cooling down the component after a heating test takes an enormous amount of time. Apart from these points, the test procedure can be carried out very quickly. A complete series of measurements can be completed in less than an hour. For this reason, the requirement for a fast evaluation procedure was successfully met.

The requirement for the measurement volume was tested based on the 500-measuring field. The results for the 500-measuring volume were mixed. The evaluation showed significantly higher standard deviations, but in some cases, achieved equivalent results to those of the 100-measuring field in terms of systematic deviation. Results based on a single view demonstrated significantly worse results even under atmospheric conditions. The hoped-for effect of being able to cover more area inside the chamber with the aid of the 500-measuring volume failed to materialize since the effect of the installed glass pane rendered the additionally covered areas unusable. It can therefore be stated that the 100 mm measuring field is a good compromise between accuracy and measuring volume. Considering the size of the laboratory scale, the choice is doubly supported since not too large components always find space inside the vacuum chamber.

Thus, all the requirements for the evaluation of linear thermal expansion under space conditions based on a 3D scan for materials, that are not considered high-temperature resistant, could be met. The elaborated method is precise and accurate to about 10 µm. Basically, the obtained results can be considered as a "proof of concept", which has been successfully provided for metallic materials. In the following and final chapter, possibilities are identified for improving the evaluation procedure.

7 Outlook

In this chapter, the potential for improvement and further tasks are to be identified. For a better overview, the individual points are listed briefly here and then described in more detail. For the evaluation procedure, there is the following potential for improvement

- Use of a newer scanner
- Upgrading the vacuum chamber
- Improvement of the rotation manipulator
- Use of a ray tracing software

Based on the results of this project, the following further work or ideas exist

- Creation of a validated FEM model
- Verification of the results for further metallic materials

All results of this work were created with the Comet L3D 5M. The stripe light scanners currently available on the market use a two-camera system in addition to the light source. An example of this would be the ATOS 5 fringe light scanner from Zeiss or GOM [Gom-21]. By using two cameras with 8 million measuring points each, the scanner can capture more surfaces with a higher resolution just from the technical starting point. Verifying the results obtained here with such a device could improve the overall accuracy of the system. For a comparison of the scanners, the following series of measurements or experiments would be used: For the analysis of the general accuracy, a series of tests would be carried out with the 40 mm gauge block as well as with the aluminum test specimen. This should be sufficient for a comparison of the accuracy achieved. It is questionable how the use of two cameras affects the effect of the glass pane since two images must now be processed for the calculation of one image point. For this reason, intensive tests would be carried out for this special issue, since the technical behavior of the ATOS 5 scanner differs fundamentally from that of the COMET. This would begin with tests to determine the influence of the glass pane on single-view scans and then investigate multiple-view scans. If the respective image coordinates by the cameras are shifted by the glass pane for a single view scan, this aspect could prove to be disadvantageous. The results for the tests through the additional glass pane determine the scope of the test under space conditions. With strongly deviating behavior of the ATOS 5 for single view scans through an additional glass pane, the feasibility for scans under space conditions is not given for the time being and a solution for this problem must be found first. The time required for this cannot be estimated at the present time.

By upgrading the vacuum chamber, the laboratory scale can be improved, especially regarding the reached temperatures. On the one hand, the temperature range could be improved by at least 100 °C by purchasing a liquid nitrogen pump. For the use of liquid nitrogen, some built-in elements such as the liquid feed-through of the chamber must also be adapted. By using different glass panes, the viewing area inside can be increased. At the same time, the use of other glasses, i.e., glasses without bulge, turns out to be difficult. Elements of vacuum chambers use standardized connection systems. The glass panes, such as the one used for the angle and distance tests, use

a different connection system than the one used for the chamber. In principle, these elements can be connected to each other, but only with the help of adapter pieces. This extends the distance from the glass pane to the inside of the chamber currently in use, which can lead to problems under certain circumstances. In principle, it would also be possible to design and purchase a completely new vacuum chamber, but this is a major economic investment that is not readily possible without additional funding.

The rotary manipulator used for this work is used without control or regulation. A possible improvement would be that the manipulator could function like the automatic turntable of the scanner. For this purpose, the manipulator must be equipped with, for example, a stepper motor instead of an electric motor. Regulation and control are then possible via a microcontroller, which is also located outside the chamber. By upgrading the turntable inside the chamber, the rotation measurements can be performed with more repeatability.

The ray tracing approach used in this work is calculated manually, so there is a large source of error here. There are full-featured software packages for ray tracing approaches or models, which calculate the complete ray path of the model. The use of such software requires know-how, which could not be acquired in the course of this work due to time constraints. The creation of the model is usually only half of the work in simulations. The usually much larger part of the work is the validation and confirmation of the model. For this reason, such a model was not used in this work. For future studies, a working ray tracing model is more than useful. For this, however, the circumstances at the vacuum chamber must be known in detail. One factor that must be evaluated is the deformation of the glass pane due to the changed temperature and the vacuum. In addition to the deformation, the initial shape of the glass pane must also be precisely known. With this information, a realistic ray tracing model of the beam path into the interior of the vacuum chamber is possible.

The further or continuing results for additional metallic materials such as steel alloys, titanium, or tungsten complement the results demonstrated so far and would serve to find further possibilities and limits of the evaluation procedure or the measurement method.

In addition to the creation of the ray tracing model, the construction of a suitable FEM model represents another complex aspect that could not be pursued within the scope of this work. As already briefly described, such a model must be verified by real experiments for meaningful results. The series of measurements carried out here can therefore be used as a basis for such a model. However, before the measured expansions obtained here can be used for this purpose, numerous factors must be precisely known. This includes, among other things, the temperature behavior inside the chamber. This aspect alone requires an enormous amount of real experimental data, which must be obtained with the aid of temperature measurements. The results presented in this work in this area are by far not sufficient and can only serve as a small introduction. In particular, the temperature behavior of the components is extremely complex with respect to temperature transfer by radiation. For a simulation, the user must know the emission values of the respective components. These values depend on the surface properties of the material as well as on the material itself and must be determined for each tested component. The time required to set up such a

model can hardly be estimated and represents a major challenge. It is also true that, especially for components made of different materials, the complexity of this simulation also increases enormously. Examples of particularly complex situations would be welded joints between two metallic materials or glued connections for carbon fiber components. Based on the simulation results, it would then be possible to confirm the real data of the experiments. However, a certain measurement error or difference between simulation and reality will still exist. But this difference should be in a relative range of 10 - 15%.

With the help of these improvements, it would be possible to extend the provided "proof of concept" and to enter the next phase of technology development. After completion of this work, the project is between the technology maturity levels [ESA-21b] TRL 3 and TRL 4. With the help of the improvements mentioned and further work in a corresponding validation phase, the technology maturity level can be raised to level 6 or 7, which corresponds to a prototype in the operational environment [ESA-21b]. On the one hand, this would provide the space industry with a new method for testing new satellite components quickly and cost-effectively at an early stage of their development. On the other hand, there is the possibility to choose this method as a middle way of quality control for large-scale space projects.

Directories

List of figures

List of tables

List of equations

References

Literature

[Bas-20]	E. Bas, Einführung in Wahrscheinlichkeitsrechnung, Statistik und Stochastische Prozesse, 2020, 1. Auflage, Springer Vieweg, https://doi.org/10.1007/978-3-658-32120-8
[Ber-13]	C. Bernal; B. de Agustina; M. M. Marín; A. M. Camacho, A. M, Performance Evaluation of Optical Scanner Based on blue LED Structured Light, 2013, Procedia Engineering Vol. 2, p 591-598, 10.1016/j.proeng.2013.08.261
[Bli-20]	K. Bliznakova, 2020, The advent of anthropomorphic three-dimensional breast phantoms for X-ray imaging. Physica Medica, 79, 145–161. doi:10.1016/j.ejmp.2020.11.025
[Bre-19]	Mats Bremer, Michael Wahl, Slawomir Kedziora (2019), Einfluss einer zusätzlichen Glasscheibe auf ein optisches 3D-Messsystem, tm – Technisches Messen, Vol. 87, Part 7-8, http://dx.doi.org/10.1515/teme-2019-0105
[DIN-90]	DIN Deutsches Institut für Normung e.V , 1990, DIN 28400-1:1990-05, Vakuumtechnik; Benennung und Definitionen; Allgemeine Benennungen
[DIN-97]	DIN Deutsches Institut für Normung e.V. 1997. DIN ISO 5725-1:1997-11, Genauigkeit (Richtigkeit und Präzision) von Meßverfahren und Meßergebnissen_- Teil_1: Allgemeine Grundlagen und Begriffe (ISO_5725-1:1994). Deutsches Institut für Normung e.V. Berlin 10.31030/7344872
[DIN-20]	DIN EN ISO 10360-13:2020-07, Geometrische Produktspezifikation_(GPS)_- Annahmeprüfung und Bestätigungsprüfung für Koordinatenmessgeräte_(KMG)_- Teil_13: Optische 3D KMG
[Fun-16]	T. Funke, M. Buscher, A. Patzphal, K. Brieß, Eigenschaften und Entwicklung von Kleinstellten, 2016, Deutscher Luft- und Raumfahrt Kongress

[Gen -11]	J.Geng, Structured-light 3D surface imaging: a tutorial, 2011, Adv. Opt. Photon. (Advances in Optics and Photonics) Vol.2, p 128 – 160, DOI: 10.1364/AOP.3.000128
[Geo-10]	A. Georgopoulos, Ch. Ioannidis, A. Valanis, Assesing the performance of structured light scanner, 2010, International Archives of Photogrammetry, Remote Sensing and Spatial Information Sciences Vol. 38 Part 5, p. 251 – 255.
[Ger-16]	S. Gerbino, D.M. Del Giudice, G. Staiano et al. On the influence of scanning factors on the laser scanner-based 3D inspection process. Int J Adv Manuf Technol 84, 1787–1799 (2016). https://doi.org/10.1007/s00170-015-7830-7
[Gue-20]	M. G. Guerra; L. de Chiffre; F. Lavecchia; L. M. Galantucci; Use of Miniature Step Gauges to Assess the Performance of 3D Optical Scanners and to Evaluate the Accuracy of a Novel Additive Manufacturing process, 2020, Sensors Vol. 3 p. 738 – 754; DOI: 10.3390/s20030738
[Gue-02]	J. Guehring, 2002, 3D-Erfassung und Objektrekonstruktion mittels Streifenprojektion, Universität Stuttgart.
[Gum-93]	International Organization for Standardization.1993. Guide to the expression of uncertainty in measurement. International Organization for Standardization. Genève
[Had-10]	T. Hadjimichael, D. Kubalak, A. Slotwinski, P. Davila, B. Eegholm, W. Eichhorn, et al. (2010). Cryogenic metrology for the James Webb Space Telescope Integrated Science Instrument Module alignment target fixtures using laser radar through a chamber window. Optical System Alignment, Tolerancing, and Verification IV. doi:10.1117/12.862693
[Hay-11]	J. Hayden, B. Eegholm, D. Kubalak, T. Hadjimichael, R Ohl, R Telfer, Mathematical Corrections Applied to Laser Radar Measurements Made Through a Cryogenic Vacuum Chamber Window, The Journal of the CMSC, Vol. 6, No. 2, Autumn 2
[Hee-20]	Henrik te Heesen, Michael Wahl, Mats Bremer, Adrian Huwer, Joachim Messemer (2020); Heterogene Einsatzfelder der generativen Fertigung; Industrie Management 4.0 Vol. 36 Part 4 (2020), http://dx.doi.org/10.30844/I40M_20-4_S25-25
[Hel-21]	R.H. Helle and H.G. Lemu, A case study on use of 3D scanning for reverse engineering and quality control, Materials Today: Proceedings, https://doi.org/10.1016/j.matpr.2021.01.828

[Hay-15]	J. Hayden et al., 2015, Patent No.: US 9,109,898 B2, Laser Radar through the window (LRTW) coordinate correction method, URL: https://ntrs.nasa.gov/api/citations/20150016932/downloads/20150016932.pdf
[Kef-15]	C.P. Keferstein, M. Marxer, Fertigungsmesstechnik, Praxisorientierte Grundlagen moderner Messverfahren, 2015, 8. Auflage, Springer Vieweg, DOI: 10.1007/978-3-8348-2583-4
[Kwa-19]	W. Kwangwoo, S. Vignesh, W. Kejin, L. Beiwen, Q. Hantang, Quantifying quality of 3D printed clay objects using a 3D structured light scanning system, Additive Manufacturing, Volume 32, 2020, 100987, ISSN 2214-8604, https://doi.org/10.1016/j.addma.2019.100987.
[Laz-19]	D. Lazarević, B. Nedić, S. Jović, Ž. Šarkoćević, M. Blagojević, Optical inspection of cutting parts by 3D scanning, Physica A: Statistical Mechanics and its Applications, Volume 531, 2019, 121583, ISSN 0378-4371, https://doi.org/10.1016/j.physa.2019.121583.
[Li-17]	F. Li, D. Stoddart & I. Zwierzak, I. (2017). A Performance Test for a Fringe Projection Scanner in Various Ambient Light Conditions. Procedia CIRP, 62, 400–404. doi:10.1016/j.procir.2016.06.0
[Men-16]	R. Mendricky, Determination of measurement accuracy of optical 3D scanners; 2016, MM Science Journal 06, p. 1565 – 1572, DOI: 10.17973/MMSJ.2016_12_2016183
[NAS-17]	National Aeronautics and Space Administration (NASA), CubeSat101, 2017
[NAS-19]	National Aeronautics and Space Administration (NASA), Mission Success Handbook für Cuebsat Missions, 2019
[NAS-21]	National Aeronautics and Space Administration (NASA), General Environmental Verification Standard (GEVS) for GSFC Flight Programs and Projects, 2021
[Pal-12]	M.J. Pallone, P.M. Meaney, K.D. Paulsen, 2012, Surface scanning through a cylindrical tank of coupling fluid for clinical microwave breast imaging exams. Medical Physics, 39(6Part1), 3102–3111. doi:10.1118/1.4711799
[Pal-15]	D. Palousek; M. Omasta, D. Koutny, J. Bednar, T. Koutecky; F. Dokoupil; Effect of matte coating on 3D optical measurement accuracy, 2015, Optical Materials 40 1-4, p. 1 – 9, DOI: 10.1016/j.optmat.2014.11.020

[Pap-14]	Papula L.; Mathematische Formelsammlung; 2014; 11. Auflage; Springer Vieweg; Wiesbaden
[Pfe-13]	Pfeiffer Vacuum GmbH; The Vacuum Technolgy Book Volume II; 2013; Pfeifer Vacuum GmbH; Asslar.
[QB5-15]	QB50 - System Requirements and Recommendations, 2015, Issue 7, https://www.qb50.eu/index.php/tech-docs/category/QB50_Systems_Requirements_issue_76e8e.pdf?download=89:qb50-docs
[Sch-99]	R. Schwarte, H. Heinol, B. Buxbaum, T. Ringbeck, Z. Xu, K. Hartmann, „Principles of Three-Dimensional Imaging Techniques", Handbook of Computer Vision and Applications, Volume 1, Sensors and Imaging, Academic Press, ISBN 978-0123797711 , London 1999.
[Sie-17]	Siebertz, Karl; van Bebber, David; Hochkirchen, Thomas (2017): Statistische Versuchsplanung. Berlin, Heidelberg: Springer Berlin Heidelberg
[Tip-19]	P.A. Tipler, G. Mosca, Physik; 2019; 8. Auflage; Springer Verlag; Heidelberg
[VDI-08a]	Richtlinie, VDI 2634: Optische 3-D-Messsysteme, Blatt 1, Bildgebende Systeme mit punktförmiger Antastung. Düsseldorf: VDI 2008
[VDI-08b]	Richtlinie, VDI 2634: Optische 3-D-Messsysteme, Blatt 2, Bildgebende Systeme mit flächenhafter Antastung. Düsseldorf: VDI 2008
[VDI-08c]	VDI 2634: Optische 3-D-Messsysteme, Blatt 3, Bildgebende Systeme mit flächenhafter Antastung in mehreren Einzelansichten. Düsseldorf: VDI 2008
[Wio-08]	G. Wiora, Optische 3D-Messtechnik: Präzise Gestaltvermessung mit einem erweiterten Streifenprojektionsverfahren, 2001, Dissertation an der Universität Heidelberg, http://archiv.ub.uni-heidelberg.de/volltextserver/1808/3/03_Diss_Wiora_Online_Version.pdf , abgerufen am 18.09.2021
[Wut-06]	M. Wutz, K. Jousten (Hrsg).; Wutz Handbuch Vakuumtechnik; 2006; 9. Auflage; Vieweg+Teubner Verlag; Wiesbaden.
[Yam-04]	Yamashita, A., Higuchi, H., Kaneko, T., & Kawata, Y. (2004). Three dimensional measurement of object's surface in water using the light stripe projection method. IEEE International Conference on Robotics

	and Automation, 2004. Proceedings. ICRA '04. 2004. doi:10.1109/robot.2004.1307474

Internet

[Cap-21]	https://www.capital.de/wirtschaft-politik/satelliten-kritik-an-elon-musk-wird-starlink-zu-einer-gefahr, abgerufen am 13.09.2021
[Dor-21]	https://www.dorotek.de/wp-content/uploads/2021/01/Optik-Katalog-Kapitel-01-Optische-Materialien.pdf abgerufen am 25.01.2022
[ESA-21a]	https://www.esa.int/Enabling_Support/Space_Engineering_Technology/Technology_CubeSats , abgerufen am 13.09.2021
[ESA-21b]	https://www.esa.int/Enabling_Support/Space_Engineering_Technology/Shaping_the_Future/Technology_Readiness_Levels_TRL
[ESA-17]	https://www.esa.int/Applications/Navigation/How_each_Galileo_satellite_is_tested_ahead_of_launch, abgerufen am 13.09.2021
[Gom-21]	https://www.gom.com/de-de/produkte/hochpraezise-3d-messtechnik/atos-5
[Kon-11	http://theorie.physik.uni-konstanz.de/lsfuchs/lectures/Skript_IK3_WS10-11/ik3ws1011_skript_aktuell.pdf ,abgerufen am 06.11.2021
[Pre-17]	https://docplayer.org/60191198-Endmasse-produktinformation.html , abgerufen am 21.11.2021
[Spa-21]	https://www.spacex.com/updates/starlink-mission-05-15-2021/index.html
[Sta-21]	https://www.starlink.com/, abgerufen am 13.09.2021
[Rau-20]	https://www.raumfahrer.net/mission-zur-entfernung-von-weltraummuell-beauftragt/; abgerufen am 09.09.2021
[Tag-21]	https://www.tagesschau.de/wirtschaft/technologie/starlink-spacex-elon-musk-satelliten-internet-101.html, abgerufen am 13.09.2021
[Zei-21]	https://www.handsonmetrology.com/products/t-scan-10-20#Technical_Data